Transport-Limited Aggregation and Dense Granular Flow

by

Jaehyuk Choi

B.S., Korea Advanced Institute of Science and Technology, 2000

Submitted to the Department of Mathematics
in partial fulfillment of the requirements for the degree of

Doctor of Philosophy

at the

MASSACHUSETTS INSTITUTE OF TECHNOLOGY

June 2005

© Jaehyuk Choi, MMV. All rights reserved.

Author . . . .
Department of Mathematics
April 13, 2005

Certified by . . . .
Martin Z. Bazant
Associate Professor of Applied Mathematics
Thesis Supervisor

Accepted by . . . .
Rodolfo R. Rosales
Chairperson, Applied Mathematics Committee

Accepted by . . . .
Pavel I. Etingof
Chairperson, Department Committee on Graduate Students

Transport-Limited Aggregation and Dense Granular Flow

by

Jaehyuk Choi

Submitted to the Department of Mathematics
on April 13, 2005, in partial fulfillment of the
requirements for the degree of
Doctor of Philosophy

Abstract

In this thesis, transport of interacting particles is studied in two different physical systems. In the first part, a model for interfacial growth driven by general transport processes is proposed to generalize Laplacian growth such as diffusion-limited aggregation (DLA) and viscous fingering. The fractal properties, crossover in morphology, and relation between continuous and stochastic growth are studied in the context of a representative case, advection-diffusion-limited aggregation (ADLA). The model is extended on curved surfaces and the effect of curvature is also discussed. In the second part, dense granular flow inside silos and hoppers is investigated using high-speed imaging and the results are compared to existing theories. While mean velocity fields are in qualitative agreement, the diffusion and mixing of particles are contradictory to the microscopic assumptions. A new model for dense granular flow is suggested to resolve the inconsistency.

Thesis Supervisor: Martin Z. Bazant
Title: Associate Professor of Applied Mathematics

Acknowledgments

Previously Published Works

Parts of this thesis have appeared (or will soon appear) in the following published articles:

Chaps. 2 and Chap. 3

M. Z. Bazant, J. Choi, and B. Davidovitch. Dynamics of conformal maps for a class of non-Laplacian growth phenomena. *Phys. Rev. Lett.*, 91:045503, 2003, cond-mat/0303234.

M. Z. Bazant, J. Choi, B. Davidovitch, and D. Crowdy. Transport-limited aggregation, *Chaos*, 14:S6, 2004.

M. Z. Bazant, J. Choi, and B. Davidovitch, Advection-diffusion-limited aggregation, *Chaos*, 14:S7, 2004.

Chap. 5

J. Choi, D. Margetis, T. M. Squires, and M. Z. Bazant. Steady advection-diffusion around finite absorbers in two-dimensional potential flows. to appear in *J. Fluid Mech.*, 2005, cond-mat/0403740.

Chap. 9

J. Choi, A. Kudrolli, and M. Z. Bazant. Velocity profile of granular flows inside silos and hoppers. *J. Phys.: Condens. Matter* 17:1, 2005, cond-mat/0501568.

Chap. 10

J. Choi, A. Kudrolli, R. R. Rosales, and M. Z. Bazant. Diffusion and mixing in gravity-driven dense granular flows. *Phys. Rev. Lett.* 92:174301, 2004, cond-mat/0311401.

Resources on the Internet

Further publications, computation codes, and other research updates can be found on the following internet sites:

Jaehyuk Choi's Homepage

> `http://www.jaehyukchoi.net`

Martin Z. Bazant's Homepage

> `http://www-math.mit.edu/~bazant`

MIT Dry Fluids Laboratory

> `http://www-math.mit.edu/dryfluids`

MIT Applied Mathematics Computational Laboratory

> `http://www-math.mit.edu/~bazant/AMCL`

Computation Codes for the Advection-Diffusion Problem (Chap. 5)

> `http://www.advection-diffusion.net`

Contents

List of Figures

List of Tables

Part I

Transport-Limited Aggregation

Chapter 1

Introduction to Part I

1.1 Diffusion-Limited Aggregation

Patterns abound in nature. From the double helix structure of DNA molecules to the spiral galaxies of celestial bodies, patterns prevail at all length-scales. To understand nature is, in no small part, to identify and explain patterns. Therefore, the important questions in studying patterns are the following: "what is the underlying rules responsible for a pattern?" and " how are the rules related to the manifested pattern?" In simple systems, the answers are sought in a deductive way, directly from the exact physics of the phenomena. In highly complex systems, however, reverse-engineering is often used; a model, consisting of simplified but relevant rules, is proposed and is verified by comparing the patterns from the model and ones in nature. Sometimes a model proposed on this purpose draws attention on its own light due to the richness of patterns it creates. One of the most successful example in this regard is diffusion-limited-aggregation (DLA) [7].

DLA was originally proposed by Witten and Sander [8] in 1981 to model the aggregates of metal particles formed by adhesive contact in low concentration limit. The model is set by the following simple rules: A seed is fixed at the origin of some coordinate system and one particle is released from a far-away boundary and allowed to take random walks. If the particle touches the seed, it irreversibly sticks to the seed and forms a two-particle aggregate. As soon as the random walker is removed either by being captured or escaping the boundary, the next walker is released and the process is repeated. Now it can stick to any particle in the aggregate as well as the original seed.

The resulting clusters are highly branched since DLA enhances the instability of growth.

The arriving particles are far more likely to stick to the tips of outer branches than to maneuver their way deep into the *fjords* before contacting the surrounding branches. Thus the tall branches of the cluster screen the small ones and grow faster. The growth on the tips, however, is not always in the outward radial direction. Sometimes a few new branches are spun off from one tip site as occurred at the original seed. The *tip-splitting* makes the DLA a clusters self-similar fractal.

1.2   Laplacian Growth

The significance of DLA is beyond that of a simply implementable toy model. DLA is known to have about 50 realizations in physical systems [9]. The ubiquity of DLA is related to diffusive transport, which is dominant in many pattern formations. To illustrate the popularity of DLA, we introduce a seemingly unrelated problem: *viscous fingering* [10]. Suppose that oil fills in a thin gap between two parallel glass plates, i.e., Hele-Shaw cell. If air is slowly injected through a hole on a plate, the interface becomes unstable and generates erratic structures of growing fingers similar to the branches in DLA. It turns out that the two different problems share the same theoretical background. In a Hele-Shaw cell, or more generally in a porous medium, the velocity of a viscous fluid (oil), $\boldsymbol{v}$, is proportional to the gradient of the pressure P via Darcy's law, $\boldsymbol{v} = -(k/\mu)\boldsymbol{\nabla}P$, where k is the permeability and μ is the viscosity of the fluid. If the fluid is incompressible, that is $\boldsymbol{\nabla} \cdot \boldsymbol{v} = 0$, the pressure P satisfies the Laplace equation. On the other hand, the injected fluid (air) can be assumed to have a constant pressure if the viscosity is much lower. Thus, in the limit of zero surface tension, the pressure of the viscous fluid and the velocity at the interface satisfy

$$\boldsymbol{\nabla}^2 P = 0 \quad \text{in} \quad \Omega \qquad \text{and} \qquad P = const., \quad \boldsymbol{v} \propto -\boldsymbol{\nabla}P \quad \text{at} \quad \partial\Omega, \qquad (1.1)$$

where Ω is the region of the viscous fluid. One should note that, since the injection is very slow, the time-derivative term in the diffusion equation becomes negligible; thus, the system is quasi-static.

Remarkably the same equation and boundary condition hold for DLA when P is re-placed by the concentration (or probability) of random walkers c and the velocity $\boldsymbol{v}$ by the probability measure for the next growth p. The one-by-one release of particles now plays the role of the slow injection of fluid. Thus DLA can be applied, directly or in a modified

18

way, to general pattern formation which is described by the Laplace equation. Such systems include the dielectric breakdown model (DBM) [11], electrodeposition [12], and dendritic crystal growth [13]. Recently, DLA has been claimed to have some relevance to biological systems [9].

Though they are governed by the same equation, viscous fingering and DLA are certainly different in that the former is, in theory, continuous and deterministic while the latter is stochastic. The growth occurs in parallel over the interface in continuous growth, but it occurs serially one site at a time in stochastic growth. More subtle differences are found in the growth instability. Shraiman and Bensimon [14] investigated the viscous fingering of zero surface tension and showed that the problem is mathematically ill-posed. An arbitrary shaped initial *seed* leads to a cusp-like singularity within a finite time; see Fig. 1-1. DLA does not exhibit the singularity since the particle size is finite. To avoid this unphysical outcome, one should add regularization, such as surface tension, in growth.

The relation between continuous and stochastic Laplacian growth is still controversial. There have been conjectures that they belong to the same universality class and supporting evidences from experiments and simulations [9, 15, 16, 17]. Recent studies, however, counter-claimed the universality although for different reasons. Ball and Somfai [18, 19] showed that the two growth models differ in the mechanism of the ultra-violet cutoff, and Barra et al. [20, 21] argued that the discrepancy comes from the growth rule (i.e., parallel vs. serial). For DLA grown in a channel geometry (with reflecting walls), Somfai et al. [22] claimed that, contrary to previous works [16], the average shape of DLA does not exactly match to any Saffman-Taylor finger solutions, which are zero surface tension profiles in the geometry.

1.3   The Hastings-Levitov Algorithm

The Laplacian equation is deeply involved in an implementation method of DLA as well. In two dimensions (2D), where DLA and viscous fingering is mostly studied, it is well known that conformal map is a convenient tool for solving the Laplace equation with complicated geometry since any solution is invariant under the mapping. In fact, the interface dynamics of viscous fingering was formulated as an equation for a time-dependent conformal map by Polubarinova-Kochina [23], Galin [24] in 1945. And it was in 1998 that Hastings and Levitov
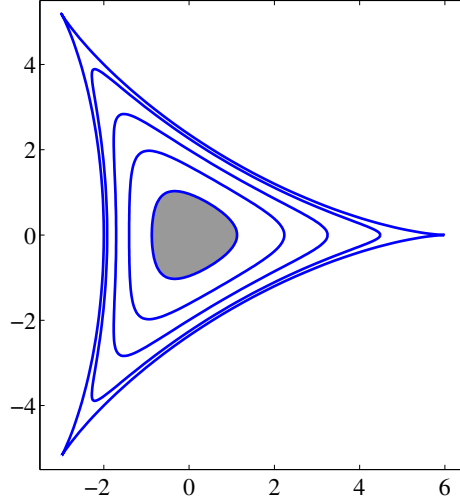
Figure 1-1: The continuous Laplacian growth of a triangularly perturbed disk (gray), $g(w) = w + 1/8w^2$ which lead to a cusp singularities in finite time $t_s = 3.5156$. The solid lines are the profiles at at $t = 1, 2, 3$ and t_s.

(HL) [25] cleverly used the conformal-mapping representation to describe the complicated boundary of DLA. Their formulation enabled the use of the analytical tools that come with conformal maps and helped the theoretical studies of DLA thereafter.

Suppose that we have a off-lattice DLA cluster. In order to determine the site for the next growth *a priori* without random walk simulations, one has to first solve Laplace equation for c and choose a boundary point according to the growth probability p as prescribed in Eq. (1.1). Not only is solving the Laplace equation not an easy task, but also one has to repeat it every time the cluster adds a new particle since the boundary has changed! This cumbersome procedure can be avoided only if we can find a conformal map from (the exterior of) a unit disk to (the exterior of) the cluster. If $z = g(w)$ is such a map, the equation is first solved in w-plane as $c(w) = \log|w|$ and then mapped back to the original z-plane as $c(z) = \log|g^{-1}(z)|$. Selecting the next growth point is more simple; the probability that a particle hits between two points, w_1 and w_2, on the unit circle in w-plane is equal to that between $g(w_1)$ and $g(w_2)$ in z-plane. Since our *cluster* in w-plane is radially symmetric, it practically means that one can randomly pick any point w ($|w| = 1$) with no angle preference and add a new particle at the site $g(w)$ of the cluster.

The trick of the HL algorithm is devising an elementary function which emulates adding a *bump* to a unit disk and bookkeeping the map $g(w)$ by iteratively applying those functions. If $g_{n-1}(w)$ is the map for a $(n - 1)$-particle cluster and ϕ_n is the elementary map for the

n-th particle, the map for the n-particle cluster is given by $g_{n-1} \circ \phi_n(w)$ and is further decomposed into

$$g_n(w) = \phi_1 \circ \phi_2 \circ \ \cdots \ \circ \phi_n(w). \tag{1.2}$$

Here each $\phi_k(w)$ has two parameters for the angle and the size of the bump. While the angle is completely random as mentioned, the size is inversely proportional to the Jacobian of the map so far, i.e., $\phi_{k-1}(w)$, so that the the bumps in z-plane have the same size. Fig. 1-2 shows early and later growth stages of a DLA cluster generated in the HL algorithm. Since the order of the function composition is reversed from that of the arrival of particles, the computation time of the algorithm scales as $O(n^2)$ where as direct random walk scales as $O(n)$ with some shortcut methods. Nevertheless conformal-mapping formulation is more appealing as the map itself gives detailed information about a cluster. For example, in the Laurent series expansion of $g_n(w)$,

$$g_n(w) = A_1 w + A_0 + \frac{A_{-1}}{w} + \frac{A_{-2}}{w^2} \cdots , \tag{1.3}$$

A_1 is called the *conformal radius* and A_0 the *center of charge* of the cluster. In the electrostatic analogy, they give the radius and the center of a charged disk, respectively, which would yield the same asymptotic electric potential far away as the cluster. A_1 is largely used for a measure of the characteristic size. Similarly, higher coefficients encode higher multipole moments.

For larger scale simulations, a hybrid method was developed by Somfai et al. [26], in which the cluster is generated by random walk, and then the conformal map is reconstructed from the sampled growth probability at the fixed cluster. The HL algorithm has been also modified to other stochastic interfacial dynamics such as snowflake, dielectric breakdown, and brittle fracture [27].

1.4 DLA as a Fractal

DLA is a simple model which provides rich aspects of fractals. In fact, DLA can be quantified mostly by its fractal properties, which distinguish it from other fractal objects. The fractal
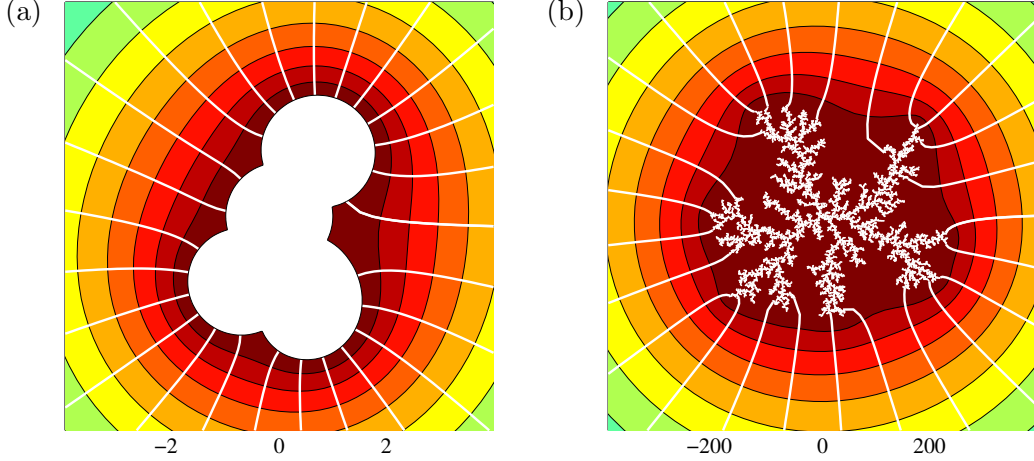
Figure 1-2: Simulation of DLA of (a) 4 and (b) 10^4 particles using the Hastings-Levitov algorithm ($a = 1/2$). Contour plots show the quasi-steady concentration (or probability) field for random walkers released from infinity, and solid curves indicate lines of diffusive flux.

dimension D_f is obtained from the power law,

$$R \sim n^{1/D_f}, \tag{1.4}$$

where n is the number of particles in a cluster and R is a characteristic size such as the radius of gyration or the conformal radius A_1. For 2D off-lattice DLA, $D_f = 1.71$ is reported [28].

The dimension, however, sensitively depends on geometrical factors. On a 2D square lattice, Meakin et al. [29] observed D_f decrease to 1.5 as the cluster size increased. Stepanov and Levitov [30] also showed that D_f can be as low as 1.5 for simulations of anisotropic growth using the noise-controlled HL algorithm. In a channel geometry, D_f also depends on the boundary condition; $D_f = 1.67$ [31] and $D_f = 1.71$ [22] are reported for periodic and reflecting boundary conditions respectively. The delicacy of DLA fractality is observed from other cases: Davidovitch et al. [32] used a quasi-random sequence $\theta_n = 2\pi W n$ with an irrational number W rather than random angles in the HL algorithm. This interesting choice also led to highly branched clusters, but their fractal dimension was higher than 1.71. In dielectric breakdown model, Hastings [33] observed a critical transition from fractal to non-fractal clusters when a parameter is increased.

It is, in fact, still controversial if DLA is truly fractal, i.e., the size of growing clusters is the only length scale. DLA exhibits complex scaling features and there have been reports about anomalous scalings; Plischke and Rácz [34] claimed that the average and the width of

22

the *active zone*, i.e., outer crust collecting new particles, scales differently, and thus, there are two diverging length scales. Amitrano et al. [35] and Stanley [9] claimed DLA obeys *multiscaling* where the fractal dimension D_f is a decreasing function of radius. Mandelbrot et al. [36] claimed both $D_f = 1.67$ and $D_f = 1.71$ coexist in the radial DLA clusters. Against these arguments, [26, 37, 38] recently reported that the anomalous scalings are finite size transients from the results of large scale simulations with the hybrid method.

DLA also shows *multifractality* [39, 40]. In an n-particle cluster, the i-th particle has a probability p_i to trap the next arriving particle. The probability set $\{p_i\}$, called the *harmonic measure*, shows a very wide distribution due to tips and fjords. From the moments of this distribution, it is possible to define infinitely many generalized fractal dimensions D_q:

$$\sum_{i=1}^{n} p_i^q \ \sim \ R^{-\tau(q)}, \quad D_q = \frac{\tau(q)}{q-1}. \tag{1.5}$$

The fractal dimension D_f equal to D_0 as Eq. (1.5) is reduced to Eq. (1.4) for $q = 0$. The next two dimensions, D_1 and D_2, are quantities previously known as the *information dimension* and the *correlation exponent* respectively. Generally D_q is a decreasing function of q [39], but D_q is a constant for homogeneous fractals. For DLA, the following are known about D_q: Makarov [41] mathematically proved that $D_1 = D_f$ for any harmonic measure of a simply connected region distorted under conformal maps. Halsey [42], using the *electrostatic* scaling relation, showed $D_3 = D_f/2$. Later Davidovitch et al. [43] derived the same result in the context of the HL algorithm, and the relation agrees with numerical results. Turkevich and Scher [44] and Halsey [42] obtained several relations between multifractal dimensions D_q. D_q for negative q depends on small values of p corresponding to rare events. From numerical studies [45, 46], it is known that D_q is infinite for $q < -0.2$.

There have been numerous theoretical approaches to solve D_f and D_q *a priori*, but they have been only partially successful. Unlike other random systems such as the self-avoiding random walk or percolation, DLA does not have an upper critical dimension above which the mean-field theory holds [47]. For DLA in d-dimensional Euclidean space, a mean-field continuum approximation [48] expects $D_f = d - 1$, but it is only valid in the limit of $d \to \infty$. The structure of DLA seems to be influenced by fluctuations which are not diluted by high dimensionality [7]. The scale-invariance of DLA naturally leads to renormalization group approaches. Among them are *fixed scale transformation* by Erzan et al. [49] and a

perturbative renormalization group analysis of the conformal dynamics by Hastings [50]. They give good results for fractal and multifractal dimensions. Yet another approach is *branched growth theory* [7, 51, 52, 53]; In this theory, the death of branches (by screening) competes with the creation of them (by tip-splitting) and thus a whole cluster is understood as a dynamical system of interacting branches.

1.5   Scope and Outline of Part I

We saw that a system of diffusive transport results in a surprisingly complex pattern. Alongside the effort to fully understand DLA, its huge success also brings us the questions; "what are the generalization of DLA to other transport processes?" and "how are they related to DLA?" The investigation of the first question is a natural step for modeling aggregation phenomena in which non-diffusive transports play important roles. Exploring the effect of transport rules on the morphological features of resulting patterns may be essential in estimating the physical setting under which a given pattern was generated. The second question can help understand DLA in a broader context. One can see how certain the properties of DLA are robust or fragile under *perturbations* on the underlying rules and where DLA is positioned among its peers.

In this thesis, we attempt to build transport-limited aggregation (TLA) model that generalizes DLA by relaxing the key assumptions of it. We begin in Chap. 2 by formulating the time-dependent conformal mapping dynamics for both continuous and stochastic growth limited by generalized transport processes. In Chap. 3, advection-diffusion-limited aggregation (ADLA) is studied in depth as a representative example. We investigate the crossover and convergence of ADLA and compare the average shape with the continuous growth profile. Asymptotic analysis and numerical methods for the advection-diffusion problem, which is essential for ADLA simulation, are discussed in Chap. 5. In Chap. 4, we extend the formulation of TLA to the surface of constant Gaussian curvature such as a sphere and a pseudosphere and discuss the effect of the curvature. Finally, in Chap. 6, we conclude with remarks on the success and limitation of our result.

Chapter 2

Transport-Limited Aggregation

Laplacian growth models describe some of the best known phenomena of pattern forma-
tion far from equilibrium, including continuous dynamics such as viscous fingering [54]
and (quasi-static) dendritic solidification [13] and stochastic processes such as diffusion-
limited aggregation (DLA) [8] and dielectric breakdown [11]. In this class of models, the
interfacial velocity is determined by the normal derivative of a harmonic function, so the
powerful technique of conformal mapping has been used extensively in two dimensions.
Time-dependent conformal maps are used in the classical analysis of continuous Laplacian
growth [14, 23, 24, 55], and the analogous method of iterated conformal maps has recently
been developed for stochastic Laplacian growth [25, 33, 43].

In spite of the broad relevance of these models, real growth phenomena often involve
non-Laplacian transport processes, such as advection or electro-migration coupled to dif-
fusion [56, 57, 58, 59]. Much less theoretical work exists in such cases, in part because
conformal mapping would appear to be of little use for non-harmonic functions. An ex-
ception is the recent use of streamline coordinates for dendritic solidification in a potential
flow, but it turns out that advection has no effect on the shape of an infinite dendrite [60].
Stochastic conformal-map dynamics, however, has not yet been formulated for any non-
Laplacian transport process (although iterated conformal maps have been used in a recent
model of brittle fracture with a bi-harmonic elastic potential [61].

In this Chapter, the dynamics of conformal maps for Laplacian growth is generalized. In
Sec. 2.1, we consider non-Laplacian transport processes in a recently identified conformally
invariant class [62]. Then we formulate continuous and stochastic growth from a finite seed

in Secs. 2.2 and 2.3 respectively.

2.1 Transport Processes and Boundary Conditions

Consider a set of scalar "fields," $\boldsymbol{\varphi} = \{\varphi_1, \varphi_2, \ldots, \varphi_M\}$, whose gradients produce quasi-static, conserved "flux densities,"

$$\boldsymbol{F}_i = \sum_{j=1}^{M} C_{ij} \boldsymbol{\nabla}\varphi_j , \quad \boldsymbol{\nabla} \cdot \boldsymbol{F}_i = 0 \quad (1 \le i \le N) \tag{2.1}$$

where the coefficients, $\{C_{ij}(\boldsymbol{\varphi})\}$, may be nonlinear functions of the fields. This general system contains a number of physical cases [62]: ($M = 1$) simple nonlinear diffusion, $\boldsymbol{F}_1 = -D(c)\boldsymbol{\nabla}c$, where c is a temperature or particle concentration and $D(c)$ the diffusivity; ($M = 2$) advection-diffusion, $\boldsymbol{F}_1 = c\boldsymbol{\nabla}\varphi - D(c)\boldsymbol{\nabla}c$, of a scalar c in a potential flow, $\boldsymbol{u} = \boldsymbol{F}_2 = \boldsymbol{\nabla}\varphi$, (e.g. in a porous medium or Hele-Shaw cell); and ($M \ge 2$) various cases of electrochemical transport, $\boldsymbol{F}_i = -D_i(c_i)\boldsymbol{\nabla}c_i - b_i(c_i)q_i c_i \boldsymbol{\nabla}\varphi$, where c_i, D_i, b_i, and q_i are respectively the concentration, diffusivity, mobility, and charge of ion i, and φ is the (non-harmonic) electrostatic potential determined by the electro-neutrality condition, $\sum_{i=1}^{M} q_i c_i = 0$.

In planar geometries, it is convenient to represent a vector, $\boldsymbol{F} = (F_x, F_y)$, as a complex scalar, $F = F_x + iF_y$, so Eq. (2.1) takes the form,

$$F_i = \sum_{j=1}^{M} C_{ij} \nabla \varphi_j , \quad \mathrm{Re}\,\{\overline{\nabla} \boldsymbol{F}_i\} = 0 \tag{2.2}$$

in the $z = x + iy$ plane, where $\nabla = \frac{\partial}{\partial x} + i\frac{\partial}{\partial y}$. Under a conformal mapping, $w = f(z)$, F_i transforms as

$$F_i(z, \bar{z}) = \overline{f'(z)}\, F_i(w, \overline{w}). \tag{2.3}$$

(like ∇ [63]), and $\mathrm{Re}\,\{\overline{\nabla}F_i\} = 0$ is unchanged. Therefore, even though the solutions (depending on z and $\bar{z} = x - iy$) are not harmonic functions, the usual trick of conformal mapping still works [62]: If $\boldsymbol{\varphi}(w, \bar{w})$ solves Eq. (2.2) in one domain, Ω_w, then $\boldsymbol{\varphi}(f(z), \overline{f(z)})$ solves Eq. (2.2) in another domain, $\Omega_z = f^{-1}(\Omega_w)$ (with appropriately transformed boundary conditions).

Interfacial dynamics in the plane can be elegantly described by a conformal map,

$z = g(w, t)$, from Ω_w, the exterior of the unit circle, to $\Omega_z(t)$, the exterior of the (singly connected) growing object [14, 23, 24, 25, 33, 43, 55]. Since the map must be univalent (one-to-one), it has a Laurent series,

$$g(w, t) = A_1(t)w + A_0(t) + \frac{A_{-1}(t)}{w} + \frac{A_{-2}(t)}{w^2} + \cdots , \qquad (2.4)$$

for $|w| > 1$, where $A_1(t)$ is real and defines an effective diameter of $\Omega_z(t)$ [25]. As described above, the fields satisfying Eq. (2.1) in $\Omega_z(t)$ are easily obtained from the inverse, $w = f(z, t)$, once the same equations are solved in Ω_w. As in Laplacian growth, the removal of geometrical complexity from the transport problem is a tremendous simplification.

On the moving boundary, $\partial\Omega_z(t)$, we consider generalized Dirichlet ($B(\boldsymbol{\varphi}_i) = 0$) and Neumann ($\hat{\boldsymbol{n}} \cdot \boldsymbol{\nabla}\varphi_i = 0$) boundary conditions (BC) [62]:

$$B\left(\boldsymbol{\varphi}(z, \bar{z})\right) = 0 \quad \text{or} \quad \hat{\boldsymbol{n}} \cdot \boldsymbol{F}_i = \text{Re}\left\{\overline{n(z)}F_i(z, \bar{z})\right\} = 0 \qquad \text{for} \qquad z \in \partial\Omega_z(t), \qquad (2.5)$$

where $n = n_x + in_y$ represents the outward normal, $\hat{\boldsymbol{n}}$, and $B(\boldsymbol{\varphi})$ is a function of the fields. The former BC express interfacial equilibrium for "fast reactions" (compared to transport rates), while the latter expresses impermeability to flows ($\boldsymbol{F} = \boldsymbol{u} = \boldsymbol{\nabla}\varphi$) or flux densities of non-reacting species. Due to Eq. (2.3), these BC are the same for $w \in \partial\Omega_w$,

$$B\left(\boldsymbol{\varphi}(w, \overline{w})\right) = 0 \quad \text{or} \quad \hat{\boldsymbol{n}} \cdot \boldsymbol{F}_i = \text{Re}\left\{\overline{w}F_i(w, \overline{w})\right\} = 0 \qquad \text{for} \qquad |w| = 1, \qquad (2.6)$$

since $n(w) = w = n(z)f'(z)/|f'(z)|$.

Far from the growth, we assume either constant values of the fields (e.g. temperature, concentration) or given flux (or flow) profiles which drive the growth:

$$\varphi_i(z, \bar{z}, t) \to \varphi_i^{\infty}(t) \quad \text{or} \quad F_i(z, \bar{z}, t) \sim F_i^{\infty}(t) \qquad \text{as} \qquad |z| \to \infty. \qquad (2.7)$$

The former BC also remain the same after conformal mapping, but the latter is transformed by Eqs. (2.3) and (2.4):

$$\varphi_i(w, \bar{w}, t) \to \varphi_i^{\infty}(t) \quad \text{or} \quad F_i(w, \bar{w}, t) \sim \overline{A_1(t)}\, F_i^{\infty}(t) \qquad \text{as} \qquad |w| \to \infty. \qquad (2.8)$$

Through $A_1(t)\, (= \overline{A_1(t)})$, the fields and fluxes in Ω_w vary with the diameter of the growth,

$\Omega_z(t)$.

2.2   Continuous Growth

Suppose that a Lagrangian boundary point, $z(t) \in \partial\Omega_z(t)$, moves in the normal direction with (complex) velocity,

$$v = z_t = \alpha\, n\, \sigma, \quad \sigma = \mathrm{Re}\,\{\overline{n}Q\}, \quad Q = \sum_{i=1}^{M} B_i F_i, \qquad (2.9)$$

where $\boldsymbol{Q}$ is a flux density causing growth, α is a constant, and $B_i(\boldsymbol{\varphi})$ may be functions of the fields. This generalizes Stefan's law ($\boldsymbol{v} = \alpha\, \hat{\boldsymbol{n}} \cdot \boldsymbol{\nabla}\varphi$), e.g. to electrodeposition [58, 59] (where $\boldsymbol{Q}$ is for the depositing ion).

The classical analysis of viscous fingering is easily generalized to Eqs. (2.2), (2.5), (2.7), and (2.9). Let $w(t)$ be a "marker" for $z(t) = g(w(t), t)$ on Ω_w [55]. Substituting $z_t = g'\, w_t + g_t$ into Eq. (2.9), multiplying by $\overline{w g'}$, taking the real part, and using $\mathrm{Re}\,\{\overline{w}w_t\} = 0$ for $|w|^2 = \overline{w}w = 1$, we arrive at an evolution equation for the conformal map,

$$\mathrm{Re}\,\{\overline{w\, g(w)'}\, g_t(w)\} = \alpha\, \sigma(w, t) \qquad \text{for} \qquad |w| = 1 \qquad (2.10)$$

where $\sigma(w, t) = \mathrm{Re}\,\{\overline{w}Q(w, \overline{w})\} = \hat{\boldsymbol{n}} \cdot \boldsymbol{\nabla}\boldsymbol{Q}$ is the normal flux density on Ω_w. The evolution equation for radial Laplacian growth (e.g. viscous fingering) [14, 23, 24], $\mathrm{Re}\,\{\overline{w\, g'}\, g_t\} = 1$, corresponds to the special case of uniform flux, $\sigma = \text{constant}$. This dynamics is known to preserve number of pole-like singularities (inside the unit circle) for a wide class of initial maps, $g(w, 0)$. Except for some elementary maps, e.g. circles and ellipses, which preserve their shapes, arbitrary smooth initial interfaces develop singularities (cusps) in finite time [14].

In our generalized models, the time-dependent, non-uniform flux, σ, in Eq. (2.10) changes the analytic structure of an initial map (including the number of poles), so even circles and ellipses become distorted. This raises interesting questions about finite-time singularities: For example, what is the fate of solidification from a circular seed in a flowing melt (with σ described below)? Does advection generally enhance or retard the formation of singularities? We leave these questions for future work and focus here on non-Laplacian fractal growth.
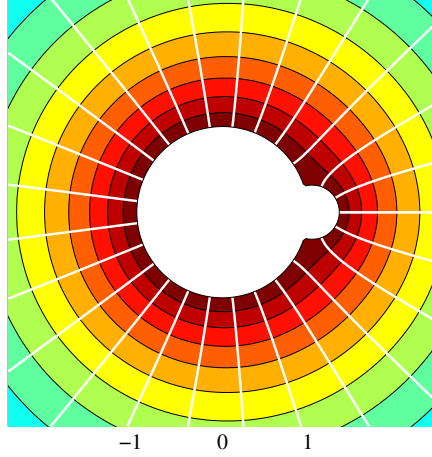
Figure 2-1: The image of "bump" function $\phi_{\lambda,\theta}(w)$ with bump area $\lambda = 0.1$, angle $\theta = 0$ and the elongation $a = 1/2$. The contour plot and solid curves indicate the concentration field and the lines of flux.

2.3   Stochastic Growth

Suppose that the domain, $\Omega_z(t_n)$, grows from its initial shape, $\Omega_z(0)$, at times $t_1, t_2, \cdots, t_n$ by discrete "bumps" representing n particles of characteristic area, λ_o [25, 43]. Since our models exhibit non-trivial time-dependence (see Sec. 3.1), we introduce time into the usual morphological model by replacing Eq. (2.9) with $p(z, t_n) = \alpha\, \sigma(z, t_{n-1})\,/\lambda_o$, for $z \in \partial\Omega_z(t_{n-1})$, where $p(z, t_n)\,|dz|\,dt$ is the probability that the nth growth event occurs in the boundary element $(z, z + dz)$ in the time interval $(t, t + dt)$. The waiting time, $t_n - t_{n-1}$, is then an exponential random variable with mean, τ_n, given by

$$\frac{\lambda_o}{\alpha \tau_n} = \oint_{\partial\Omega_z(t_{n-1})} \sigma(z, t_{n-1})\,|dz| = \int_0^{2\pi} d\theta\,\sigma(e^{i\theta}, t_{n-1}) \tag{2.11}$$

where we use $|dz| = |dw|/|f'|$ and $\sigma(z) = |f'(z)|\sigma(w)$ from Eq. (2.3) to transform to $\partial\Omega_w$ where $w = e^{i\theta}$ and $|dw| = d\theta$. The probability that the position of the nth growth occurs in $(z, z + dz) \subset \partial\Omega_z(t_{n-1})$ is, $p(z, t_n)|dz| = (\alpha/\lambda_o)\,\tau_n\,\sigma(z)|dz| = p(\theta, t_n)d\theta$, where

$$p(\theta, t_n) = \frac{\sigma(e^{i\theta}, t_{n-1})}{\int_0^{2\pi} d\theta'\,\sigma(e^{i\theta'}, t_{n-1})} = \frac{\alpha}{\lambda_o \tau_n}\,\sigma(e^{i\theta}, t_{n-1}) \tag{2.12}$$

is the probability measure for angles on the unit circle. In DLA [25], $p(z, t_n)$ is the harmonic measure, $p(\theta) = 1/2\pi$ is uniform, and τ_n is not defined.

It is now straightforward to generalize the Hastings-Levitov algorithm [25] to our non-

29

Laplacian models. As for DLA, the univalent map $z = g(w, t_n)$ from the exterior of the unit disk, Ω_w, to the exterior of an n-particle aggregate, $\Omega_z(t_n)$, is constructed iteratively by

$$g_n(w) = g_{n-1} \circ \phi_{\lambda_n, \theta_n}(w), \qquad g_n(w) = g(w, t_n), \tag{2.13}$$

where $\phi_{\lambda, \theta}(w)$ is a two-parameter basic map, conformal in Ω_w, that places a bump of area λ_n around an angle θ_n on the unit circle. Our choice of $\phi_{\lambda, \theta}(w)$ for simulations in the following Chapters is given by [25]

$$\phi_{\lambda,0} = w^{1-2a} \left\{ \frac{\sqrt{1+\lambda}}{2} \left(1 + w + w \sqrt{1 + \frac{1}{w^2} - \frac{1-\lambda}{1+\lambda} \frac{2}{w}} \right) \right\}^{2a}$$

$$\phi_{\lambda,\theta} = e^{i\theta} \, \phi_{\lambda,0}(e^{-i\theta} w). \tag{2.14}$$

The parameter, a, determines the aspect ratio of the bump and stay in the range of $0 < a \leq 1$: The higher a is, the more elongated the bump is in the normal direction. The bump becomes a semi-circle at $a = 1/2$ and a line segment ("strike") at $a = 1$. In order to fix the area λ_o of a new bump on $\partial \Omega_z(t_n)$, the size of its preimage, λ_n, on $\partial \Omega_w$ is divided by the Jacobian of the previous map,

$$\lambda_n = \frac{\lambda_o}{|g'_{n-1}(e^{i\theta_n})|^2}. \tag{2.15}$$

The difference between TLA and DLA is the sequence of the angles, $\{\theta_n\}$. While, in DLA, the angle is randomly chosen from the uniform distribution, $p(\theta) = 1/2\pi$, it is chosen according to the time-dependent (non-harmonic) measure, $p(\theta, t_n)$ in Eq. (2.12). Obtaining the non-trivial probability each time step certainly adds an extra complexity to the simulation. It seems, however, that our method is more efficient than the direct particle simulation method, in which one has to solve the field of drift every time the cluster adds a particle. In some desirable cases, such as ADLA in Chap. 3, $p(\theta, t_n)$ can be fully tabularized in advance, thus the complexity is the same as that of DLA simulation. Another difference, although it does not change the morphology of resulting aggregates, is the evolving waiting time, τ_n, in Eq. (2.11), which is not clear in DLA.

Chapter 3

Advection-Diffusion-Limited Aggregation

To illustrate the general theory developed in Chap. 2, we study growth driven by advection-diffusion in a potential flow and simulate advection-diffusion-limited aggregation (ADLA). In ADLA the released particles are being drifted in the direction of the background flow as well as random-walking. ADLA is one of the simplest examples of the broad class of TLA, but it raises nontrivial issues in regards of the interplay between the two transport processes.

The morphology of ADLA is among them. One easily expects that ADLA clusters grow toward the direction of higher particle flux, i.e, tend to climb up the incoming fluid. Therefore, it is an interesting question whether the cluster will be a non-fractal object like a stretched one-dimensional branch given that the fractality of DLA is very sensitive (see Chap. 1). If it remains fractal, one should look into the fractal dimension D_f.

The connection between continuous and stochastic growth can be investigated in the context of ADLA. For the most direct comparison, we ask "what is the asymptotic average cluster shape of stochastic growth?" and "how does it compare with the corresponding shape of continuous growth?" Note that DLA is a degenerate case where the asymptotic shapes for the two growth processes are simply circles due to the radial symmetry in growth. On the other hand, ADLA takes a non-trivial average shape as advection breaks the radial symmetry. Thus these questions about ADLA might give a useful insight back to the theories for DLA. In particular, such investigation may explain the limited success of the

mean-field theories which are based on continuous Laplacian growth.

We begin in Sec. 3.1 by formulating advection-diffusion-limited growth. In Sec. 3.2, the scaling and crossover of ADLA are looked into. In Sec. 3.3 and 3.4, we present the asymptotic shape of continuous and stochastic growth respectively and compare them. In Sec. 3.5, we show how the two shapes are related. The continuous dynamics is a self-consistent mean-field approximation of the stochastic dynamics, which, nevertheless, does not accurately predict the average shape of aggregates. In Sec. 3.6, we discuss the generality of the results.

3.1   Transport Processes and Boundary Conditions

We consider the stochastic aggregation of particles around a seed of characteristic size L_o, limited by advection-diffusion in a uniform potential flow of speed U_∞ and concentration C_∞. In $\Omega_z(t)$ the transport problem has the usual dimensionless form,

$$\text{Pe}_o \, \boldsymbol{\nabla}\varphi \cdot \boldsymbol{\nabla}c = \boldsymbol{\nabla}^2 c, \quad \boldsymbol{\nabla}^2\varphi = 0, \qquad z \in \Omega_z(t) \tag{3.1}$$

$$c = 0, \quad \hat{\boldsymbol{n}} \cdot \boldsymbol{\nabla}\varphi = 0, \qquad z \in \partial\Omega_z(t) \qquad \text{and} \qquad c \to 1, \qquad |z| \to \infty \tag{3.2}$$

$$\boldsymbol{\nabla}\varphi \to \hat{\boldsymbol{x}}, \qquad |z| \to \infty, \tag{3.3}$$

with the normal flux density for growth,

$$\sigma = \hat{\boldsymbol{n}} \cdot \boldsymbol{\nabla}c, \qquad z \in \partial\Omega_z(t), \tag{3.4}$$

where x, φ, c, and σ are in units of L_o, $U_\infty L_o$, C_∞, and DC_∞/L_o, respectively, and $\text{Pe}_o = U_\infty L_o/D$ is the *bare* Péclet number. In the notation in Chap. 2, we solve Eq. (2.2) in $\Omega_z(t)$ with BCs of type (2.5) and (2.7) for the "fluxes," $F_1 = Q = -\nabla c + \text{Pe}_o \, c\nabla\varphi$ and $F_2 = u = \nabla\varphi$.

In Ω_w Eqs. (3.1)~(3.2) remain the same. The BCs in Eq. (3.2) belong to the type of Eq. (2.6). However, the background flow speed at $|w| \to \infty$ in Eq. (3.3) diverges with $A_1(t)$ by Eq. (2.8). It is natural then to rescale the w-velocity by $A_1(t)$ to fix the background flow speed at unity as $\hat{\boldsymbol{x}}$, and instead solve the same equations in Ω_w with a *time-dependent* Péclet number,

$$\text{Pe}(t) = \text{Pe}_o \, A_1(t). \tag{3.5}$$

The velocity potential in Ω_w has the usual harmonic form, $\varphi(w) = \mathrm{Re}\,\{w + 1/w\}$, for the potential flow past the unit disk, and thus Eqs. (3.1)~(3.3) are mapped to Ω_w as

$$\mathrm{Pe}\,\boldsymbol{\nabla}\varphi \cdot \boldsymbol{\nabla}c = \boldsymbol{\nabla}^2 c, \quad \varphi = \mathrm{Re}\left\{w + \frac{1}{w}\right\}, \qquad |w| > 1 \tag{3.6}$$

$$c = 0, \qquad |w| = 1 \quad \text{and} \quad c \to 1, \qquad |w| \to \infty. \tag{3.7}$$

Since $A_1(t)$ is an effective diameter for $\Omega_z(t)$, the theory has shown us how to properly define Pe (which is not obvious for fractals). Note that, with this scaling, the time dependence of the solution is only via $\mathrm{Pe}(t)$, e.g., $c(w, \bar{w}, t) = c(w, \bar{w}; \mathrm{Pe}(t))$, $p(\theta, t) = p(\theta; \mathrm{Pe}(t))$, and $\tau_n = \tau_n(\mathrm{Pe}(t))$.

For a growth problem, Eqs. (3.6)~(3.7) need to be solved for a wide range of Pe due to the growth of $A_1(t)$. Numerical and analytical solution methods for the normal flux, σ, are extensively discussed in Chap. 5. An important result from asymptotic analysis is that the (non-harmonic) concentration $c(w, \overline{w}; \mathrm{Pe})$ can be derived as

$$c(w, \overline{w};\ \mathrm{Pe}) \sim \begin{cases} \log|w|\ /\ (\ \log(4/\mathrm{Pe}) - \gamma\ ) & \mathrm{Pe} \ll 1 \\ \mathrm{erf}\left[\sqrt{\mathrm{Pe}}\ \mathrm{Im}\left(\sqrt{w} + 1/\sqrt{w}\right)\right] & \mathrm{Pe} \gg 1, \end{cases} \tag{3.8}$$

where $\mathrm{erfc}(z)$ is the error function and γ is the Euler number. The low-Pe approximation, the familiar harmonic field of Laplacian growth, is valid out to a "boundary layer at ∞," while the high-Pe approximation is valid away from a wake region around the positive real axis (the branch cut for $\sqrt{w}$) [62]. From Eqs. (2.11), (2.12), and (3.8) we also obtain

$$\tau_n(\mathrm{Pe}) \sim \begin{cases} (\ \log(4/\mathrm{Pe}) - \gamma\ )/2\pi \\ (1/8)\sqrt{\pi/\mathrm{Pe}} \end{cases}, \quad p(\theta; \mathrm{Pe}) \sim \begin{cases} p_o(\theta) = 1/2\pi & \mathrm{Pe} \ll 1 \\ p_\infty(\theta) = \sin(\theta/2)/4 & \mathrm{Pe} \gg 1 \end{cases}, \tag{3.9}$$

where τ_n is measured in the unit of $(\lambda_o/D)/(\alpha C_\infty)$.

We see that advection eventually dominates diffusion and the growth probability becomes anisotropic as $\mathrm{Pe}(t) \to \infty$; thus, the stochastic dynamics undergoes a crossover from DLA to a new dynamics. Even for $\mathrm{Pe}_o \ll 1$, the ADLA dynamics smoothly crosses over from the diffusion-dominated "unstable fixed point," $\mathrm{Pe}(t) \ll 1$, to the new advection-dominated "stable fixed point," $\mathrm{Pe}(t) \gg 1$. The morphology of aggregates is also expected to converge to a fixed point independent of the shape of the seed. Although the morphology comes

from the accumulated influence of $p(\theta; \text{Pe})$ for $\text{Pe}_o < \text{Pe} < \infty$, the growth probability $p_\infty(\theta)$ eventually dominates transients and the initial condition is forgotten.

3.2 Scaling and Crossover of ADLA

We grow ADLA clusters by the modified Hastings-Levitov algorithm as described in Sec. 2.3. The growth probability $p(\theta; \text{Pe})$ is accurately obtained from the numerical methods in Chap. 5 for dense static values of Pe in advance and is interpolated for actual values of $\text{Pe}(t_n)$ in simulations. We perform ADLA simulations of $n = 10^4 \sim 10^5$ particles for various initial conditions such as the flow speed, Pe_o, the shape of seed, $g_0(w)$, the bump size, λ_0, and the elongation, a.

We show in Fig. 3-1 the evolution of the field in both Ω_z and Ω_w during a simulation of a 10^4 particle cluster. The growth is highly anisotropic and moves toward the flow for $\text{Pe} \gg 1$, but the branched structure of the aggregate resembles that of DLA. The resulting morphology of ADLA looks to be independent of the initial conditions. The two clusters in Fig. 3-2 grown from different seeds end up in similar shapes at $n = 10^5$.

We quantitatively investigate the scaling and crossover; the Laurent coefficients in Eq. (2.4) contain morphological information [25, 43]. From Eq. (2.13) we can obtain the recurrence relations for $\{A_k\}$ and thus for $\{\xi_k\}$. The first three relations are

$$A_1(t_n) = A_1(t_{n-1})a_1, \tag{3.10}$$

$$A_0(t_n) = A_1(t_{n-1})a_0 + A_0(t_{n-1}), \tag{3.11}$$

$$A_{-1}(t_n) = A_1(t_{n-1})a_{-1} + A_{-1}(t_{n-1})/a_1, \tag{3.12}$$

where a_k is the corresponding Laurent coefficients of $\phi_{\lambda,\theta}(w)$ in Eq. (2.14),

$$a_1 = (1+\lambda)^a, \quad a_0 = \frac{2a\lambda e^{i\theta}}{(1+\lambda)^{1-a}}, \quad \text{and} \quad a_{-1} = \frac{2a\lambda e^{2i\theta}}{(1+\lambda)^{2-a}}\left(1 + \frac{2a-1}{2}\lambda\right). \tag{3.13}$$

As illustrated in Fig. 3-3(a), the diameter of the cluster, $A_1(t_n) \sim n^{1/D_f}$, remarkably maintains the same fractal dimension as DLA, $D_f = 1.71$, for all Pe_o in the scaling regime, $A_1(t_n) \gg 1$. (As a check, we obtain the same D_f from the radius of gyration.) *A posteriori*, this can be understood by noting that the stable fixed point has a growth measure, $p_\infty(\theta) \propto \sin\theta/2$, which is differentiable, and thus locally constant (as in DLA), everywhere

34
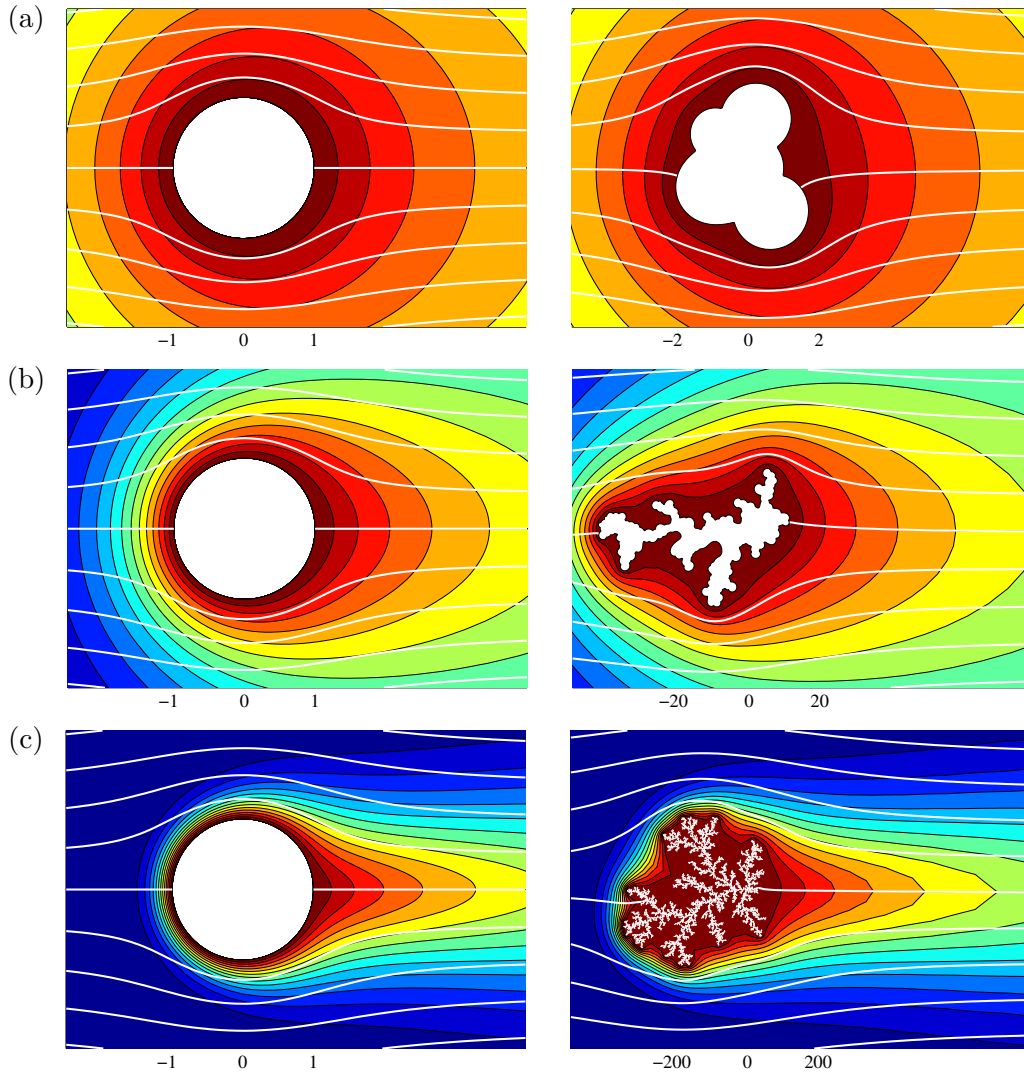
Figure 3-1: Evolution of the flow (white streamlines) and concentration (color contour plot) in Ω_w (left) and in $\Omega_z(t)$ (right) during advection-diffusion-limited aggregation of $n = 10^4$ particles with the flow speed $\mathrm{Pe}_o = 0.05$, the unit disk seed $g_0(w) = w$, and the semicircular bump $a = 1/2$. The rows from top to bottom correspond to (a) $\mathrm{Pe}(t_4) = 0.1$, (b) $\mathrm{Pe}(t_{182}) = 1$, and (c) $\mathrm{Pe}(t_{10^4}) = 10$. The plots in the right column are shown rescaled by $A_1(t_4) = 2$, $A_1(t_{182}) = 20$, and $A_1(t_{10^4}) = 200$, the effective diameters of the fractal cluster.
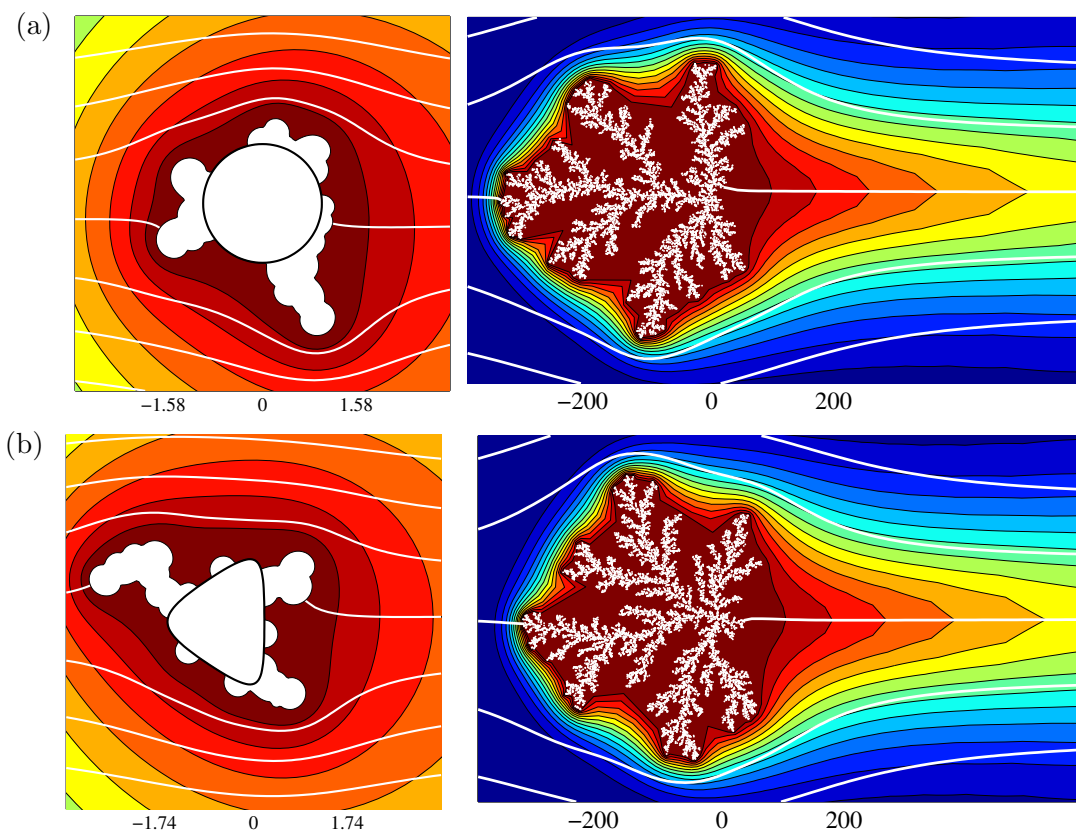
Figure 3-2: The growth of ADLA clusters with two different "seeds": (a) the unit disk, $g_0(w) = w$ and (b) the round triangle, $g_0(w) = w - 0.5 - 0.1/w - 0.2/w^2$. Initial Péclet number and particle size are set as $\text{Pe}_o = 10^{-2}$ and $\lambda_0 = 1/16$. Initial stages (left) shows $n = 20$ particles aggregated to the seed in near-symmetric DLA-limit concentrations profiles and the final states (right) shows $n = 10^5$ particles growing toward to $-\hat{\boldsymbol{x}}$ direction in highly asymmetric profiles.
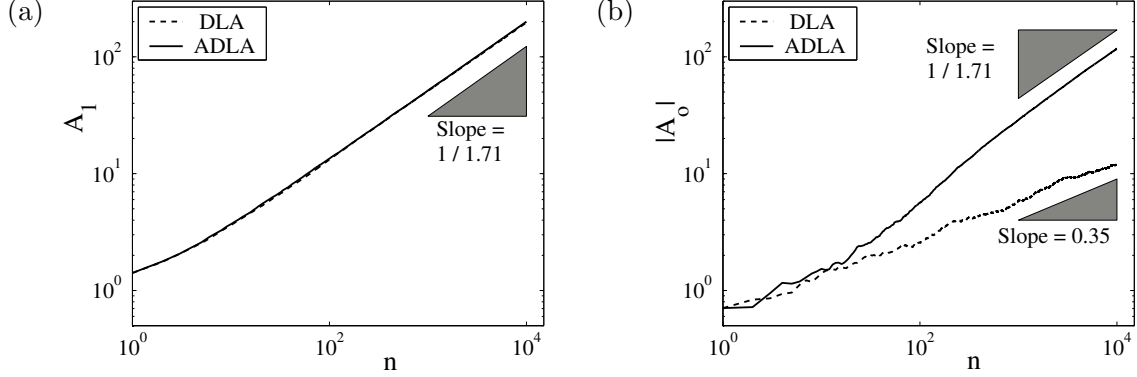
Figure 3-3: Log-log plot of the Laurent coefficients, (a) A_1 and (b) $|A_0|$ versus n, averaged over ADLA simulations (Pe$_o = 0.05$, $\lambda_o = L_o^2 = 1$), compared with analogous results for DLA without advection.

except at the rear stagnation point, $\theta = 0$. Physically, this simply means that diffusion always dominates advection at small scales. We conjecture that the same D_f holds for any non-Laplacian dynamics in our class, if $\lim_{n\to\infty} p(\theta, t_n)$ is continuous and almost everywhere differentiable. The surprising universality of $D_f = 1.71$ makes its exact value seem quite fundamental.

The expected total mass versus time, $n(t)$, also undergoes a crossover. Using Eqs. (2.11) and (3.9) and integrating

$$\frac{dn}{dt} = \frac{1}{\tau_n(\mathrm{Pe}_o A_1)} \approx \frac{1}{\tau_n(n^{1/D_f})} \qquad (3.14)$$

yields, $n(t) \propto t$ for $t \ll 1$ and $n(t) \propto t^{2D_f/(2D_f-1)}$ for $t \gg 1$, where again only D_f matters. The cluster diameter $A_1(t)$ switches from t^{1/D_f} to $t^{2/(2D_f-1)}$ scaling in time, even though the scaling with $N(t)$ does not change. One should also bear in mind that $\tau_n \to 0$ as Pe$(t) \to \infty$, so the quasi-static, discrete-growth approximation must eventually break down (although this is delayed in the dilute limit, $\alpha C \ll 1$).

The anisotropy of ADLA is seen from the scaling of the next Laurent coefficient, $A_0(t)$, the "center of charge," [43]

$$|A_0(t_n)| \sim \begin{cases} N^a & \mathrm{Pe} \ll 1 \\ N^{1/D_f} & \mathrm{Pe} \gg 1 \end{cases} \qquad (3.15)$$

which crosses over from DLA scaling ($2a = 0.7$ [43]) to the same scaling as $A_1(t_n)$, as shown in Fig. 3-3(b). Thus, $A_0(t_n)/A_1(t_n)$ converges to a constant as $n \to \infty$, and we further speculate that the same holds for the ratio of the higher coefficients, $A_{-k}(t_n)/A_1(t_n)$ for
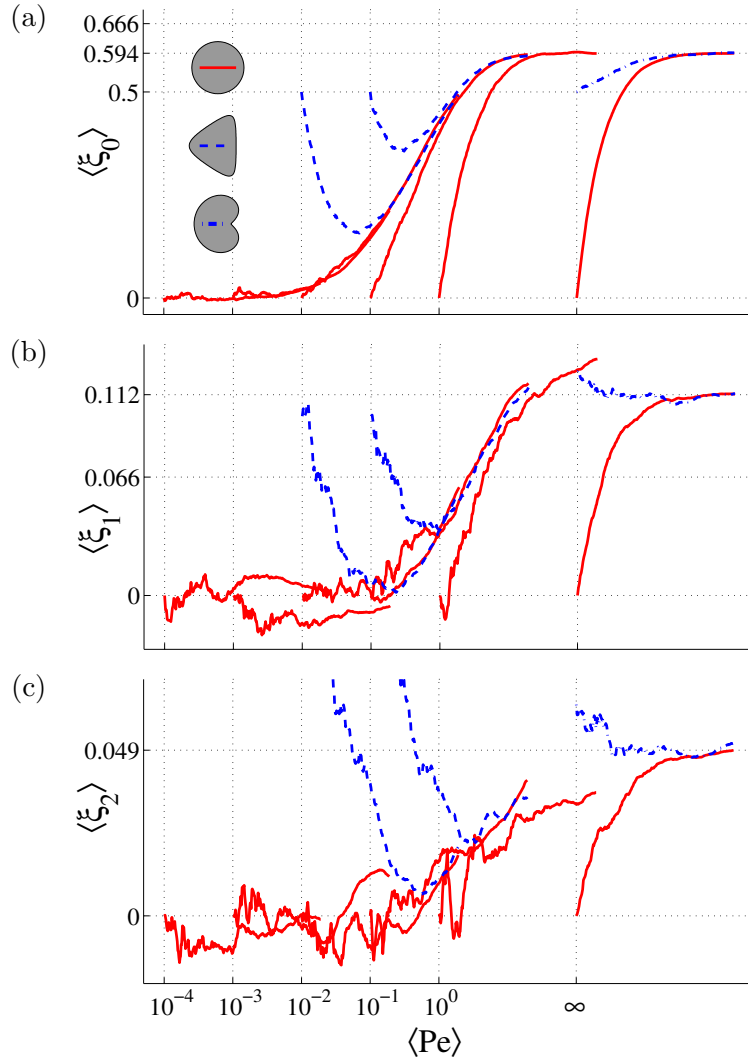
Figure 3-4: (a) $\langle \xi_0 \rangle$, (b) $\langle \xi_1 \rangle$ and (c) $\langle \xi_2 \rangle$ as functions of $\langle Pe \rangle$ for various flow speeds, ($Pe_o = 10^{-4}, 10^{-3}, \cdots, 1, \infty$) and different seeds (disk, triangle and $G_c(w)$).

$k \geq 1$. If ADLA converges to a shape (upto the scaling of $A_1(t)$) as we argue in Sec. 3.1, it will be determined by those ratios.

Therefore, we look into the changes of the rescaled Laurent coefficients, $\xi_k = -A_{-k} / A_1$. Note that, although A_{-k} (thus ξ_k) is generally a complex number for $k \geq 1$, we only take the real part for the ensemble average. For each cluster with $\{A_{-k}\}$, we can assume that the "conjugated" cluster with $\{\overline{A_{-k}}\}$ also exists in the ensemble. We grow 200 or more clusters of $n = 10^5$ particles for each of the following combinations of different seeds and flow speed: for a circular seed $(g_0(w) = w)$, we use the flow speed, $\mathrm{Pe}_o = 10^{-4}, 10^{-3} \cdots, 10^0, \infty$, and, for a triangular seed $(g_0(w) = w - 0.5 - 0.1/w - 0.2/w^2)$, $\mathrm{Pe}_o = 10^{-2}, 10^{-1}$. (We will explain the third choice of seed Sec. 3.3.) The simulation with $\mathrm{Pe}_o = \infty$ means that we use the probability $p_\infty(\theta)$ right from the beginning of the growth. This helps the clusters to reach at the asymptotic limit fast. To reduce fluctuation, we use small particle, $\lambda_0 = 1/16$.

In Fig. 3-4, we plot $\langle \xi_k \rangle$ for $k = 0, 1$, and 2 as functions of $\langle \mathrm{Pe} \rangle = \mathrm{Pe}_o \langle A_1(t_n) \rangle$ since Pe is the proper parameter for the crossover. As seen in Fig. 3-4(a), $\langle \xi_0 \rangle$ eventually approaches to a value close to 0.6 independent of its starting point. One can easily identify the curve of the stable attractor starting from 0 and approaching to 0.6. The next two variables shown in Fig. 3-4(b)$\sim$(c) exhibit similar patterns although fluctuations are larger and convergence takes more time. From the simulations with $\mathrm{Pe}_o = \infty$, we obtain the following asymptotic values of the coefficients,

$$\langle \xi_0^\infty \rangle = 0.594 \pm 0.049, \tag{3.16}$$

$$\langle \xi_1^\infty \rangle = 0.112 \pm 0.079, \tag{3.17}$$

$$\langle \xi_2^\infty \rangle = 0.049 \pm 0.064, \tag{3.18}$$

where $\xi_k^\infty = \lim_{n \to \infty} \xi_k(t_n)$. As fluctuations of higher coefficients $(k \geq 3)$ are significantly large, we are not sure whether they reach at their asymptotic values at $n = 10^5$. Thus, we do not report the values here. Indeed, in Sec. 3.5, we show that the coefficients are still moving toward to the asymptotic values.
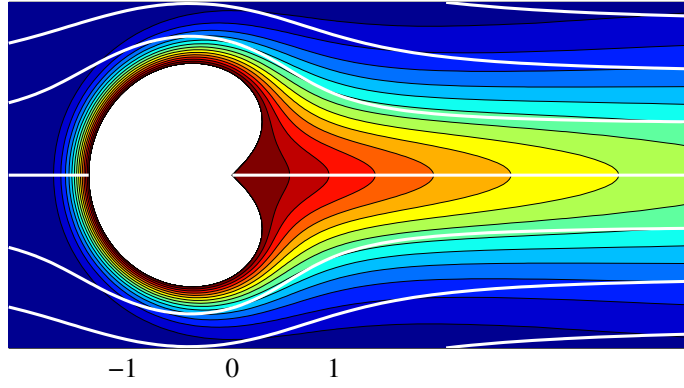
Figure 3-5: The exact, asymptotic shape of the continuous dynamics, $G_c(w)$, which describes solidification in a fluid flow.
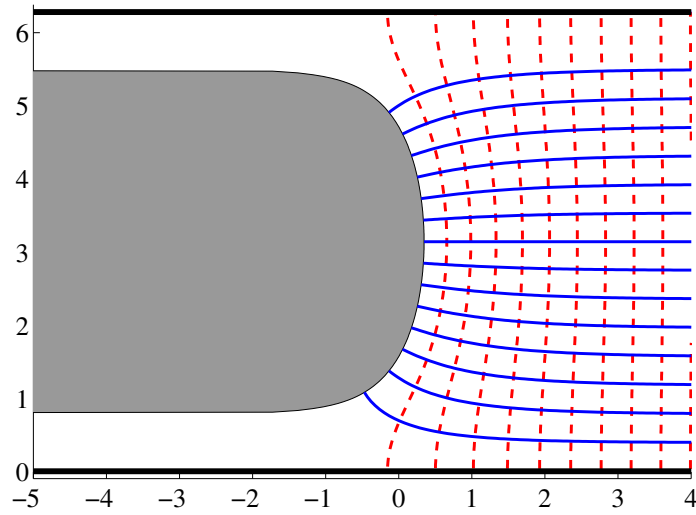
Figure 3-6: The Saffman-Taylor finger with the filling fraction $\lambda = 3/4$.

3.3 A Similarity Solution of Continuous Growth

Continuous growth limited by advection-diffusion is described by the generalized Polubarinova-Galin equation, Eq. (2.10),

$$\mathrm{Re}\left\{\overline{wg'(w)}g_t(w)\right\} = \alpha\,\sigma(w;\mathrm{Pe}_o A_1(t)\,) \qquad \text{for} \qquad |w| = 1. \tag{3.19}$$

This equation also models the solidification from a flowing melt, and the asymptotic solutions in low-Pe limit are only known [64]. Here we present a high-Pe asymptotic solution; when the flux density is given by the high-Pe asymptotic solution as

$$\alpha\,\sigma(\theta;\mathrm{Pe}(t)) = \sqrt{\mathrm{Pe}(t)}\,\sin(\theta/2) = 4\sqrt{\mathrm{Pe}_o A_1(t)}\,p_\infty(\theta) \tag{3.20}$$

for *all* range of Pe, the continuous dynamics, Eq. (3.19), admits an exact solution of the form, $g(w,t) = A_1(t)\,G_c(w)$, where

$$A_1(t) = \mathrm{Pe}_o^{1/3}\,t^{2/3}, \tag{3.21}$$

$$G_c(w) = w\,\sqrt{1 - 1/w}. \tag{3.22}$$

This solution describes the long-time limit of the continuous growth for all $\mathrm{Pe}_o > 0$.

We decouple the growing radius $A_1(t)$ from Eq. (3.19) in order to find the equation required for $G_c(w)$. Any solution of $A_1(t)$ and $G_c(w)$ should satisfy the following variable-separated equations,

$$A_1'(t)\,A_1(t) = 4C\,\sqrt{\mathrm{Pe}_o A_1(t)} \tag{3.23}$$

$$\mathrm{Re}\left\{\overline{wG_c'(w)}G_c(w)\right\} = \frac{1}{C}\,p_\infty(w), \tag{3.24}$$

where $C = 1/6$ for $G_c(w)$ in Eq. (3.22) but not necessarily so for the possible other solutions. Following Hastings [50], we use properties of Poisson kernel [65] to obtain another representation of Eq. (3.24):

$$\frac{G_c(w)}{wG_c'(w)} = \frac{1}{2\pi C}\int_0^{2\pi} d\theta\,\frac{p_\infty(\theta)}{|G_c'(e^{i\theta})|^2}\frac{w + e^{i\theta}}{w - e^{i\theta}}. \tag{3.25}$$

Then, by comparing both sides at $|w| = \infty$, we determine the constant C by

$$C = \frac{1}{2\pi} \int_0^{2\pi} d\theta \; p_\infty(\theta) \, |G_c'(e^{i\theta})|^{-2}. \tag{3.26}$$

We conjecture that Eq. (3.22) is the unique solution of Eqs. (3.25)~(3.26) for $p_\infty(\theta)$ given from ADLA. It is based on that the singularity of $p_\infty(\theta)$ at $\theta = 0$ is related to the square-root factor of $G_c(w)$, but we can not provide a rigorous proof. The stability of $G_c(w)$ is also in question; however, it is unimportant since the finite-time singularities are likely to be developed under small perturbation as in the Laplacian growth without surface tension.

It is interesting to notice a coincident relation between the continuous dynamics of ADLA and the viscous fingering in a channel. The map,

$$z = \log G_c(w), \quad 0 \le \arg z < 2\pi \tag{3.27}$$

is the time-independent part of the Saffman-Taylor finger solution traveling in $\hat{\boldsymbol{x}}$ direction with the *filling fraction* of 3/4. (See Fig. 3-6.)

Just as the Saffman-Taylor finger solutions have been compared to DLA in a channel geometry [22], the asymptotic solution of continuous growth, $G_c(w)$, begs comparison with the average shape of ADLA clusters. Although we will directly compare them in Secs. 3.4, we already have a clue. The rescaled Laurent coefficients of $G_c(w)$ obtained from the expansion of Eq. (3.22),

$$\xi_0^c = \frac{1}{2}, \quad \xi_1^c = \frac{1}{8}, \quad \xi_2^c = \frac{1}{16}, \qquad \cdots \quad, \quad \xi_k^c = \frac{(2k-1)\cdots 3 \cdot 1}{2^{k+1} \, (k+1)!} \tag{3.28}$$

are slightly different from those of stochastic growth in Eq. (3.16)~(3.18).

The convergence of ξ_k shows a quantitative difference between $G_c(w)$ and $\langle G_\infty(w) \rangle$ as the values of coefficients in Eqs. (3.16)~(3.18) are different from those of the similarity solution in Eq. (3.28). In order to check the possibility that $G_c(w)$ is another asymptotic shape of stochastic dynamics belonging to a different basin of attraction, we grow ADLA clusters using $G_c(w)$ as a seed. It turns out to be not the case; as Fig. 3-4 shows, $\langle \xi_k \rangle$ starts from ξ_k^c at $\mathrm{Pe}_o = \infty$, but eventually converges to $\langle \xi_k^\infty \rangle$.

42

3.4 The Average Shape of Stochastic Growth

The conformal mapping formulation helps define the average cluster. For an ensemble of stochastic aggregates, a natural definition of the average cluster shape would be the conformal map, $\langle g(w,t) \rangle$, defined by averaging at a point, $w \in \Omega_w$, all the maps at the same time, t [22]. Since the aggregates are growing over time, however, we rather consider the ensemble average of the rescaled map,

$$G(w,t) = \frac{g(w,t)}{A_1(t)} = w - \xi_0(t) - \frac{\xi_1(t)}{w} - \frac{\xi_2(t)}{w^2} - \cdots, \qquad (3.29)$$

and seek the asymptotic limit, $\langle G_\infty(w) \rangle = \lim_{n \to \infty} \langle G(w, t_n) \rangle$.

In the left column of Fig. 3-7, we plot the evolution of the average contour of the ensemble, $\langle G_n(e^{i\theta}) \rangle$ from $n = 10^3$ to $n = 10^5$ along with the continuous growth solution, $G_c(e^{i\theta})$. To give a sense of fluctuations, we also plot a "cloud" of points, $G_n(e^{i\theta})$ for uniformly sampled values of θ. In the right column is the zoom-in of the boxed region around the branch point near $z = 0$. The cloud in the right column is a set of points, $G_n(e^{i\theta})$ at $\theta = 0$, i.e., $G_n(1)$, which shows the fluctuation around the average contour near $z = 0$.

Two important observations are as follows. First, we clearly see the convergence of $\langle G_n(w) \rangle$. Although the fluctuation of points (thickness of cloud) around the mean is relatively large and decreases very slowly (see below), the contour of $\langle G_n(w) \rangle$ is well-defined and becomes steadystate from $n = 10^3$. The exception is the region around the branch point; however, the convergence is easily extrapolated. The average contour, $\langle G_n(w) \rangle$, is approaching the asymptotic contour, $\langle G_\infty(w) \rangle$, which will be derived in Sec. 3.5. The convergence to $\langle G_\infty(w) \rangle$ looks universal in the range of our numerical experiment. ADLA clusters grown with other initial conditions converged to the same average contour. Second, $\langle G_\infty(w) \rangle$ is different from $G_c(w)$ although they are quite similar. The contour $\langle G_\infty(w) \rangle$ better captures the ensemble morphology reflected by the cloud pattern than $G_c(w)$ does. The difference is also conspicuous in the opening angles of the two curves at the branch point; while $G_c(w)$ makes $90°$, $\langle G_\infty(w) \rangle$ makes $101°$.

We investigate the fluctuation of the cloud during growth. In a similar way to the previous investigation of *penetration depth* of DLA [26, 37], we decompose the fluctuation
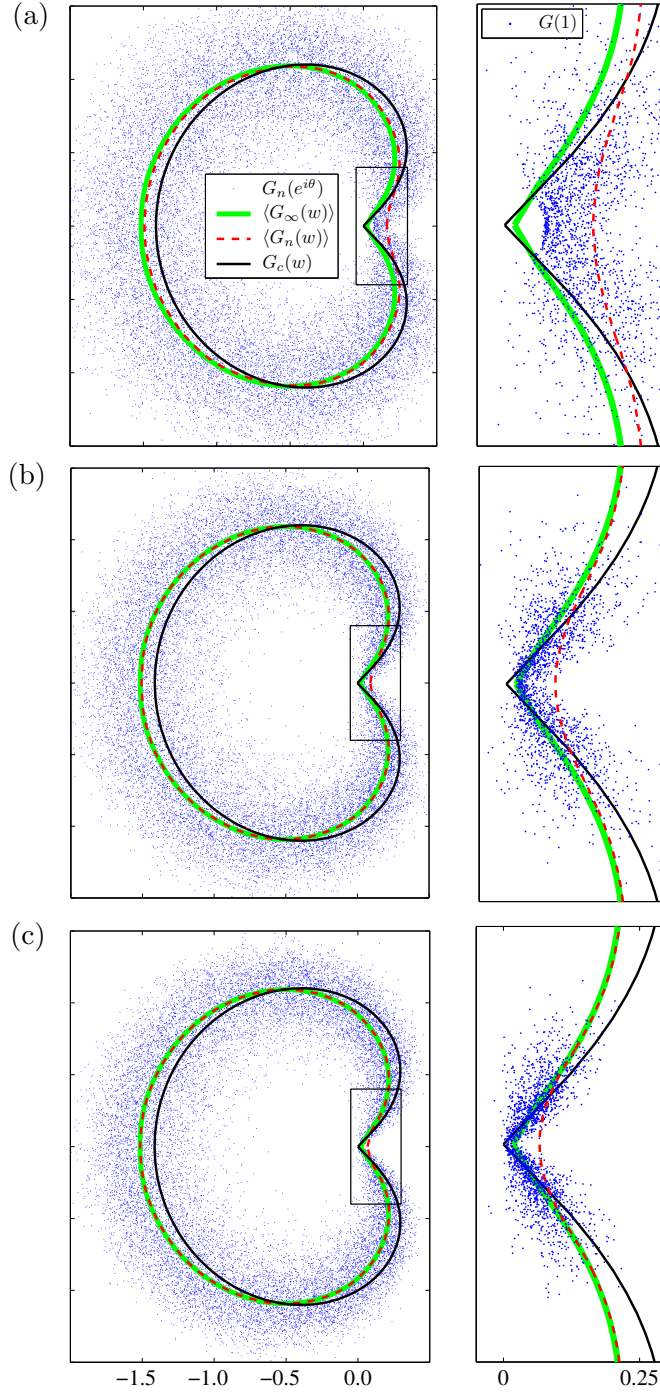
Figure 3-7: The convergence of the average cluster shape, $\langle G_n(e^{i\theta}) \rangle$ (dashed) from (a) $n = 10^3$, (b) $n = 10^4$ to (c) $n = 10^5$. The contour slowly approaches to $\langle G_\infty(e^{i\theta}) \rangle$ (thick gray), which is similar to but different from the continuous growth solution, $G_c(e^{i\theta})$ (solid). The "cloud" of the uniformly sampled points, $G_n(e^{i\theta})$ (dot) shows the width of the band slightly decreasing. On the right is the zoom-in of the branch point, $z = 0$, where we show the cloud of images only from $\theta = 0$, $G(1)$.

into

$$G_n(e^{i\theta}) - \langle G_n(e^{i\theta}) \rangle = \gamma(\theta) \left(\Delta T_n(\theta) + i \Delta R_n(\theta) \right), \tag{3.30}$$

where $\gamma(\theta)$ is a unit complex number in the direction of the tangent at $\langle G_n(e^{i\theta}) \rangle$, and ΔT_n and ΔR_n are tangential and normal components of deviation respectively. We observe both $\sqrt{\langle \Delta T_n^2 \rangle}$ and $\sqrt{\langle \Delta R_n^2 \rangle}$ satisfy the asymptotic scalings in the form, $\alpha + \beta N^{-0.3}$, consistent to Somfai et al. [26, 37]. Thus, the rescaled ADLA clusters have non-vanishing fluctuation. Unlike DLA, however, the amount of fluctuation, α, shows dependence on the angle θ; α for tangential component increases from 0.07 to 0.17 and for radial component from 0.04 to 0.17 as θ increase from 0 to π. This is because the tip of a cluster becomes farther from the origin as θ goes to π. The magnitude of α for ΔT_n and ΔR_n does not show significant difference except for θ close to 0.

The slow convergence around the branch point is attributed to the formation of a "cusp" resulting from the singularity of the growth probability, $p_\infty(\theta)$, at $\theta = 0$. We note that the points of $G(1)$ are sharply split along the two lines of $\langle G_\infty(w) \rangle$ as shown in the right column of Fig. 3-7. Thus, $\langle G_n(1) \rangle$ approach $\langle G_\infty(1) \rangle$ from left as the fluctuation decreases slowly. On the other hand, $\langle G_n(w) \rangle$ away from the origin does not have any preferred direction in convergence; thus, $\langle G_n(w) \rangle$ is close to $\langle G_\infty(w) \rangle$ even when the cluster is small and the fluctuation is large. Since the fluctuation does not vanish at $\theta = 0$, we infer that $\langle G_\infty(1) \rangle > 0$ and the contour, $\langle G_\infty(w) \rangle$, around $w = 1$ is not a cusp but a smooth curve with a very large curvature.

3.5 Dynamics of Conformal Map and Mean-Field Approximation

In this section, we give in-depth analysis regarding why stochastic growth and continuous growth have different asymptotic shapes. We look into the stochastic dynamics of the rescaled map, $G_n(w)$. Since $\lambda_n \sim O(1/n)$ as $n \to \infty$ for growing aggregates [43], we can seek the recurrence relation of $G_n(w)$ in the linear approximation for $\lambda \ll 1$. The bump function, Eq. (2.14), can be approximated as

$$\phi_{\lambda,\theta}(w) \sim w + a\lambda H_\theta(w), \qquad H_\theta(w) = w \frac{w + e^{i\theta}}{w - e^{i\theta}}. \tag{3.31}$$
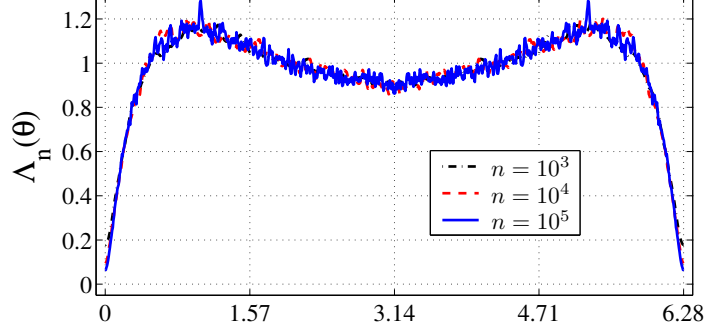
Figure 3-8: The angular profile of the Jacobian factor, $\Lambda_n(\theta)$, which shows how the size of bump preimages vary on the unit circle. Simulations with circular bump ($a = 1/2$) at three stages of growth simulations, $n = 10^3$ (dash-dot), $n = 10^4$ (dashed) and $n = 10^5$ (solid). Λ_n reaches at the steadystate profile independent of seed or bump shape.

Then it follows that, using Eq. (3.10),

$$
\begin{aligned}
G_{n+1}(w) &= (1+\lambda)^{-a}\, G_n \circ \phi_{\lambda,\theta}(w) \\
&\sim (1 - a\lambda)\,(G_n(w) + a\lambda H_\theta(w)G'_n(w)) \\
&\sim G_n(w) + a\lambda\,(\,H_\theta(w)G'_n(w) - G_n(w)\,),
\end{aligned}
\tag{3.32}
$$

where (λ, θ) denote the parameters for the $(n+1)$-th bump.

Before taking on a full-scale analysis on the map $G_n(w)$, we first examine its "center of charge," $\xi_0(t_n)$. The corresponding recurrence relation for $\xi_0(t_n)$ is obtained from the Laurent series expansion of Eq. (3.32):

$$
\xi_0(t_{n+1}) = \xi_0(t_n) - a\lambda\,(\,2e^{i\theta} + \xi_0(t_n)\,).
\tag{3.33}
$$

The steadystate ensemble of ξ_0 satisfy

$$
\langle \xi_0(t_n) \rangle = \int_0^{2\pi} d\theta\, p_\infty(\theta) \langle \xi_0(t_{n+1}) \rangle \,,
\tag{3.34}
$$

and, using Eq. (3.33), we obtain the fixed-point condition,

$$
\int_0^{2\pi} d\theta\, p_\infty(\theta) \langle \lambda \xi_0^\infty \rangle \sim -2 \int_0^{2\pi} d\theta\, p_\infty(\theta) \langle \lambda \cos\theta \rangle.
\tag{3.35}
$$

A naive answer for $\langle \xi_0^\infty \rangle$ would be $-2 \int_0^{2\pi} d\theta\, p_\infty(\theta) \cos(\theta) = 2/3$ with λ canceled out, but this value is not close to Eq. (3.16). Since the average shape is not radially symmetric, we

46

have to consider the angle dependence of λ from Eq. (2.15).

Thus we introduce the conditional probability density,

$$\Lambda_n(\theta) = \frac{\langle |G'_n(e^{i\theta})|^{-2} \rangle}{\int_0^{2\pi} d\theta' \, p_\infty(\theta') \, \langle |G'_n(e^{i\theta'})|^{-2} \rangle}. \tag{3.36}$$

proportional to the average local size of a bump's preimage (Jacobian factor), $\langle \lambda \rangle$, at the angle θ. In the definition, we use $G_n(w)$ rather than $g_n(w)$ so that the equation we derive can be written by the rescaled variables only. In fact, the difference in the values from the two definition is significantly small for large n as the relative deviation of A_1 is negligible as $n \to \infty$ [26, 37]. With the introduction of Λ_n, Eq. (3.35) yields

$$\langle \xi_0^\infty \rangle = -2 \int_0^{2\pi} d\theta \, p_\infty(\theta) \, \Lambda_\infty(\theta) \cos \theta, \tag{3.37}$$

where we use $\langle \lambda \, \xi_0^\infty \rangle = \langle \lambda \rangle \langle \xi_0^\infty \rangle$ since ξ_0^∞ does not appear in $G'_\infty(w)$.

It is not possible to derive average Jacobian, $\Lambda_n(\theta)$, a priori, but is possible to obtain it from the ensemble of the ADLA clusters. We collect the values of $1/|G'_n(e^{i\theta})|^2$ at 10^4 equally distributed values of θ over $[0, 2\pi)$ and average them over the 2000 clusters. In Fig. 3-8(a), we show the curves of $\Lambda_n(\theta)$ for $n = 10^3$, 10^4 and 10^5. Surprisingly the three curves are identical enough for us to conclude that $\Lambda_{10^5}(\theta)$ is a good approximation of $\Lambda_\infty(\theta)$. With $\Lambda_\infty(\theta) = \Lambda_{10^5}(\theta)$, Eq. (3.37) indeed gives the same value as Eq. (3.16).

The fast convergence of $\Lambda_n(\theta)$ is a dual problem to the slow convergence of $\langle G_n(w) \rangle$. The stretching factor, $|G'_n(w)|$, becomes large at the cusp near $z = 0$. In the averaging of $\Lambda_n(\theta) \propto |G'_n(e^{i\theta})|^{-2}$, however, the contribution from the cusp is negligible. Thus, $\Lambda_n(\theta)$ can be viewed as an optimal way of averaging, with which we avoid the influence of the large fluctuation of $\langle G_\infty(w) \rangle$. This argument suggests that the fast converging $\Lambda_n(\theta)$ dominates the morphology of ADLA dynamics, enabling us to obtain $\langle G_\infty(w) \rangle$ from $\Lambda_\infty(\theta)$. We observe that $\Lambda_n(\theta)$ approaches to the same $\Lambda_\infty(\theta)$ for simulations with all initial conditions. It confirms the universal crossover in Sec. 3.4.

Now the analysis for $G_n(w)$ can be done in a similar way. The steadystate and fixed point conditions for the ensemble of $G_n(w)$, corresponding to Eqs. (3.34) and (3.35), are

given by

$$\langle G_n(w) \rangle = \int_0^{2\pi} d\theta \, p_\infty(\theta) \langle G_{n+1}(w) \rangle, \tag{3.38}$$

$$\int_0^{2\pi} d\theta \, p_\infty(\theta) \langle \lambda G_\infty(w) \rangle \sim \int_0^{2\pi} d\theta \, p_\infty(\theta) \langle \lambda G'_\infty(w) \rangle H_\theta(w). \tag{3.39}$$

Then we arrive at a nonlinear integro-differential equation for the limiting average cluster shape, $\langle G_\infty(w) \rangle$:

$$\frac{\langle G_\infty(w) \rangle}{\langle G_\infty(w) \rangle'} = \int_0^{2\pi} d\theta \, p_\infty(\theta) \, \Lambda_\infty(\theta) \, H_\theta(w) \tag{3.40}$$

$$\Lambda_\infty(\theta) = \frac{\langle |G'_\infty(e^{i\theta})|^{-2} \rangle}{\int_0^{2\pi} d\theta' \, p_\infty(\theta') \, \langle |G'_\infty(e^{i\theta'})|^{-2} \rangle}, \tag{3.41}$$

which is indeed the all-coefficients version of Eq. (3.37). To derive Eqs. (3.40)~(3.41), however, we need assumptions that λ is correlated with neither $G_\infty(w)$ nor $G'_\infty(w)$, i.e.,

$$\int_0^{2\pi} d\theta \, p_\infty(\theta) \langle \lambda G_\infty(w) \rangle \approx \langle G_\infty(w) \rangle \int_0^{2\pi} d\theta \, p_\infty(\theta) \langle \lambda \rangle \tag{3.42}$$

$$\int_0^{2\pi} d\theta \, p_\infty(\theta) \langle \lambda G'_\infty(w) \rangle H_\theta(w) \approx \langle G'_\infty(w) \rangle \int_0^{2\pi} d\theta \, p_\infty(\theta) \langle \lambda \rangle H_\theta(w). \tag{3.43}$$

We verify that they are very accurate approximations. In fact, we expect some positive correlation between $G_n(w)$ and $\lambda(\theta)$ for $w = e^{i\theta}$. When $G_n(w)$ is outside of the average contour, $\langle G_n(e^{i\theta}) \rangle$, then the point is more likely to be around a tip than in a fjord of the cluster; thus, λ is likely bigger than the average $\langle \lambda \rangle$. Indeed, the measured correlation values supports this argument; the correlation coefficient,

$$\frac{\langle G_n \lambda_n \rangle - \langle G_n \rangle \langle \lambda \rangle}{\sqrt{\text{Var}\{G_n\} \, \text{Var}\{\lambda_n\}}}, \tag{3.44}$$

for $n = 10^5$ varies from 0.129 to 0.247 as a functions of θ. However, this correlation seems to be canceled out in the contour integral of Eq. (3.42). On the other hand, the correlation between G'_n and λ_n is already negligible; the coefficient similar to Eq. (3.44) ranges from 0.011 to 0.015. We believe it is because a typical image of $G_n(w)$ erratically varies as $n \to \infty$ since it is the perimeter of a fractal object, and thus the derivative $G'_n(w)$ is hardly correlated to $\lambda(\theta)$, i.e., whether $G_n(e^{i\theta})$ is in a tip or a fjord.

The validity of Eqs. (3.40)~(3.41) (and the assumptions leading to it) can be checked by
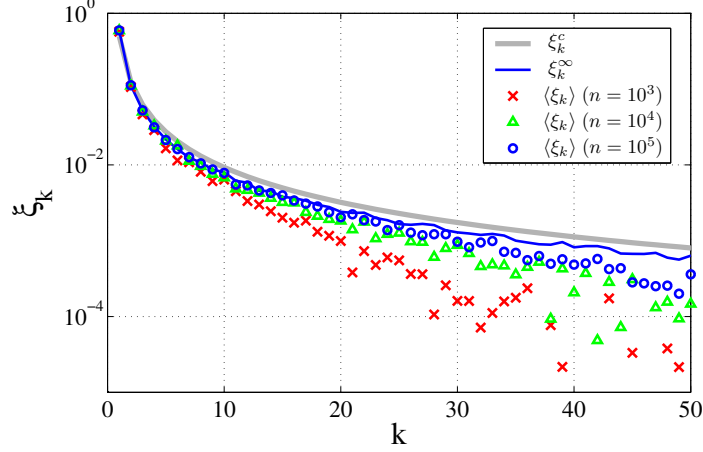
Figure 3-9: The rescaled Laurent coefficients, $\langle \xi_k(t_n) \rangle$, of an ensemble of ADLA clusters at $n = 10^3$(cross), $n = 10^4$(triangle) and $n = 10^5$(circle). They slowly converge to the asymptotic values, $\langle \xi_k^\infty \rangle$ (solid), obtained from $\Lambda_\infty(\theta) = \Lambda_{10^5}(\theta)$. We also show the coefficients, ξ_k^c (thick gray), of continuous growth solution, $G_c(w)$, for comparison.

solving for $\langle G_\infty(w) \rangle$ using $\Lambda_\infty(\theta)$. We expand $\langle G_\infty(w) \rangle$ by the Laurent series with $\{\langle \xi_k^\infty \rangle\}$ and obtain the recurrence relations for the coefficients as

$$\langle \xi_k^\infty \rangle = \frac{1}{k+1} \left(I_{k+1} + \sum_{j=0}^{k-1} j\, \xi_j\, I_{k-j} \right), \quad I_j = -2 \int_0^{2\pi} d\theta\, p_\infty(\theta)\, \Lambda_\infty(\theta)\, \cos(j\theta) \qquad (3.45)$$

for $k \geq 1$. (The case of $k = 0$ is Eq. (3.37).) We calculate $\langle \xi_k^\infty \rangle$ for $0 \leq k \leq 400$ and reconstruct $\langle G_\infty(w) \rangle$ using discrete Fourier transform. The contour of $\langle G_\infty(w) \rangle$ ($|w| = 1$) is shown in Fig. 3-7, and we see it is the correct extrapolation curve of $\langle G_n(w) \rangle$ as $n \to \infty$. In Fig. 3-9 we show the first 50 values of $\langle \xi_k(t_n) \rangle$ approaching $\langle \xi_k^\infty \rangle$ from Eq. (3.45). For higher coefficients, which are responsible for the cusp, the convergence is slow as expected from Fig. 3-4. The coefficients of the asymptotic solution, ξ_k^c, are also shown for comparison.

With the validity of Eqs. (3.40)~(3.41) established, we may consider its mean-field version, where the ensemble average is replaced by a single conformal map, $G(w)$:

$$\frac{G(w)}{G'(w)} = \int_0^{2\pi} d\theta\, p_\infty(\theta)\, \Lambda(\theta; G)\, H_\theta(w), \qquad (3.46)$$

$$\Lambda(\theta; G) = \frac{|G'(e^{i\theta})|^{-2}}{\int_0^{2\pi} d\theta'\, p_\infty(\theta')\, |G'(e^{i\theta'})|^{-2}}, \qquad (3.47)$$

where $\Lambda(\theta; G)$ is the rescaled Jacobian of the function $G(w)$.

Not surprisingly, these equations are equivalent to Eqs. (3.25)~(3.26). Thus, the sim-
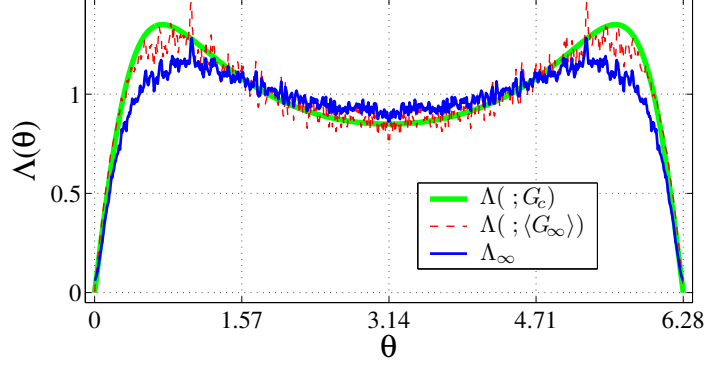
Figure 3-10: $\Lambda_\infty = \Lambda_{10^5}$ (solid) in comparison with the Jacobian factors defined from two different single functions: $\Lambda(\theta; G_c) \propto |G_c|^{-2}$ (thick gray) and $\Lambda(\theta; \langle G_\infty \rangle) \propto |\langle G_\infty \rangle'|^{-2}$ (dashed).

ilarity solution, $G_c(w)$, can be interpreted as a self-consistent mean-field approximation for the average conformal map, $\langle G_\infty(w) \rangle$. This mean-field approximation also tells us the source of the slight difference between $\langle G_\infty(w) \rangle$ and $G_c(w)$: the nonlinear averaging, $\langle |G_\infty|^{-2} \rangle$ in Eq. (3.41). Substituting $G = \langle G_\infty \rangle$ into Eqs. (3.46)$\sim$(3.47) does not render Eqs. (3.40)$\sim$(3.41) since $\Lambda_\infty(\theta) \neq \Lambda(\theta; \langle G_\infty \rangle)$ in general. In Fig. 3-10, we show the two Jacobian factors, $\Lambda_\infty(\theta)$ and $\Lambda(\theta; \langle G_\infty \rangle)$ as well as $\Lambda(\theta; G_c)$. We obtain $\Lambda(\theta; \langle G_\infty \rangle)$ from $\langle G_\infty(w) \rangle$ numerically and $\Lambda(\theta; G_c)$ from G_c in an analytic form,

$$\Lambda(\theta; G_c) = \frac{3}{\pi} \frac{8 \sin(\theta/2)}{8 \sin^2(\theta/2) + 1}. \tag{3.48}$$

The nonlinear average, $\Lambda_\infty(\theta)$, shows a small but significant difference from the similar quantity from the linear average, $\Lambda(\theta; \langle G_\infty \rangle)$, especially at $\theta = \pi/4$ and $7\pi/4$. It is interesting to note that, although $\Lambda(\theta; \langle G_\infty \rangle)$ closely resembles $\Lambda(\theta; G_c)$, the pair $\{G_\infty, \Lambda(\,\cdot\,; G_\infty)\}$ is not the solution to Eq. (3.46).

3.6 Implication on Transport-Limited Aggregation

We believe that the assumptions and arguments leading to the results in Secs. 3.5 generally hold for the general transport-limited growth model we developed in Chap. 2. In fact, we have presented the main results, Eqs. (3.24), (3.26), (3.40)$\sim$(3.41) and (3.46)$\sim$(3.47) (with $G = G_c$) in general forms, so they should hold for $p_\infty(\theta)$ derived from other models in the class of TLA. Thus, continuous dynamics should be a mean-field theory for the

corresponding stochastic dynamics.

We also claim that the deviation of the averaged cluster shape from the continuous dynamics solution, i.e., $\Lambda_\infty \neq \Lambda(\,;\langle G_\infty \rangle)$, is general in TLA. An exception is DLA in radial geometry; the radial symmetry implies the trivial solution, $\langle G_\infty(w) \rangle = w$ and $\Lambda_\infty(\theta) = \Lambda(\theta;\langle G_\infty \rangle) = 1$. However, the identity between the mean-field approximation and the average cluster shape will be removed when the symmetry is broken.

We consider the the following two cases. First, the symmetry can be broken from the boundary conditions. A recent simulation of DLA in a channel geometry with the reflective boundary condition [22] shows a consistent result with ours. The average cluster shape is reported to be similar, but not identical, to any Saffman-Taylor "finger," which solves the continuous dynamics. We expect that analogous equations to Eqs. (3.40)~(3.41), relating $\langle G_\infty(w) \rangle$ and $\langle |G'_\infty(e^{i\theta})|^{-2} \rangle$, will also hold in a channel geometry. The Saffman-Taylor fingers are exact solutions to the mean-field approximation, but not solutions to the exact equations.

Second, the model can have an asymmetric growth probability as in the case of ADLA. Here we suggest a qualitative argument explaining the difference between Λ_∞ and $\Lambda(\,;\langle G_\infty \rangle)$ observed in, but not restricted to, ADLA. As we note in Sec. 3.4, the rescaled aggregates have nonzero length scales for spatial deviation. If we ignore the radial component and assume deviations occur *on* the average contour, the ensemble of $G_\infty(e^{i\theta})$ takes the distribution of $\langle G_\infty(e^{i\,x(\theta)}) \rangle$, where $x(\theta)$ is a random variable with the mean θ and the standard deviation $\alpha(\theta)/|\langle G_\infty(e^{i\theta}) \rangle'|$. Then, it follows that Λ_∞ is approximated as the convolution of $\Lambda(\,;\langle G_\infty \rangle)$ and $\mathbf{P}_\theta$, the probability density distribution of $x(\theta)$:

$$\Lambda_\infty(\theta) \approx \int_0^{2\pi} d\theta' \, \Lambda(\theta';\langle G_\infty \rangle) \, \mathbf{P}_\theta(\theta'). \tag{3.49}$$

This relation explains the pattern in Fig. 3-10 that $\Lambda_\infty(\theta)$ looks like a relaxed profile from $\Lambda(\theta;\langle G_\infty \rangle)$ under a diffusion-type equation. The seemingly inconsistent behavior, $\Lambda_\infty(0) \approx 0$, is because $|\langle G_\infty(e^{i\theta}) \rangle'| \gg 1$ around the cusp at $\theta = 0$, and thus $\mathbf{P}_0$ becomes a delta function. Therefore, we conclude that one should observe $\Lambda_\infty \neq \Lambda(\,;\langle G_\infty \rangle)$ for any transport-limited growth with an asymmetric growth probability.

We admit that, although Eqs. (3.40)~(3.41) are necessary conditions for the average shape of the transport-limited aggregates in the class of Eq. (2.1), it does not provide a

51

basis for a complete statistical theory. Such a theory would likely consist of an infinite set of independent equations connecting the corresponding set of independent averages on the ensemble of maps $\{G_\infty(w)\}$. The mean-field approximation, Eqs. (3.46)$\sim$(3.47), which corresponds to the continuous growth process, can be considered as a leading hierarchy of closure approximations to this set.

Chapter 4

Transport-Limited Aggregation on Curved Surfaces

Continuous and stochastic Laplacian growth models describe many out-of-equilibrium pattern formations, including diffusion-limited aggregation (DLA) [8], viscous fingering [54], (quasi-static) dendrite solidification [13], and dielectric breakdown [11]. Although real growth processes sometimes occur on curved surfaces, such as cell membranes or rock formations, the studies on these models mostly assume a flat Euclidean surface. The influence of curved surfaces has been neglected; An exceptions is the continuous growth of viscous fingering investigated by Entov and Etingof [66] and Parisio et al. [67].

In this chapter, the transport-limited growth model in Chap. 2 is extended on curved surfaces by use of conformal projections. As an application to stochastic growth, we will simulate DLA on constant curvature surfaces and investigate the fractal and the multifractal properties of the aggregates.

4.1 Description of Growth on Curved Surfaces

When a growth phenomena occurs on a non-Euclidean surface, the conformal mapping formulation can not be directly applied as complex number can not be used as a coordinate system. If there exists a conformal, i.e., angle-preserving, map between the manifold and a complex plane, however, we can describe the growth on the complex plane instead. Let $\Omega_m(t)$ be the exterior of the growing object on a non-Euclidean manifold, M, and Φ be a conformal map from a (part of) complex plane to M. Then, the domain $\Omega_m(t)$ has has its
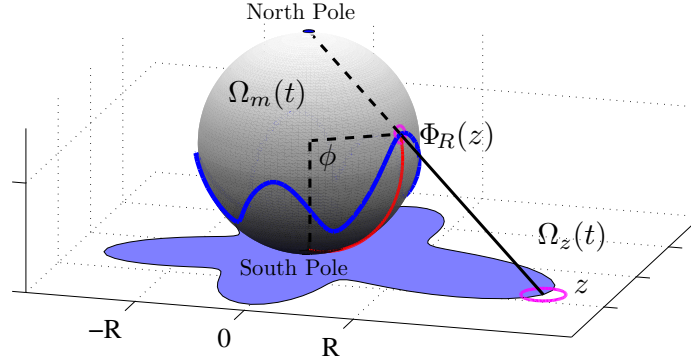
Figure 4-1: Stereographic projection, Φ^{-1}, from the exterior of the growing object $\Omega_m(t)$ on a sphere of radius R to the exterior of the shadow, $\Omega_z(t)$, on a complex plane. The point $\Phi(z)$ is projected from the north pole to the point z. The origin of the z-plane is tangent to the sphere at the south pole, and the latitudinal angle ϕ is measured from the south pole.
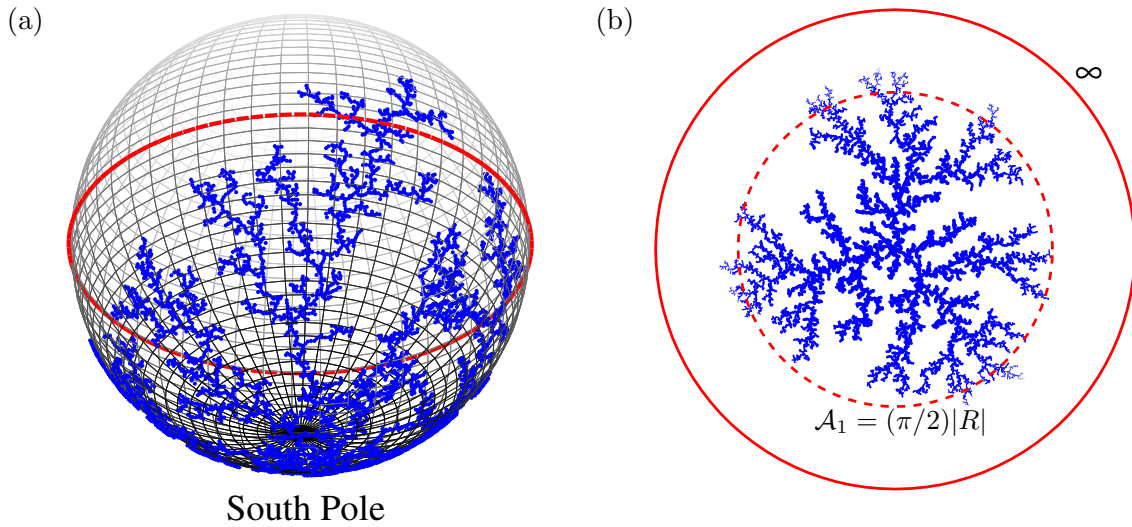
Figure 4-2: DLA clusters on the elliptic (left) and the hyperbolic (right) geometries. The elliptic geometry is isometrically embedded on the surface of a sphere and the hyperbolic geometry is visualized on the Poincaré disk with the metric, $ds = dz/(1 - (|z|/2R)^2)$. We use $R/\sqrt{\lambda_o} = 100$ and aggregate 4942 and 9001 particles to fill the great circles of radius $(\pi/2)R$ (dashed lines) in the elliptic and hyperbolic geometries respectively.

shadow, $\Omega_z(t) = \Phi^{-1}(\Omega_m(t))$, on the complex plane under the *projection* Φ^{-1}. As in the flat surface case, the growth is described by a time-dependent conformal map, $g(w, t)$, from the exterior of the unit disk, Ω_w, to the exterior of the growing shadow, $\Omega_z(t)$; however, the dynamics of $g(w, t)$ should describe $\Omega_z(t)$ in such a way that the object, $\Omega_m(t)$, follows the correct physics growth on M.

For the continuous growth on a curved manifold with a projection $\Phi(z)$, the generalized Polubarinova-Galin equation in (2.10) can be extended to

$$\text{Re}\left\{\overline{wg'(w)}g_t(w)\right\} = \frac{\alpha\, \sigma(w, t)}{|\Phi' \circ g(w)|^2} \qquad \text{for} \qquad |w| = 1, \tag{4.1}$$

where α is a constant, and $\sigma(w, t)$ is the time-dependent normal flux on the boundary of Ω_w. This result is easily obtained by substituting $\Phi \circ g$ for g in the original equation (2.10). For stochastic growth, we need to adjust the Hastings-Levitov algorithm [25] on the shadow domain. The algorithm is based on the recursive updates of the map, (2.13). The random sequence of angle, $\{\theta_n\}$, follows the probability distribution, $p(\theta, t_n) \propto \sigma(e^{i\theta}, t_n)$, invariant under the conformal maps, $g_n(w)$ and $\Phi(z)$. However, the preimage of bump area, λ_n, should be determined so that the bump area is fixed as λ_o on the manifold M. Thus, the bump size for the n-th particle is modified from Eq. (2.15) to

$$\lambda_n = \frac{\lambda_o}{|\Phi' \circ g_{n-1}(e^{i\theta_n})|^2 \cdot |g'_{n-1}(e^{i\theta_n})|^2}. \tag{4.2}$$

Note that this modification is nevertheless new. The previous studies on DLA in a channel geometry [22] can be viewed as an example, in which M is a subset of a complex plane (Euclidean), $M = \{z' : 0 \leq \text{Im } z' < 2\pi\}$ and the projection is given by $z' = \Phi(z) = \log(z)$.

Stereographic projection [63] best serves our purposes; we can apply the result above to the surface of a sphere. Stereographic projection is obtained by projecting the surface of a sphere from the north pole to a plane whose origin is tangent to the south pole; see Fig. 4-1. If Φ is an *inverse* stereographic projection with sphere of radius R, Φ^{-1} maps the point (R, ϕ, θ) in spherical coordinates to $z = R\tan(\phi/2)e^{i\theta}$ in the complex plane. Here θ is the azimuthal angle and ϕ is the latitudinal angle measured from the south pole. If the modulus, $|\cdot|$, on the sphere is defined to be distance to the origin (south pole) in the curved metric (arc-length of the great circle) in a similar way to $|\cdot|$ on a complex plane,

$|z|$ and $|\Phi(z)|$ satisfy

$$\frac{|z|}{2R} = \tan\left(\frac{|\Phi(z)|}{2R}\right). \tag{4.3}$$

The Jacobian factor of the projection is angle-independent; thus, it is given by

$$|\Phi'(z)| = \frac{d|\Phi(z)|}{d|z|} = \frac{1}{1 + (|z|/2R)^2} \tag{4.4}$$

from the derivative of Eq. (4.3). Now Eq. (4.4) can be used to continuous dynamics, Eq. (4.1), and stochastic dynamics, Eq. (4.2) on sphere.

While the surface of a sphere is a three-dimensional visualization of elliptic (or Riemannian) geometry, we can obtain a conformal project from hyperbolic geometry to a complex plane as well. Unlike elliptic geometry, hyperbolic geometry can not be isometrically embedded into 3D Euclidean space; only a part of the geometry can be embedded into 3D as a surface known as *pseudosphere*. Hyperbolic geometry has a negative constant curvature, $K = -1/R^2$, as opposed to the positive one, $K = 1/R^2$, of elliptic geometry. The projection can be obtained by simply viewing hyperbolic geometry as a surface of a sphere with an imaginary radius, iR, as suggested from the sign of curvature. The projection can be still defined; substituting iR for R alters Eqs. (4.3) and (4.4) as

$$\frac{|z|}{2R} = \tanh\left(\frac{|\Phi(z)|}{2R}\right) \qquad \text{and} \qquad |\Phi'(z)| = \frac{1}{1 - (|z|/2R)^2}. \tag{4.5}$$

The image of hyperbolic geometry under the projection is thus limited to the inside of a disk with radius $2R$, and the boundary, $|z| = 2R$, corresponds to the infinity. The stereographic projection serves as a non-isometric visualization of the geometry known as Poincaré disk. The length element dz at dz in the disk corresponds to the element $dz/(1 - (|z|/2R)^2)$ in the hyperbolic universe.

4.2 Fractal Properties of DLA on Constant Curvature Surfaces

Using the harmonic probability measure, $p(\theta) = 1/2\pi$, and the modified Hastings-Levitov algorithm with Eq. (4.2), we grow DLA clusters on curved surfaces. Fig. 4-2 shows clusters on elliptic and hyperbolic geometries. On the Poincaré disk, the size of particles becomes

Geometry	Elliptic	Euclidean	Hyperbolic
D_f	1.704±0.001	1.704±0.001	1.693±0.001
D_2/D_f	0.577±0.003	0.529±0.006	0.527±0.001
D_3/D_f	0.591±0.006	0.503±0.005	0.499±0.001
D_4/D_f	0.617±0.012	0.486±0.004	0.482±0.001
D_5/D_f	0.631±0.018	0.473±0.004	0.469±0.001

Table 4.1: The fractal dimension D_f and the multifractal dimensions D_q of DLA clusters on three different geometries.
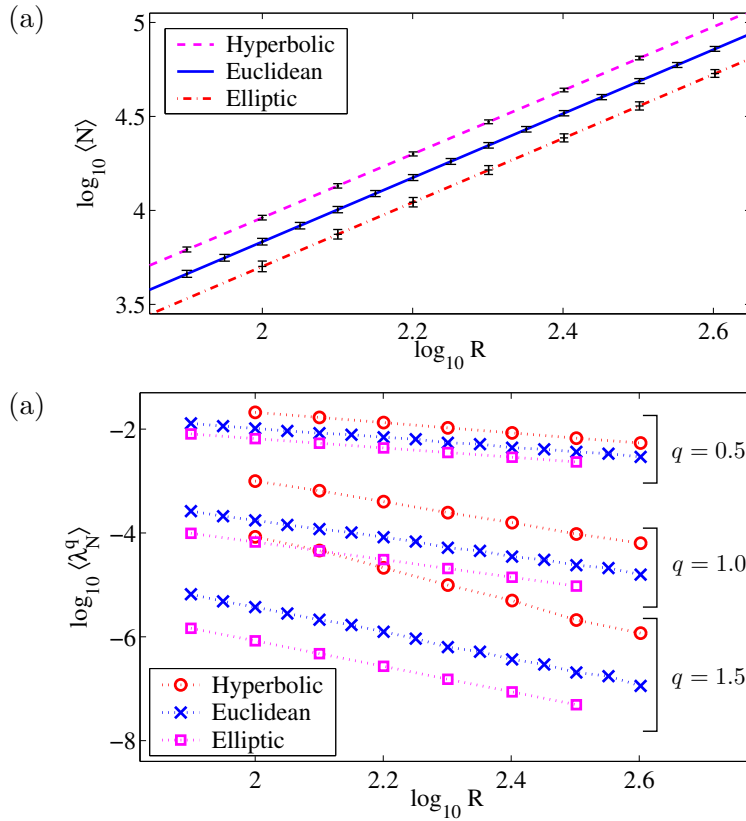
Figure 4-3: (a) The average number of particles to fill the disk of radius $\mathcal{A}_1 = (\pi/2)R$, $\langle N \rangle$, as a function of the radius R on the three geometries. (b) Moments of λ_N, $\langle \lambda_N^q \rangle$, as functions of R.

smaller and smaller as they approach the infinity, $|z| = 2R$.

An analytic advantage of the conformal mapping formulation is that the Laurent expansion of $g(w,t)$ gives us information on the moments of the cluster; the *conformal radius*, A_1, and the *center of charge*, A_0, come from the first two terms of the expansion, $g(w) \approx A_1 w + A_0$. Such coefficients from DLA clusters on curved surfaces are not useful as they are the moments of the shadow, not the original cluster. Using the property that circles are mapped to circles under a (inverse) stereographic, it is possible to define the quantities corresponding to A_1 and A_0. We note that the image, $\Phi(A_1 w + A_0)$, of the unit circle, $|w| = 1$, is also a circle on M, and it is the one that best approximate the cluster and the far-field in $\Omega_m(t)$. Thus, we define the conformal radius, $\mathcal{A}_1$, and the center of charge, $\mathcal{A}_0$, on M to be the radius and the deviation of $\Phi(A_1 w + A_0)$ respectively:

$$\mathcal{A}_1 = \frac{1}{2} \{ \, |\Phi(A_1 + |A_0|)| + |\Phi(A_1 - |A_0|)| \, \}, \tag{4.6}$$

$$\mathcal{A}_0 = \frac{1}{2} \{ \, |\Phi(A_1 + |A_0|)| - |\Phi(A_1 - |A_0|)| \, \}. \tag{4.7}$$

On curved surfaces, however, the fractal dimension D_f, can not be determined from the scaling, $n \sim \langle \mathcal{A}_1 \rangle^{D_f}$, since the geometry is not linearly scalable with $\mathcal{A}_1$; the two domains within radii of different values of $\mathcal{A}_1$ are not self-similar to each other, and the log-log plot of n versus $\mathcal{A}_1$ is not linear either. Instead, we use the sphere radius R as a relevant length scale while keeping $\mathcal{A}_1$ proportional to R for self-similarity. Thus, we grow a cluster until $\mathcal{A}_1$ reaches at $\phi_o R$ for various radius R, but with a fixed particle size, $\lambda_o = 1$, and a fixed angle $\phi_o = \pi/2$. The angle ϕ_o is as such since the circle (dashed lines in Fig. 4-2) becomes a great circle on a sphere. If N is the number of particles to fill the radius, the fractal dimension is determined from $\langle N \rangle \sim R^{D_f}$. From the statistics of 1000 clusters for each of R in a geometrically increasing sequence from 79 to 400, we obtain the fractal dimensions, $D_f \approx 1.70$, as shown in Table 4.1. Fig. 4-3(a) shows $\langle N \rangle$ versus R in the three geometries. The relative deviation of D_f between geometries is surprisingly small compared to the deviation of surface properties caused by the curvature. For example, the area within the radius $(\pi/2)R$ on elliptic (or hyperbolic) geometry is about 23% smaller (or larger) than the corresponding area on the Euclidean surface; however, this factor only change the prefactor, not the exponent, of the scaling, $\langle N \rangle \sim R^{D_f}$. We believe D_f is insensitive to the curvature because, on small length scale comparable to the the the particle size $\sqrt{\lambda_0}$, the surface is locally

Euclidean. This result is consistent with that of ADLA whose fractal dimension is not affected by the background flow.

The multifractal properties [39, 40] related to from the probability measure, however, seem to depend on the curvature. Following Davidovitch et al. [43], we measure the multifractal dimensions D_q from the relation,

$$\langle \lambda_N^q \rangle \sim R^{-2qD_{2q+1}}. \tag{4.8}$$

The averaging in Eq. (4.8) is made over λ_N at uniformly distributed angle. Fig. 4-3(b) shows the first three moments of λ_N as functions of R, and Table 4.1 shows D_q/D_f in the three geometries. We note that D_q for elliptic geometry are yet transient, influenced by finite-size effect. The multifractal dimensions do not satisfy the inequality $D_q > D_{q'}$ for $q < q'$ [39]. Since the space itself is finite and the distance to the *infinity* is bounded, the instability in growth is pronounced in elliptic geometry. The normalized center-of-charge fluctuation, $\langle |\mathcal{A}_0|^2 \rangle^{1/2}/R$, is about 0.3 for on elliptic geometry although it decreases as R increases. For Euclidean and hyperbolic geometries, the fluctuations are around 0.03 and 0.02 respectively. It should also be noted that the growth probability on sphere is not harmonic since the far-field potential, $-\log |z|$, on plane is mapped to the singular potential, $\log(\pi - \phi)$, around the north pole.

Even with the finite size effect, we conjecture that multifractal dimensions increase in the order of hyperbolic, Euclidean, and elliptic geometries. The justification is that, when the measurements are similarly made for smaller latitudinal angles, $\phi_o = \pi/3$ and $\pi/6$, D_q on elliptic and hyperbolic geometries converge to D_q on Euclidean plane. This also support that the slight difference in D_q between Euclidean and hyperbolic geometries are not from statistical error. We believe the dependence of D_q on curvature is related to the depth of fjords. On elliptic geometry, the circumference of a circle with radius $\phi_o R$ is $2\pi \sin \phi_o R$, shorter than $2\pi \phi_o R$ on Euclidean geometry. If we consider a pair of branches which make the same opening angle on the two geometries, the area between them is more screened on elliptic than on Euclidean geometry. Thus, we expect a different distribution of λ. Because of the competition on smaller circumference, tip-splitting events are subdued, as observed in continuous growth [67], and eventually fewer branches survive. The opposite argument applies to hyperbolic geometry, where the circumference is given by $2\pi \sinh \phi_o R$,

inter-branch area is less-screened, and tip-splitting is encouraged. A quantitative study on the spectrum of λ and the tip splitting events will be our future works.

Chapter 5

Steady advection-diffusion around finite absorbers in two-dimensional potential flows

Motivated by ADLA in Chap. 3, we provide the solution method for the advection-diffusion problem, Eqs. (3.1)∼(3.3). This boundary value problem (BVP) needs to be solved for all Pe since the normal flux density, $\sigma(e^{i\theta}; \text{Pe})$, determines the probability measure for growth events. It turns out that this problem also describes other physical systems and has been studied previously in these context. Thus, it merits serious mathematical study in its own right. It is perhaps the simplest advection-diffusion problem with a nontrivial dependence on the Péclet number. At the same time, it is also the most complicated advection-diffusion problem for which a nearly exact analytical solution is possible, as we will show.

As this chapter is somewhat independent from the others about TLA, it is organized in a self-contained way, having it own introduction and conclusion. In Sec. 5.1 we introduce the problem with its various applications. In Sec. 5.2 we set the stage for our analysis by reviewing two key properties of the BVP Eqs. (5.3)∼(5.5): (i) It can be recast as a singular integral equation in streamline coordinates, and (ii) conformal mapping can be applied to work in other convenient geometries for numerical solution and mathematical analysis. In Sec. 5.3 we present an efficient, new numerical method to solve the BVP, after conformal mapping to the interior of a circular disk. In Sec. 5.4 we derive accurate asymptotic expansions for σ for high Péclet numbers by applying an exact iterative procedure to the integral

equation. In Sec. 5.5 approximate formulae for σ are derived when Pe is sufficiently small via approximating the kernel of the integral equation and solving the resulting equation exactly by known methods. In Sec. 5.6 an accurate *ad hoc* connection formula is given for σ by combining the formulae for high and low Pe, and it is also integrated to obtain the Nu(Pe) relation. Finally, in Sec. 5.7 we conclude with a discussion of some of the implications and applications of our results, as well as by posing a few challenges for future work.

5.1   Introduction

The transfer of mass, heat, or other passive scalars in fluid flows is a major theme in transport science [68]. The canonical model problem involves a uniform background flow of speed, U_∞, and concentration, C_∞, past an absorbing object of characteristic size, L_o. Given the steady, incompressible flow field, $\boldsymbol{u}$ (scaled to U_∞), the steady tracer concentration around the object, c (scaled to C_∞), satisfies the (dimensionless) linear advection-diffusion equation,

$$\text{Pe}_o \, \boldsymbol{u} \cdot \boldsymbol{\nabla} c = \boldsymbol{\nabla}^2 c, \tag{5.1}$$

where $\text{Pe}_o = U_\infty L / D$ is the *bare* Péclet number, which measures the relative importance of advection compared to diffusion (with a diffusivity D). The partial differential equation (PDE) Eq. (5.1) must be solved subject to the boundary conditions (BCs) $c = 0$ on the object and $c = 1$ far away (at ∞), to obtain the dimensionless normal flux density,

$$\sigma = \hat{\boldsymbol{n}} \cdot \boldsymbol{\nabla} c, \tag{5.2}$$

everywhere on the surface of the object. (Since the problem is linear, we may also consider the equivalent problem of a source object at $c = 1$ relative to a depleted background fluid at $c = 0$.)

Although similarity solutions exist for infinite leading edges (see below), in the usual case of a *finite* absorber, the mathematical problem is intractable. It can even be difficult to solve numerically because Pe_o appears as a singular perturbation in the PDE in both limits, $\text{Pe}_o \to \infty$ and $\text{Pe}_o \to 0$. The classical approach, therefore, has been to employ asymptotic analysis to obtain approximate solutions, usually relating the total integrated flux, or Nusselt number, Nu, to the Péclet number, Pe. Early studies of this type focused
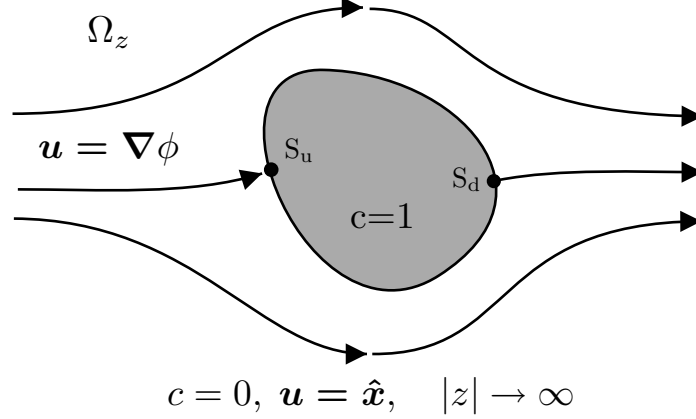
Figure 5-1: The fundamental problem of advection-diffusion: A finite absorber (source) in a steady flow of uniformly concentrated (depleted) fluid in the complex z plane; Ω_z is the region exterior to the object.

on spheres [69] and more complicated shapes [70] in Stokes flows, and later studies dealt with heat or mass transfer in steady shear flow [71]. Related work continues to the present day, e.g. in the context of nutrient uptake by single-cell organisms [72].

The Nu(Pe) relation contains useful global information, but one sometimes requires a complete solution to the problem, including the local flux profile on the absorber. In this thesis, we focus on a well known special case, ideally suited for mathematical analysis and physical interpretation: steady advection-diffusion in a two-dimensional, irrotational flow. The velocity field is described by the flow potential, φ, as $\boldsymbol{u} = \boldsymbol{\nabla}\varphi$ and we obtain the dimensionless BVP equivalent to Eqs. (3.1)∼Eq. (3.3):

$$\mathrm{Pe}_o \boldsymbol{\nabla}\varphi \cdot \boldsymbol{\nabla}c = \boldsymbol{\nabla}^2 c, \quad \boldsymbol{\nabla}^2\varphi = 0, \quad (x, y) \in \Omega_z \tag{5.3}$$

$$c = 1, \quad \hat{\boldsymbol{n}} \cdot \boldsymbol{\nabla}\varphi = 0, \quad (x, y) \in \partial\Omega_z \quad \text{and} \quad c \to 0, \quad x^2 + y^2 \to \infty; \tag{5.4}$$

$$\boldsymbol{\nabla}\varphi \to \hat{\boldsymbol{x}}, \quad x^2 + y^2 \to \infty, \tag{5.5}$$

where Ω_z is the flow region, exterior to the finite absorber as shown in Fig. 5-1. Note that, in Eq. (5.4), we use boundary conditions for desorption ($c = 1$ on $\partial\Omega_z$ and $c = 0$ far away), which are somewhat more convenient that those of adsorption ($c = 0$ on $\partial\Omega_z$ and $c = 1$ far away) used in Eqs. (3.1)∼Eq. (3.3). If c is a solution for one problem, $1 - c$ is one for the other by linearity.

The key to analyzing Eq. (5.3) is to view points in the plane as complex numbers, $z = x + iy$. For example, this enables a transformation to streamline coordinates, $\Psi = \varphi + i\psi$,

which reduces the problem to a thin absorbing strip in a uniform flow [73]. For a more general perspective in terms of conformal mapping, see Bazant [62]. Using complex-variable techniques, the general system of PDEs Eq. (5.3) has been studied recently with applications to tracer dispersion [74] and heat transfer [75] in porous media, as well as vorticity diffusion in strained wakes [76, 77].

Complex analysis becomes particularly useful when the interface, $\partial\Omega_z(t)$, is a moving free boundary, driven by the local flux density, σ_z. For a broad class of transport-limited growth phenomena, the interfacial dynamics, whether deterministic or stochastic, can be formulated in terms of a time-dependent conformal map from a simple, static domain to the evolving, physical domain (see Chap. 2). For continuous growth by advection-diffusion, this approach was introduced by van Wijngaarden [78] and Maksimov [79], who solved Eqs. (5.3)~(5.5) in streamline coordinates. Maksimov's method has been used extensively by Kornev and his collaborators to describe solidification and freezing from a flowing melt [80, 81, 64, 82, 83, 84, 60]. These studies significantly extend the conformal-map dynamics for Laplacian growth by pure diffusion, without advection [23, 24, 85].

5.2 Mathematical Preliminaries

5.2.1 Streamline Coordinates

In his analysis of high Reynolds number flows, Boussinesq [73] discovered a hodograph transformation (exchanging dependent and independent variables) which greatly simplifies Eq. (5.3). It is well known that the velocity potential is the real part of an analytic complex potential, $\Psi = \varphi + i\psi$, where the harmonic conjugate, ψ, is the stream function [86]. Using the Cauchy-Riemann equations, it is easy to show that the concentration profile, c, satisfies the simplified PDE

$$\mathrm{Pe}_o \frac{\partial c}{\partial \varphi} = \frac{\partial^2 c}{\partial \varphi^2} + \frac{\partial^2 c}{\partial \psi^2}, \tag{5.6}$$

in "streamline coordinates", (φ, ψ). The physical significance of this equation is that advection (the left hand side) only occurs along streamlines, while diffusion (the right hand side) also occurs in the transverse direction, along isopotential lines.

Boussinesq's transformation corresponds to a conformal mapping to a plane of a uniform flow, described by a constant $\boldsymbol{\nabla}\varphi$. Therefore, an arbitrary domain, Ω_z, as shown in Fig. 5-1,

is mapped to the exterior of a straight line segment, or strip, parallel to the streamlines (which is a branch cut of the inverse map). Some examples are given in Fig. 5-2. In streamline coordinates, the BCs Eqs. (5.4) and (5.5) are transformed as follows:

$$c = 1, \quad \psi = 0, \; -2A < \varphi < 2A, \quad \text{and} \quad c \to 0 \quad \text{as} \quad \varphi^2 + \psi^2 \to \infty. \tag{5.7}$$

The constant A is determined so that $4A$ is equal to the difference of the flow potential φ between two stagnant points, for example, the points S_u and S_d shown in Fig. 5-1.

5.2.2 Formulation as an Integral Equation

In streamline coordinates, the advection-diffusion process past a finite strip can be formulated in terms of an integral equation using the classical method of Green's functions [87]. For reasons to become clear in Sec. 5.2.3, we let $x = \varphi$, $y = \psi$, $A = 1/2$, and $\text{Pe} = \text{Pe}_o/2$, so the BVP Eqs. (5.6)$\sim$(5.7) takes the form

$$2\,\text{Pe}\frac{\partial c}{\partial x} = \frac{\partial^2 c}{\partial x^2} + \frac{\partial^2 c}{\partial y^2}, \tag{5.8}$$

$$c = 1, \quad \text{on} \quad y = 0, \; -1 < x < 1 \quad \text{and} \quad c = 0, \quad \text{as} \quad x^2 + y^2 \to \infty. \tag{5.9}$$

Green's function $G(x, y)$ for Eqs. (5.8) and (5.9), which expresses the concentration profile generated by a unit source flux at the origin, satisfies the PDE

$$2\,\text{Pe}\frac{\partial G}{\partial x} - \frac{\partial^2 G}{\partial x^2} - \frac{\partial^2 G}{\partial y^2} = \delta(x)\delta(y).$$

After removing the first derivative term by a change of variables and using polar coordinates,

$$G(x, y) = e^{\text{Pe}\,x} F(r, \theta) \, , \tag{5.10}$$

we find that F obeys the Helmholtz equation

$$\boldsymbol{\nabla}^2 F - \text{Pe}^2 F = \delta(x)\delta(y) \, , \tag{5.11}$$
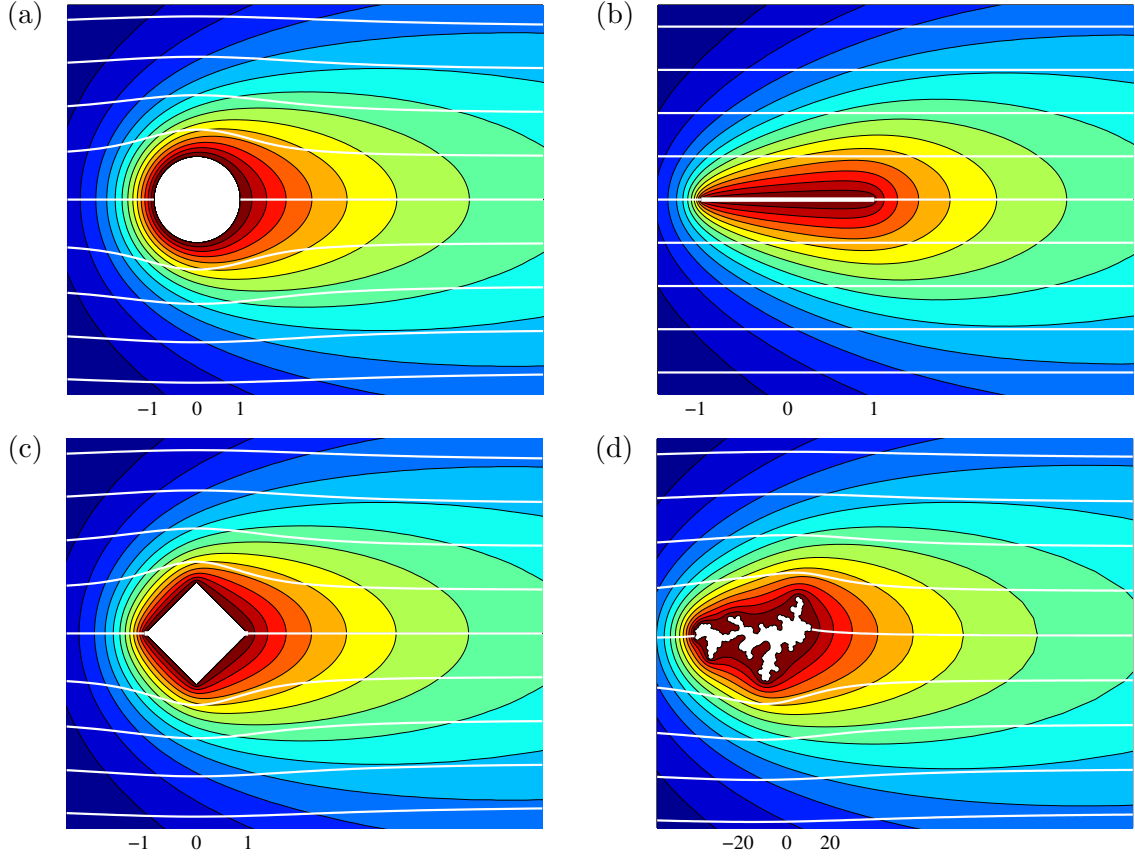
Figure 5-2: Numerical solutions using the method of Sec. 5.3 for the concentration profile (color contour plot) and streamlines (open yellow curves) around different absorbing objects in a uniform background potential flow: (a) the unit disk, (b) a finite strip, (c) a square, and (d) an ADLA fractal cluster of 3000 particles with $Pe_o = 1$, 2, 1.2 and 0.05 respectively. The geometries in (b), (c) and (d) are obtained by conformal mapping from (a). Case (b) corresponds to streamline coordinates; case (c) is obtained by the numerical Schwarz-Christoffel mapping; case (d) is obtained from a stochastic, iterated conformal map. The horizontal axis is labeled by numerical values of the spatial coordinate x. However, the distances in the figures (a)-(d) are scaled by the "conformal radius" A_1, see Eq. (2.4) below, which is the characteristic size of the physical object. The A_1 is chosen so that the renormalized Péclet number is the same, $Pe = A_1 Pe_o = 1$, in all cases, which explains why the far-field solutions look the same.

whose solution is a modified Bessel function of the second kind, $K_0(\text{Pe}\,r)$, where $r = (x^2 + y^2)^{1/2}$. Taking into account the unit normalization, we obtain Green's function,

$$G(x, y) = e^{\text{Pe}\,x} K_0(\text{Pe}\,r)/2\pi. \tag{5.12}$$

The concentration profile, c, everywhere in streamline coordinates is obtained by convolving Green's function, G, with the flux on the strip,

$$c(x, y) = \int_{-1}^{1} G(x - x', y) \cdot 2\sigma(x')dx', \tag{5.13}$$

where the factor 2 is included because the flux has the same value,

$$\sigma(x) = -\frac{\partial c}{\partial y}(x, 0^+) = \frac{\partial c}{\partial y}(x, 0^-),$$

on the upper and the lower sides of the strip, respectively. Therefore, the boundary value problem described by Eqs. (5.8) and (5.9) is equivalent to finding the $\sigma(x)$ that satisfies the integral equation [78, 88]

$$\int_{-1}^{1} e^{\text{Pe}(x-x')} K_0\left(\text{Pe}|x - x'|\right) \sigma(x')dx' = \pi, \quad -1 < x < 1, \tag{5.14}$$

which forms the basis for the theory of solidification in flowing melts [79]. In this context, Eq. (5.14) has been analyzed for large and small Pe by Kornev and collaborators, as cited in the introduction. Below, we will extend these results and construct an analytical approximation that is uniformly accurate in both Pe and x.

Eq. (5.14) is a Fredholm-type equation of the first kind (with a difference kernel) whose the existence and uniqueness of solutions are not guaranteed. In the present case, however, the symmetrized kernel, $K_0(\text{Pe}\,|x - x'|)$, is positive definite, and thus invertible. Using the representation,

$$K_0(x) = \frac{1}{2} \int_{-\infty}^{\infty} dt\, \frac{\cos(xt)}{\sqrt{1 + t^2}}, \tag{5.15}$$

the kernel is recast to the form

$$\int_{-\infty}^{\infty} dt\, \frac{\cos(\varsigma t)\cos(\varsigma_0 t) + \sin(\varsigma t)\sin(\varsigma_0 t)}{\sqrt{1 + t^2}}. \tag{5.16}$$

Then, for $\beta > 0$,

$$\int_{-\beta}^{\beta} d\varsigma_0 \int_{-\beta}^{\beta} d\varsigma \int_{-\infty}^{\infty} dt \, \frac{\cos(\varsigma t)\cos(\varsigma_0 t) + \sin(\varsigma t)\sin(\varsigma_0 t)}{\sqrt{1+t^2}} f(\varsigma_0) f(\varsigma) = \int_{-\infty}^{\infty} dt \, \frac{g(t)^2 + h(t)^2}{\sqrt{1+t^2}},$$
(5.17)

where real functions $g(t)$ and $h(t)$ are given by

$$g(t) + ih(t) = \int_{-\beta}^{\beta} f(u) e^{iut} du.$$
(5.18)

It seems tempting to approach Eq. (5.14) using Fourier-type methods because it involves a convolution [89], but the kernel is not a periodic function. We also note that the kernel is singular and not of the classical Cauchy type [90]. It is known that Eq. (5.14) admits a solution which can be expanded in terms of Mathieu functions [91, 92], but such representations are impractical for computations over a wide range of Pe, and give no insight into the dependence of the flux σ on x and Pe. The collocation method has been used successfully to obtain numerically the solution of Eq. (5.14) [64].

5.2.3 The General Principle of Conformal Invariance

There is a simple way to understand why Boussinesq's transformation works: The advection-diffusion PDE Eq. (5.3) is invariant under conformal changes of variables, even though its solutions are not harmonic functions, which also holds more generally for some other equations [62]. As such, the boundary value can be transformed to any convenient geometry by conformal mapping. Streamline coordinates is a good choice for asymptotics, but other choices are better suited for numerical analysis and similarity solutions.

Here, we exploit this general principle to map the BVP Eqs. (5.3)$\sim$(5.5) to other useful coordinate systems. If $\varphi_w = \mathrm{Re}\,\Psi(w)$ and $c_w = F(w, \overline{w})$ (where $\overline{w}$ denotes the complex conjugate of w) solve Eq. (5.3) in some simple domain, Ω_w, then $\varphi_z = \mathrm{Re}\,\Psi(f(z))$ and $c_z = F(f(z), \overline{f(z)})$ solve Eq. (5.3) in an arbitrary mapped domain, $\Omega_z = g(\Omega_z)$, where $z = g(w) = f^{-1}(w)$. The concentration BCs Eq. (5.4) are conformally invariant, but, since the BC Eq. (5.5) prescribing the background flow is not, due to the gradient, care must be taken in transforming the solution.

For ADLA in Chap. 3, it was natural to let Ω_w be the exterior of the unit disk, so our canonical problem is that of a concentrated flow past a circular absorber, shown in

Fig. 5-2(a). We repeat the BVP in Ω_w, Eqs. (3.6)∼(3.7) here:

$$\text{Pe } \boldsymbol{\nabla}\varphi \cdot \boldsymbol{\nabla}c = \boldsymbol{\nabla}^2 c, \quad \varphi = \text{Re}\left\{w + \frac{1}{w}\right\}, \qquad |w| > 1 \tag{5.19}$$

$$c = 0, \qquad |w| = 1 \quad \text{and} \quad c \to 1, \qquad |w| \to \infty. \tag{5.20}$$

In order to preserve the unit flow speed far away in Ω_w, we use the *rescaled* Péclet number $\text{Pe} = A_1 \text{Pe}_o$ instead of Pe_o. The physical significance of Pe is that it determines the far-field solution, independent of the absorber's shape and the bare Péclet number. This point is illustrated in Fig. 5-2, where the concentration and flow field far away from various objects at $\text{Pe} = 1$ looks the same, in spite of extremely different shapes, ranging from a circle to a fractal ADLA cluster. Therefore, we view Pe as the basic parameter in our analysis, from which we define the bare Péclet number, $\text{Pe}_o = \text{Pe}/A_1$, for arbitrary domains, in terms of the univalent map from the exterior of the unit circle.

From this perspective, streamline coordinates are obtained via the Joukowski transformation [65], $g(w) = (w + 1/w)/2$, which maps the unit circular disk onto the finite strip of length 2 centered at the origin along the real axis. The BVP Eqs. (5.19)∼(5.20) is then transformed to the form Eqs. (5.8)∼(5.9) given above. In general, the fluxes on the boundaries $\partial\Omega_z$ (the absorber surface) and $\partial\Omega_w$ (the unit circle, $w = e^{i\theta}$) are related by

$$\sigma_w(\theta; \text{Pe}) = |g\prime(w)| \, \sigma_z(g(w); \text{Pe}), \tag{5.21}$$

where σ_w is the flux on $\partial\Omega_w$ and σ_z is the flux on $\partial\Omega_z$. In the case of streamline coordinates Eqs. (5.8)∼(5.9), the flux on the strip, $\sigma_z(x; \text{Pe})$, is thus related to the flux on the circle, $\sigma_w(\theta; \text{Pe})$, by

$$\sigma_w(\theta; \text{Pe}) = |\sin\theta| \, \sigma_z(\cos\theta; \text{Pe}). \tag{5.22}$$

For a bounded flux on the circle, σ_w, the flux on the strip, σ_z, always diverges as $O[(1 - x^2)^{-1/2}]$ as x approaches ± 1. Therefore, although we will use the strip geometry, Ω_z, for asymptotic analysis in Secs. 5.4 and 5.5, the circle geometry, Ω_w, is a better starting point for our numerical analysis in Sec. 5.3. In all cases, however, our goal is to obtain the flux on the circle, the canonical geometry for a finite absorber.

5.2.4 Similarity Solutions for Semi-Infinite Leading Edges

Before proceeding with our analysis, we mention a class of similarity solutions for "leading edges" which have relevance for the high-Pe limit of our problem. For this section only, we use the upper half plane, $\{\mathrm{Im}\, w > 0\}$, as our simple domain, Ω_w. For a straining velocity field, $\varphi(w) = \mathrm{Re}\, w^2$, bringing fluid toward the plane, there is a classical similarity solution for the concentration profile, $c(w, \overline{w}) = \mathrm{erfc}(\sqrt{\mathrm{Pe}_o}\, \mathrm{Im}\, w)$, for which the flux on the real axis is a constant, $\sigma_w = 2\sqrt{\mathrm{Pe}_o/\pi}$.

For every conformal map, $w = f(z)$, from the z plane to the upper half w plane, there corresponds another similarity solution [60, 62],

$$\varphi = \mathrm{Re}\, f(z)^2 \quad \text{and} \quad c = \mathrm{erfc}(\sqrt{\mathrm{Pe}_o}\, \mathrm{Im}\, f(z)) \quad \text{for} \quad \mathrm{Im}\, w \geq 0. \tag{5.23}$$

Note that the boundary condition $\boldsymbol{\nabla}\varphi \sim \hat{\boldsymbol{x}}$ as $|z| \to \infty$ holds only if $f(z) \sim \sqrt{z}$ as $|z| \to \infty$, so these solutions correspond to more general flows near stagnation points. For the purposes of this thesis, we discuss two choices for $f(z)$:

1. $f(z) = \sqrt{z}$, which maps the entire z plane, with the exception of the branch cut $\{\mathrm{Im}\, z = 0, \mathrm{Re}\, z > 0\}$, onto Ω_w. The (x, y) coordinates of the z plane then correspond to the streamline coordinates, and the flux on the strip is $\sigma(x) = \sqrt{\mathrm{Pe}_o/\pi x}$. This well known formula can also be derived via replacing the upper limit of integration in Eq. (5.14) by ∞, and applying the Wiener-Hopf method of factorization [65, 78, 93]. This procedure is carried out systematically to all orders of approximation in Sec. 5.4 and via a different, rigorous method by Margetis and Choi [94].

2. $f(z) = \sqrt{z} + 1/\sqrt{z}$, which maps the exterior of the circular rim, $\{z : |z| > 1 \quad \text{and} \quad 0 < \arg z < 2\pi\}$, onto Ω_w [62]. This solution describes the advection-dominated (high-Pe) fixed point of the ADLA fractal-growth process. From Eq. (5.23) with $z = re^{i\theta}$ and $r \geq 1$, we find

$$c(r, \theta) = \mathrm{erfc}\left[\sqrt{\mathrm{Pe}_o}\left(\sqrt{r} + \frac{1}{\sqrt{r}}\right)\sin\left(\frac{\theta}{2}\right)\right], \quad \sigma(\theta) = 2\sqrt{\frac{\mathrm{Pe}_o}{\pi}}\sin\left(\frac{\theta}{2}\right), \tag{5.24}$$

which is the leading-order solution for our BVP Eqs. (5.19)~(5.20) as $\mathrm{Pe}_o = \mathrm{Pe} \to \infty$.

The fact that we consider *finite* absorbers leads to significant analytical and numerical

complications, which are our focus.

5.3 Numerical Solution

5.3.1 Conformal Mapping to Polar Coordinates Inside the Unit Disk

In this section we determine the concentration profile c by numerically solving the BVP Eqs. (5.19)$\sim$(5.20). One of the difficulties in applying a numerical method is related to the fact that the region Ω_w is unbounded. By invoking conformal invariance again, however, we can apply a transformation that leaves the BVP unchanged yet maps Ω_w to a bounded region. In particular, we use inversion, $g(w) = 1/w$, to map the disk exterior onto its interior. Physically, this corresponds to a dipole source of concentrated fluid inside an absorbing circular cylinder, as shown in Fig. 5-3(a). With $g(w) = re^{i\theta}$ the problem is expressed in the polar coordinates (r, θ) by

$$r^3 \frac{\partial^2 c}{\partial r^2} + \{r^2 + \text{Pe}\, r(1 - r^2)\cos\theta\}\frac{\partial c}{\partial r} + r\frac{\partial^2 c}{\partial \theta^2} + \text{Pe}(1 + r^2)\sin\theta\frac{\partial c}{\partial \theta} = 0,$$

$$c = 0, \quad \text{at} \quad r = 0, \quad \text{and} \quad c = 1, \quad \text{at} \quad r = 1,$$

(5.25)

where $r \leq 1$ and $0 \leq \theta < 2\pi$. A solution in the (r, θ) plane is shown in Fig. 5-3(b).

5.3.2 Analytical Treatment of Singularities

Before we apply any numerical method to Eq. (5.25) directly, we note that the concentration profile c as a function of (r, θ) exhibits singular behavior as r approaches 0. We first need to modify Eq. (5.25) in order to eliminate this behavior, which undermines the accuracy of our numerical method. From the similarity solution Eq. (5.24) and Green's function of Sec. 5.2.2 we obtain the leading-order behavior

$$c(r, \theta) = O\left\{ \sqrt{r} \, \exp\left[\text{Pe}\left(2 - \frac{1}{r} - r \right) \sin^2\left(\frac{\theta}{2} \right) \right] \right\} \quad \text{as} \quad r \to 0.$$

(5.26)

First, the square-root limit $c(r, \theta = 0) = O(\sqrt{r})$ can hardly be dealt with in numerical methods because of the resulting diverging derivative near $r = 0$. Second, the essential singularity at $r = 0$, $c(r, \theta = \pi) = O\left(\sqrt{r}\, e^{-\text{Pe}/r} \right)$, forces c to change drastically near $r = 0$. Especially when Pe is large, this limiting behavior is extended even to $r < 1 - O(1/\sqrt{Pe})$. To avoid this behavior, we define a function $h(r, \theta)$ by factoring out the leading-order singular
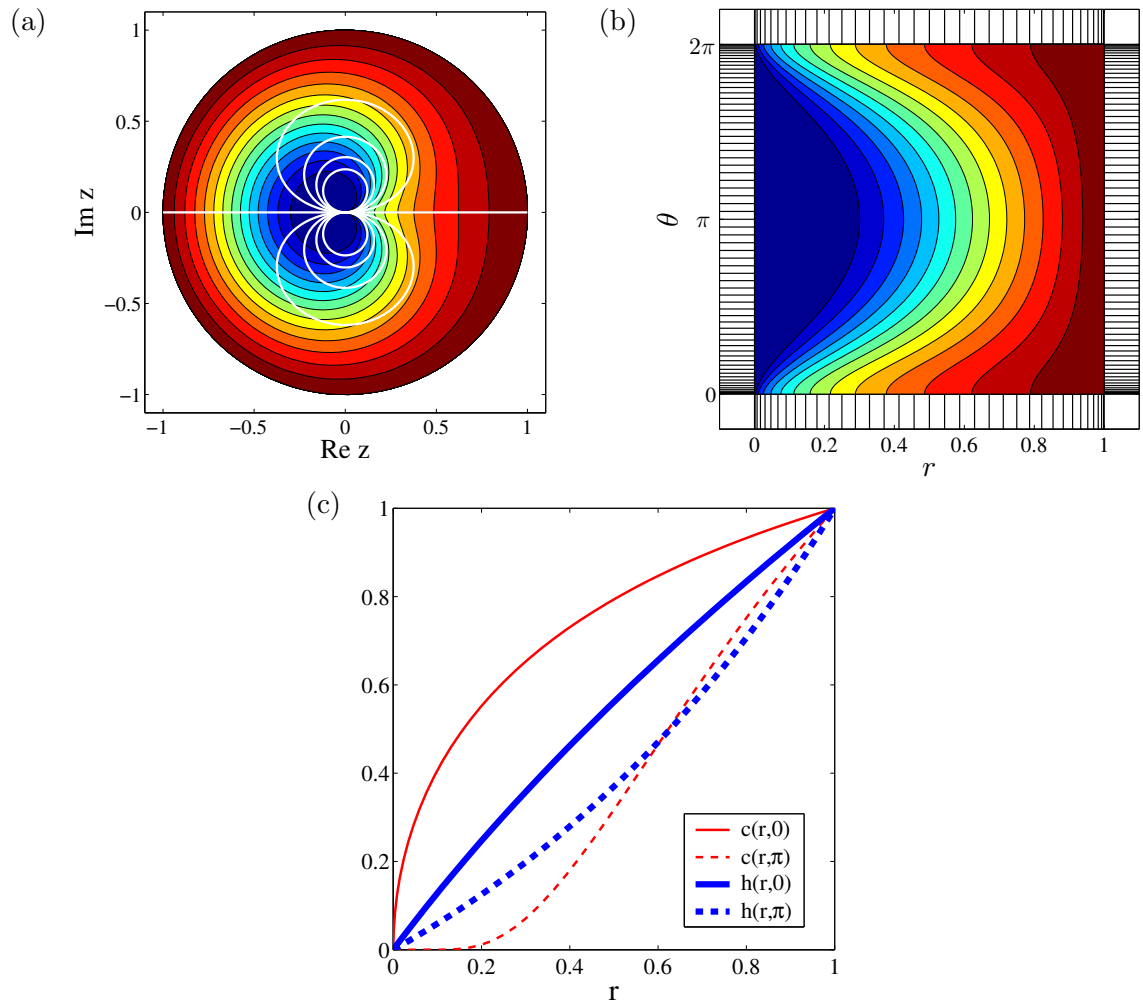
Figure 5-3: The concentration profile (Pe = 1) calculated numerically in the interior of the circular disk is shown (a) in Cartesian coordinates, and (b) in polar coordinates. In (c) the numerically obtained values are shown for $c(r, \theta = 0)$ (thin solid line), $c(r, \theta = \pi)$ (thin dashed line), $h(r, \theta = 0)$ (thick solid line), and $h(r, \theta = \pi)$ (thick dashed line).

behavior of $c(r, \theta)$ as

$$\sqrt{r} \, \exp\left\{\text{Pe}\left(2 - \frac{1}{r} - r\right)\sin^2\left(\frac{\theta}{2}\right)\right\} h(r, \theta) \equiv r \, c(r, \theta), \tag{5.27}$$

and apply the numerical method shown below directly to this $h(r, \theta)$. Note that the c is multiplied by r in the right-hand side of Eq. (5.27) to ensure that $h(r, \theta) = O(r)$ as $r \to 0$; thus, $h = 0$ at $r = 0$, which is the same condition as for c. Combining Eqs. (5.25) and (5.27) we obtain a PDE for $h(r, \theta)$:

$$r^3 \frac{\partial^2 h}{\partial r^2} + \text{Pe}(r - r^3)\frac{\partial h}{\partial r} + r\frac{\partial^2 h}{\partial \theta^2} + 2\text{Pe}\, r \sin\theta \frac{\partial h}{\partial \theta} + \left\{\text{Pe}(r\cos\theta - 1) + \frac{r}{4}\right\} h = 0. \tag{5.28}$$

By comparison of Eqs. (5.25) and (5.28), we note that the coefficients of the derivatives are simplified in Eq. (5.28). Once h is determined from Eq. (5.28), c is simply recovered via Eq. (5.27), and $\sigma(\theta)$ is obtained as

$$\sigma(\theta) = \left.\frac{\partial c}{\partial r}\right|_{(r=1,\theta)} = \left.\frac{\partial h}{\partial r}\right|_{(r=1,\theta)} - \frac{1}{2}.$$

Fig. 5-3(c) shows how the singular behavior of c is mitigated by introducing the new variable h.

5.3.3 Spectral Method

The numerical differentiations with respect to the variables r and θ are carried out by spectral methods [95]. The spatial nodes, the points (r_j, θ_k) where the function is evaluated numerically, are determined by

$$r_j = \frac{1}{2}\left(1 - \cos\frac{j\pi}{N_r}\right) \quad \text{and} \quad \theta_k = \pi\left(1 - \cos\frac{k\pi}{N_\theta}\right),$$

where $j = 1, \ldots, N_r$ and $k = 0, \ldots, N_\theta$; the nodes have higher density at the endpoints as shown in the frame of Fig. 5-3(b). Once the function values are given at the nodes, the derivatives at these points are calculated by interpolation via Chebyshev's polynomials. This procedure is very efficient, as the error in the spectral method is known to decrease exponentially in the number of nodes [95]. We used $N_r = 50$ and $N_\theta = 100$ (practically $N_\theta = 50$ exploiting the symmetry in θ) for all the numerical results appearing in this thesis.

Fig. 5-4 shows the concentration profile, $c(r,\theta)$, for Pe of different orders of magnitude. As Pe increases, there is an apparent crossover from a diffusion-dominated regime (a), where the concentration disturbance looks like a "cloud" extending in all directions, and an advection-dominated regime (c), where concentration gradients are confined to a narrow boundary layer which separates into a thin wake downstream. Understanding the crossover regime (b) to (c) is an important part of this chapter, revisited below in Sec. 5.7, following our analysis of the flux profile.

Fig. 5-5 shows the flux density on the absorber, $\sigma(\theta)$, for different values of Pe. To check the validity of our numerical method, we compare the result for σ with the asymptotic expansion for high Pe from Sec. 5.4 below, which can be numerically evaluated to any order. For this comparison we used the intermediate range of Péclet numbers $10^{-2} < \text{Pe} < 10^2$ for which the series converge fast enough yet the numerical method is stable. When $N_r = 50$ and $N_\theta = 100$ nodes are used for the discretization, the relative error measured as $||\sigma_{\text{num}} - \sigma_{\text{asym}}|| \ / \ ||\sigma_{\text{asym}}||$ is of the order of 10^{-5} or smaller; here, σ_{num} and σ_{asym} denote the numerical and the asymptotic solutions, respectively and the norm is defined as $||\sigma|| = \max\{\theta \in [0, 2\pi) : |\sigma(\theta)|\}$.

If Pe lies outside the given intermediate range, care should be exercised in using our numerical method as explained in the next subsection. For such cases, however, the asymptotic, analytical formulae of Secs. 5.4 and 5.5 give sufficently accurate solutions. The reader is referred to Secs. 5.4 and 5.5 for details on the formulae and the comparisons with the numerical solution.

5.3.4   Adaptive Mesh for Very High Péclet Numbers

A feature of the solution c that may undermine the accuracy of our numerics is the emergence of boundary layers for sufficiently large Pe. By virtue of Eq. (5.49) below we expect that for Pe $\gg 1$,

$$\frac{\partial c}{\partial r}\bigg|_{(r=1,\theta)} = \sigma(\theta) = \begin{cases} 2\sqrt{\text{Pe}/\pi}\ \sin(\theta/2) & \text{when}\quad \theta \gg O\big(1/\sqrt{\text{Pe}}\big) \\ \\ 1/\pi & \text{when}\quad \theta \leq O\big(1/\sqrt{\text{Pe}}\big). \end{cases} \tag{5.29}$$

So, $c(r,\theta)$ has boundary layers near $r = 1$ and $\theta = 0, 2\pi$ whose widths are $O(1/\sqrt{\text{Pe}})$, as indicated in Fig. 5-6(a). The layer at $\theta = 0$ corresponds to the "tail" shown in Fig. 5-4(c).
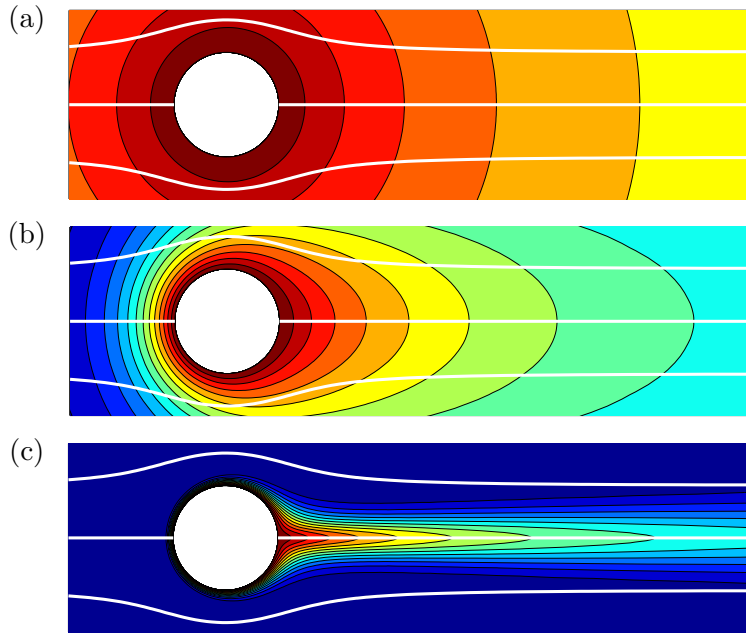
Figure 5-4: The concentration profiles for adsorption (or desorption) around the unit circular disk for (a) Pe = 0.01, (b) Pe = 1, and (c) Pe = 100.
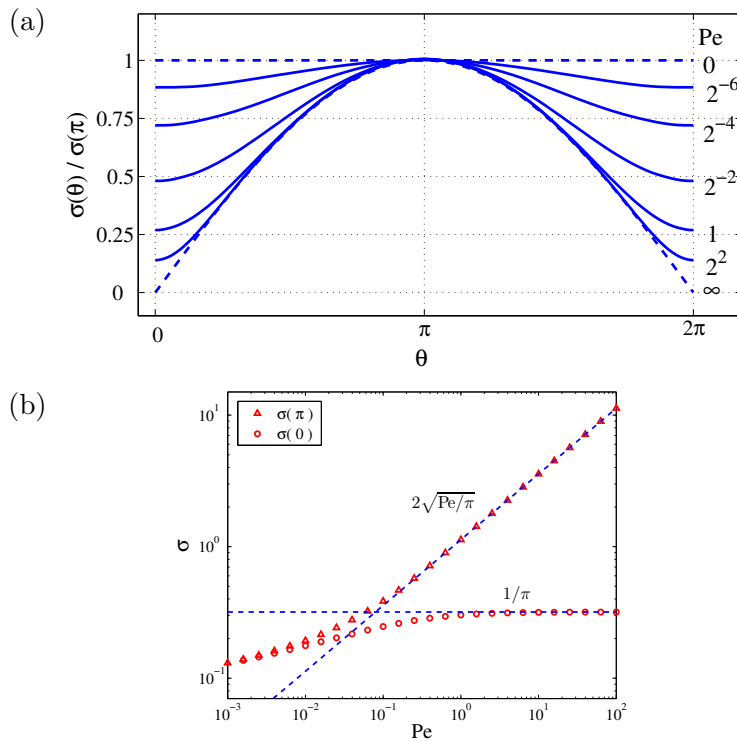
Figure 5-5: The flux $\sigma(\theta)$ is plotted around the unit disk for different values of Pe: (a) $\sigma(\theta)/\sigma(\pi)$ for Pe $= 0, 2^{-6}, 2^{-4}, 2^{-2}, 1, 2^2, \infty$, and (b) the values $\sigma(\theta = \pi)$ and $\sigma(\theta = 0)$ for a range of Pe.

75

Thus, the numerical method starts to break down when the node spacing becomes of the order of $1/\sqrt{\text{Pe}}$.

We next outline a technique to deal with the case of very high Pe within our numerical procedure. The idea is to introduce a set of independent variables, $\tilde{r} = \tilde{r}(r)$ and $\tilde{\theta} = \tilde{\theta}(\theta)$, so that c is a sufficiently smooth function of $\tilde{r}$ and $\tilde{\theta}$. The following conditions are required for $\tilde{r}(r)$ and $\tilde{\theta}(\theta)$:

$$\tilde{r}(0) = 0, \; \tilde{r}(1) = 1, \; \tilde{r}'(1) = O(\sqrt{\text{Pe}}) \tag{5.30}$$

$$\tilde{\theta}(0) = 0, \; \tilde{\theta}(2\pi) = 2\pi, \; \tilde{\theta}'(0) = O(\sqrt{\text{Pe}}), \tag{5.31}$$

where the prime here denotes differentiation with respect to the argument. Once $\tilde{r}(r)$ and $\tilde{\theta}(\theta)$ are defined, we find the PDE for $\tilde{h}(\tilde{r}, \tilde{\theta}) \equiv h(r(\tilde{r}), \theta(\tilde{\theta}))$ from Eq. (5.28) by applying the chain rule for the differentiations with respect to r and θ; for example,

$$\frac{\partial h}{\partial r} = \frac{1}{r'(\tilde{r})} \frac{\partial \tilde{h}}{\partial \tilde{r}}, \quad \frac{\partial^2 h}{\partial r^2} = \frac{1}{r'(\tilde{r})^2} \frac{\partial^2 \tilde{h}}{\partial \tilde{r}^2} - \frac{r''(\tilde{r})}{r'(\tilde{r})^3} \frac{\partial \tilde{h}}{\partial \tilde{r}}. \tag{5.32}$$

We solve the resulting PDE numerically. A convenient choice for $r(\tilde{r})$ and $\theta(\tilde{\theta})$ is

$$r(\tilde{r}) = \tilde{r} + \frac{1}{\pi}\left(1 - \frac{1}{\sqrt{\text{Pe}}}\right)\sin(\pi\tilde{r}), \quad \theta(\tilde{\theta}) = \tilde{\theta} - \left(1 - \frac{1}{\sqrt{\text{Pe}}}\right)\sin\tilde{\theta}. \tag{5.33}$$

The advantage of using $\tilde{r}$ and $\tilde{\theta}$ instead of r and θ is illustrated in Fig. 5-6 for $\text{Pe} = 100$. The effects of the boundary layers in (r, θ) are notably suppressed in the formulation using $(\tilde{r}, \tilde{\theta})$. In Sec. 5.4 and 5.5 we discuss the high- and low-Pe asymptotics and their comparisons with the solution determined numerically by the method of this section.

5.4 Direct Perturbation Analysis For "High" Péclet Numbers

In this section, we derive an approximate analytical solution to the integral equation Eq. (5.14) in terms of series expansions produced via suitable iterations in the coordinate space. We also obtain closed-form expressions for the terms of the iteration series as Pe-dependent multiple integrals. We show that the series is convergent for $\text{Pe} \geq O(1)$, and that retaining only a few of its terms produces accurate results even for $\text{Pe} = O(1)$. An
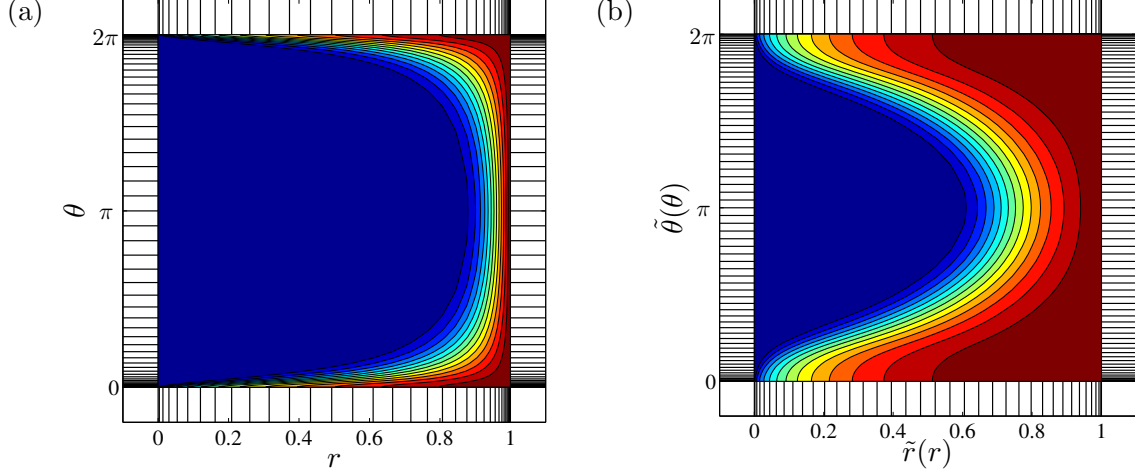
Figure 5-6: Contour plots of h for Pe $= 100$ (a) in the (r, θ) plane, and (b) in the $(\tilde{r}, \tilde{\theta})$ plane.

iterative procedure in the Fourier domain that leads to the same results is given by Margetis and Choi [94].

5.4.1 Zeroth-order solution via the Wiener-Hopf method

The starting point of the analysis is the observation that, as discussed in Sec. 5.2.4, the solution for the semi-infinite strip $-1 < x < +\infty$ (in the variable notation of Eq. (5.14) provides the leading-order term of the high-Pe asymptotic expansion of the solution for the finite strip up to a distance $O(1/\sqrt{\text{Pe}})$ from the endpoint $x = 1$. In order to develop systematically a scheme for the correction terms, we symmetrize the kernel of Eq. (5.14) and rescale the independent variable x using $s = \text{Pe}(x + 1)$ while we define $\mu(s)$ by $\sigma(x) = (\sqrt{2}/\pi)\, \text{Pe}\, e^s \mu(s)$. (The factor $(\sqrt{2}/\pi)$Pe is chosen for later convenience.) The integral equation Eq. (5.14) thus becomes

$$\int_0^{2\text{Pe}} ds' K_0\left(|s - s'|\right) \mu(s') = \frac{\pi^2 e^{-s}}{\sqrt{2}}, \quad 0 < s < 2\text{Pe}. \tag{5.34}$$

An approximate solution $\mu \sim \mu_0$ that is valid to the leading order in Pe is found by taking Pe $\to \infty$ in the upper limit of integration in Eq. (5.34). The resulting integral equation is

$$\int_0^\infty ds' K_0\left(|s - s'|\right) \mu_0(s') = \frac{\pi^2 e^{-s}}{\sqrt{2}}, \quad 0 < s. \tag{5.35}$$

The solution $\mu_0(s)$ is obtained by the Wiener-Hopf technique [93, 96]. Here we outline

the basic steps of this method, which are also applied to other, similar integral equations below. First, we extend the validity of Eq. (5.35) to $-\infty < s < \infty$ via modifying its right hand side,

$$\int_{-\infty}^{\infty} ds' K_0\left(|s - s'|\right) \mu_0(s') = \frac{\pi^2}{\sqrt{2}}\{e^{-s}u(s) + p(s)\}, \quad -\infty < s < \infty, \tag{5.36}$$

where $\mu_0(s)$ is taken to be zero for $s < 0$, $u(s)$ is the Heaviside function ($u(s) = 0$ for $s < 0$ and $u(s) = 1$ for $s > 0$), and $p(s)$ is an unknown function which has non-zero values only for $s < 0$. Next, we apply the Fourier transform in s to Eq. (5.36). Defining the Fourier transform, $\tilde{\mu}_0(k)$, of $\mu_0(s)$ as

$$\tilde{\mu}_0(k) = \int_{-\infty}^{\infty} ds\, \mu_0(s)\, e^{-iks} \quad \text{where} \quad \mu_0(s) = \int_{-\infty}^{\infty} \frac{dk}{2\pi}\, e^{iks}\, \tilde{\mu}_0(k), \tag{5.37}$$

Eq. (5.36) yields

$$\frac{\pi\tilde{\mu}_0(k)}{\sqrt{1 + k^2}} = \frac{\pi^2}{\sqrt{2}}\left[\frac{1}{1 + ik} + \tilde{p}(k)\right]. \tag{5.38}$$

By simple algebraic manipulations the last equation becomes

$$\frac{\tilde{\mu}_0(k)}{\sqrt{1 + ik}} - \frac{\pi}{1 + ik} = \frac{\pi}{\sqrt{2}}\left[\frac{\sqrt{1 - ik} - \sqrt{2}}{1 + ik} + \sqrt{1 - ik}\,\tilde{p}(k)\right], \tag{5.39}$$

where the left hand side defines a function analytic in the lower half k plane, $\operatorname{Im} k < \varepsilon$ for a small positive ε, and the right hand side defines a function analytic in the upper half k plane, $\operatorname{Im} k > -\varepsilon$; each of these functions vanishes as $|k| \to \infty$ in the corresponding half plane. Thus, the two sides of Eq. (5.39) together define an entire function of k, which is identically zero by Liouville's theorem [65]. It follows that in the region of overlap, $|\operatorname{Im} k| < \varepsilon$, the solution is $\tilde{\mu}_0(k) = \pi(1 + ik)^{-1/2}$. Inversion of this formula yields

$$\mu_0(s) = \sqrt{\frac{\pi}{s}}e^{-s}, \quad 0 < s < \infty. \tag{5.40}$$

5.4.2   Leading-order Uniformly Accurate Approximation

The deviation of $\mu_0(s)$ in Eq. (5.40) from the actual solution $\mu(s)$ of the finite strip is interpreted as due to the effect of a fictitious, "misplaced" flux source lying in 2Pe $< s$, which is present in Eq. (5.35). Therefore a correction term must be found for $\mu_0(s)$ by

placing a "correction source" on the original strip, $0 < s < 2\text{Pe}$, to compensate for the effect of the misplaced source. Margetis and Choi [94] further develop this approach and place it on a firm mathematical ground using Fourier transforms and a generalization of the Wiener-Hopf method. We proceed to calculate the correction to μ_0 iteratively. Accordingly, the solution $\mu(s)$ is sought in terms of the series

$$\mu = \mu_0 + \mu_1 + \mu_2 + \mu_3 + \ldots + \mu_n + \ldots, \tag{5.41}$$

where each term, $\mu_n(s)$, corresponds to suitable source corrections as described below.

We consider a half-line as the domain of the correction $\mu_1(s)$, as we did to obtain μ_0, but in the region $-\infty < s < 2\text{Pe}$ instead of the region $0 < s < \infty$. The term μ_1 is determined so that its effect compensates for the integrated effect of $\mu_0(s)$ in the region $2\text{Pe} < s$. Hence, the correction $\mu_1(s)$ satisfies

$$\int_{-\infty}^{2\text{Pe}} ds' K_0(|s - s'|)\mu_1(s') = \int_{2\text{Pe}}^{\infty} ds' K_0(|s - s'|)\mu_0(s'), \quad s < 2\text{Pe}, \tag{5.42}$$

where the right-hand side is known. The next-order corrections can be formulated and interpreted in a similar way; the correction μ_n compensates for the effect of the misplaced source corresponding to μ_{n-1}, where μ_{n-1} and μ_n are defined in half-lines that together cover the entire real axis and overlap only in the region of the finite strip. In general, $\mu_{n\geq 1}$ satisfy the recursion relations

$$\int_{0}^{\infty} K_0(|s - s'|)\mu_{n=2k}(s')ds' = \int_{-\infty}^{0} K_0(|s - s'|)\mu_{n-1}(s')ds',$$
$$\int_{0}^{\infty} K_0(|v - v'|)\mu_{n=2k+1}(2\text{Pe} - v')dv' = \int_{-\infty}^{0} K_0(|v - v'|)\mu_{n-1}(2\text{Pe} - v')dv', \tag{5.43}$$

where we made the change of variable from s to $v = 2\text{Pe} - s$ so that the integral equation for $\mu_{n=2k+1}$ has the same form as the one for $\mu_{n=2k}$. The variables s and v are both positive ($s > 0$ and $v > 0$), the left endpoint ($x = -1$) of the strip corresponds to $s = 0$ and the right endpoint ($x = 1$) corresponds to $v = 0$.

The various μ_n can be obtained successively, order by order, by applying the Wiener-Hopf method [93, 96] directly to Eq. (5.43), but the procedure becomes increasingly cumbersome with n. Instead, we propose a systematic procedure that facilitates the derivation of a closed-form expression for each μ_n. For this purpose, we introduce an operator, $\mathcal{L}$,

that relates μ_{n-1} and μ_n by $\mathcal{L}[\mu_{n-1}] \equiv \mu_n$. By Eq. (5.43) $\mathcal{L}$ is linear. In order to obtain μ_1, we notice that the leading-order solution $\mu_0(s)$ can be represented as an integral over a variable, t_0,

$$\mu_0 = \sqrt{\frac{\pi}{s}} e^{-s} = \int_{-\infty}^{\infty} dt_0 \; e^{-s(1+t_0^2)}. \tag{5.44}$$

Then $\mathcal{L}$ acts on μ_0 to yield μ_1 as [1]

$$\mu_1 = \int dt_0 \; \mathcal{L}[e^{-s(1+t_0^2)}], \tag{5.45}$$

where the order of $\mathcal{L}$ and integration is safely interchanged. The advantage of using the t_0-representation is that $e^{-s(1+t_0^2)}$, as a function of s, has a Fourier transform simpler than the Fourier transform of $\mu_0(s)$ itself. The function $\mathcal{L}[e^{-s(1+t_0^2)}]$ is found by the Wiener-Hopf method [93] as described in Sec. 5.4.1, and μ_1 follows by Eq. (5.45):

$$\mathcal{L}[e^{-s(1+t_0^2)}] = \frac{e^{-2\mathrm{Pe}(1+t_0^2)}}{\pi\sqrt{2+t_0^2}} \left[\sqrt{\frac{\pi}{v}} \; e^{-v} - \pi\sqrt{2+t_0^2} \; e^{v(1+t_0^2)} \mathrm{erfc}\sqrt{v(2+t_0^2)} \right], \tag{5.46}$$

$$\mu_1(v) = K_0(2\mathrm{Pe}) \frac{e^{-v}}{\sqrt{\pi v}} - \int dt_0 \; e^{-(2\mathrm{Pe}-v)(1+t_0^2)} \mathrm{erfc}\sqrt{v(2+t_0^2)}. \tag{5.47}$$

Because μ_0 and μ_1 are accurate arbitrarily close to the left edge ($s = 0$) and the right edge ($v = 0$) of the strip, respectively, $\mu_0 + \mu_1$ yields a leading-order approximation for μ as $\mathrm{Pe} \to \infty$ valid over the entire finite strip. The corresponding approximation for the flux $\sigma = (\sqrt{2}/\pi)\mathrm{Pe}\,e^s \mu(s)$ is $\sigma \sim \sigma_1 + \sigma_2$, which is given by

$$\sigma(x) \sim \sigma^{(\mathrm{hi})}(x) = 2\sqrt{\frac{\mathrm{Pe}}{\pi}} \left\{ \frac{1}{\sqrt{2(1+x)}} + \frac{K_0(2\mathrm{Pe})e^{2\mathrm{Pe}x}}{\pi\sqrt{2(1-x)}} \right.$$
$$\left. - \int d\tau \; \frac{e^{-(1+x)\tau^2}}{\sqrt{2\pi}} \mathrm{erfc}\sqrt{(2\mathrm{Pe}+\tau^2)(1-x)} \right\} \tag{5.48}$$

for the geometry of the finite strip, and

$$\sigma(\theta) \sim \sigma^{(\mathrm{hi})}(\theta) = 2\sqrt{\frac{\mathrm{Pe}}{\pi}} \left\{ |\sin\frac{\theta}{2}| + \frac{1}{\pi} K_0(2\mathrm{Pe})e^{2\mathrm{Pe}\cos\theta} |\cos\frac{\theta}{2}| \right.$$
$$\left. - \frac{|\sin\theta|}{\sqrt{2\pi}} \int d\tau \; e^{-(1+\cos\theta)\tau^2} \mathrm{erfc}\sqrt{(2\mathrm{Pe}+\tau^2)(1-\cos\theta)} \right\} \tag{5.49}$$

---

[1] In the remaining integrals of this section the range of integration is understood to be from $-\infty$ to ∞ unless it is stated otherwise.

for the geometry of the unit circular disk. In the last formula we changed the variable to $\tau = \sqrt{\text{Pe}}\, t_0$. An expansion similar to Eq. (5.48) has been obtained by Chugunov and Kornev [80] and Kornev and Chugunov [81] in the physical context of artificial freezing [2]; these authors did not use the operator $\mathcal{L}$ in their method and apparently did not obtain higher-order terms. An elaborate mathematical procedure for asymptotic solutions to the relevant class of integral equations on the basis of kernel approximations is described in Aleksandrov and Belokon [97] and Aleksandrov and Pozharskii [98]. We note that $\sigma_0(x)$ and $\sigma_1(x)$ are singular at $x = -1$ and $x = 1$, respectively, the edges of the finite strip; these singularities are properly removed after the strip is mapped onto the unit disk.

5.4.3   Exact Higher-Order Terms

In an effort to obtain further insight into the nature of the solution σ of Eq. (5.14), we next derive exact, closed-form expressions for μ_n for all n in terms of iterated, multiple integrals. For this purpose, we exploit the $\mathcal{L}$ operator introduced above. We observe that Eq. (5.46) has the integral representation

$$\mathcal{L}[e^{-s(1+t_0^2)}] = \int dt_1 \frac{e^{-2\text{Pe}(1+t_0^2)}}{\pi\sqrt{2+t_0^2}} \frac{t_1^2}{2+t_0^2+t_1^2} e^{-v(1+t_1^2)}, \tag{5.50}$$

where the last factor in the integrand has the same form as the $e^{-s(1+t_0^2)}$ term, on which the $\mathcal{L}$ acts in Eq. (5.45), with the s being replaced by v and the t_0 being replaced by t_1. It follows that the μ_n is expressed as the n-th power of $\mathcal{L}$ acting on a term of the form $e^{-s(1+t^2)}$, $\mathcal{L}^n[e^{-s(1+t^2)}]$. Thus, by induction, μ_n is expressed as an iterated, multiple integral of the independent variable s or v,

$$\mu_n(u) = e^{-2n\text{Pe}} \int dt_0 \int dt_1 (Q_0 R_1) \int dt_2 (Q_1 R_2) \cdots \int dt_n (Q_{n-1} R_n) e^{-u(1+t_n^2)}, \tag{5.51}$$

where $u \equiv s$ for even n and $u \equiv v$ for odd n, and Q_n and R_n are defined by

$$Q_n \equiv \frac{e^{-2\text{Pe}t_n^2}}{\pi\sqrt{2+t_n^2}}, \qquad R_n \equiv \frac{t_n^2}{2+t_{n-1}^2+t_n^2}. \tag{5.52}$$

As indicated from Eq. (5.46), $\mu_n(u)$ has has the singularity $u^{-1/2}$ at $u = 0$ which

---

comes from the last integral of Eq. (5.51). Thus we can single out the singular behavior as $\mu_n(u) = \sqrt{\pi/u}\, e^{-2n\mathrm{Pe}-u}\, F_n(u)$ and the singular-free part, F_n, is given by

$$
\begin{aligned}
F_n(u) = \int dt_0 \int dt_1 (Q_0 R_1) \int dt_2 (Q_1 R_2) \cdots \\
\cdots \int dt_{n-1}(Q_{n-2}R_{n-1}) \left[Q_{n-1} - \sqrt{\frac{u}{\pi}}\, e^{2u-(2\mathrm{Pe}-u)t_{n-1}^2-1} \mathrm{erfc}\sqrt{u(2+t_{n-1}^2)} \right],
\end{aligned}
\tag{5.53}
$$

where Eqs. (5.46) and (5.50) are used to evaluate the last integral.

Thus, the nth term for the flux on the strip, $\sigma_n(x)$, is given by

$$
\begin{aligned}
\sigma_{n=2k}(x) &= 2\sqrt{\frac{\mathrm{Pe}}{\pi}}\, \frac{e^{-2n\mathrm{Pe}}}{\sqrt{2(1+x)}}\, F_n(\,\mathrm{Pe}(1+x)\,), \\
\sigma_{n=2k+1}(x) &= 2\sqrt{\frac{\mathrm{Pe}}{\pi}}\, \frac{e^{-2(n-x)\mathrm{Pe}}}{\sqrt{2(1+x)}}\, F_n(\,\mathrm{Pe}(1-x)\,).
\end{aligned}
\tag{5.54}
$$

On the unit circle $\sigma_n(\theta)$ is free of singularities in θ and is expressed as

$$
\begin{aligned}
\sigma_{n=2k}(\theta) &= 2\sqrt{\frac{\mathrm{Pe}}{\pi}}\, e^{-2n\mathrm{Pe}} \left|\sin\frac{\theta}{2}\right| F_n(\,\mathrm{Pe}(1+\cos\theta)\,), \\
\sigma_{n=2k+1}(\theta) &= 2\sqrt{\frac{\mathrm{Pe}}{\pi}}\, e^{-2(n-\cos\theta)\mathrm{Pe}} \left|\cos\frac{\theta}{2}\right| F_n(\,\mathrm{Pe}(1-\cos\theta)\,).
\end{aligned}
\tag{5.55}
$$

It has not been possible to evaluate σ_n from Eq. (5.55) in simple closed form, except for $n = 1,\ 2$, as described by Eq. (5.49). However, the numerical integrations over the variables t_j $(j = 1,\ 2,\ \ldots\ n)$ for each σ_n can be carried out efficiently by using recursion.

We verify that the sum for the flux, $\sigma \sim \sigma_0 + \sigma_1 + \ldots + \sigma_n$, calculated for finite n via the numerical integration of Eq. (5.55), indeed approaches the numerical solution of Sec. 5.3. In Fig. 5-7, we show a comparison of the numerical solution of Sec. 5.3 for $\sigma(0)$ and $\sigma(\pi)$ with formula Eq. (5.55) for different values of n. Because $\sigma_{n=2k}(\theta)$ and $\sigma_{n=2k+1}(\theta)$ vanish at $\theta = 0$ and $\theta = \pi$, respectively, the term $\sigma_{n=2k}(\theta)$ affects only $\sigma(\pi)$ whereas the term $\sigma_{n=2k+1}(\theta)$ affects only $\sigma(0)$.

Remarkably, with only a few terms, our approximation is uniformly accurate down to values of Pe of order 10^{-2} or lower, which could hardly be called "high", while some correction terms $\mu_{n\geq2}$ may not be small. This behavior suggests that there may be an intermediate region of overlap between asymptotic approximations for high and low Pe. Indeed, by combining such approximations below, we will construct a very accurate approximation for all
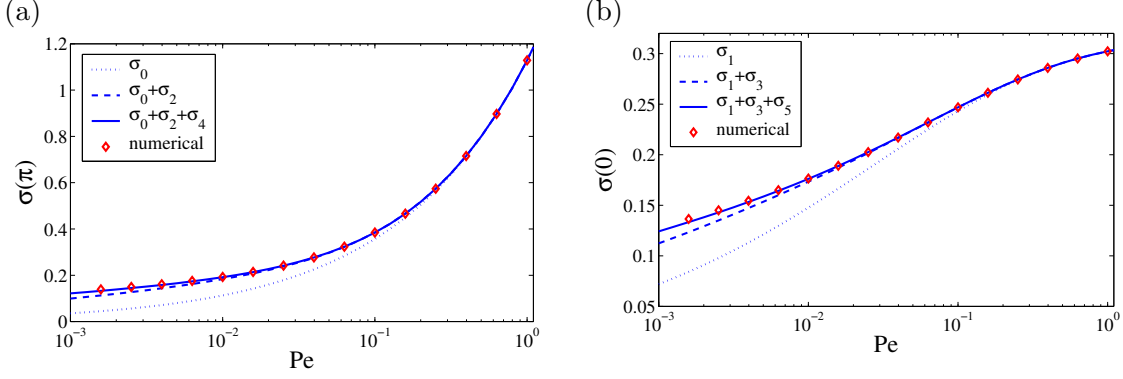
Figure 5-7: The Asymptotic approximations for high Pe compared with our numerical solution: (a) Upstream flux, $\sigma(\theta = \pi; \text{Pe})$ and (b) downstream flux, $\sigma(\theta = 0; \text{Pe})$. The integrals in the asymptotic corrections, σ_n ($1 \leq n \leq 5$), were performed numerically.

θ and all Pe.

The closed-form expression of σ_n also serves as another "numerical method" for high Pe. The multiple integrals in Eq. (5.53) can be numerically evaluated in a recursive way; the intermediate calculation steps for F_k recur in the calculation for all $F_{n>k}$. Thus, the computational cost for $\sum_{k=0}^{n} \sigma_k$ is the same as that for σ_n, which scales linearly with n.

5.4.4 Convergence of the Asymptotic Series

We next discuss the convergence properties of the asymptotic series $\sum_n \sigma_n(\theta)$ for σ on the unit circle. Because the maximum of $\sigma_n(\theta)$ occurs at $\theta = \pi$ for $n = 2k$ and at $\theta = 0$ for $n = 2k + 1$, it is readily shown that

$$||\sigma_0|| = 2\sqrt{\frac{\text{Pe}}{\pi}} \quad \text{and} \quad \begin{cases} ||\sigma_{n=2k}|| = e^{-4\text{Pe}k} \, ||F_{2k}|| \, ||\sigma_0|| \\ ||\sigma_{n=2k+1}|| = e^{-4\text{Pe}k} \, ||F_{2k+1}|| \, ||\sigma_0||, \end{cases} \quad (5.56)$$

From Eq. (5.53), $||F_n||$ is simply $F_n(u = 0)$. In particular, for $n = 1, 2$, $||F_n||$ are evaluated in simpler forms:

$$||F_1|| = \frac{e^{2\text{Pe}}}{\pi} K_0(2\text{Pe}), \quad ||F_2|| = \frac{e^{4\text{Pe}}}{\pi^2} \left\{ \frac{K_0(2\text{Pe})^2}{2} - \int_{2\text{Pe}}^{\infty} dt \, K_0(t)^2 \right\}. \quad (5.57)$$

We have not been able to further simplify the expressions for $||F_{n>2}||$. We now show that each $||F_n||$ is bounded by a function of Pe that ensures convergence of the series $\sum_n \sigma_n$

for Pe $\geq O(1)$. By noting that $Q_n < 2^{-1/2}e^{-2\mathrm{Pe}t_n^2}$ and $R_n < 1/\pi$, we find

$$||F_n|| < \pi^{-n/2}\,(4\mathrm{Pe})^{-n/2}, \tag{5.58}$$

for any Pe > 0. Hence, by Eq. (5.56) the series $\sum_n \sigma_n$ is characterized by geometric convergence in the parameter $\mathrm{Pe}^{-1/2}$ for Pe $\geq O(1)$. Finally, for large Pe and fixed n the asymptotic behavior of $||F_n||$ with respect to Pe is obtained via scaling the original variables t_k as $\tau_k = t_k\sqrt{2\mathrm{Pe}}$ $(k = 0, \ldots, n-1)$,

$$||F_{n\geq 1}|| \sim \frac{1}{2\sqrt{\pi\mathrm{Pe}}}\left(\frac{1}{16\sqrt{\pi}\mathrm{Pe}^{3/2}}\right)^{n-1} \quad \text{as} \quad \mathrm{Pe} \to \infty. \tag{5.59}$$

Formulae Eqs. (5.58) and (5.59) indicate that the series $\sum_n \sigma_n$ converges geometrically for a wide range of Pe.

We check numerically that $||F_n||$ decays exponentially in n for a wide range of Pe, $||F_n|| \sim \rho^{-n}$ as $n \to \infty$ where $\rho = \rho(\mathrm{Pe}) > 0$ is the "decay rate" of $||F_n||$, which is independent of n. For this purpose, we examine the ratio $||F_n||/||F_{n+1}||$ as a function of both n and Pe, expecting that this ratio approaches a constant for fixed Pe as n becomes sufficiently large, as shown in Fig. 5-8(a)$\sim$(c). From Fig. 5-8(d) we find that the relative error in the approximation of σ by the sum $\sum_{k=1}^5 \sigma_k$ becomes higher than 1% only when Pe $< 6.5 \times 10^{-3}$.

5.5 Uniformly Accurate Asymptotics For Low Péclet Numbers

In this section we solve approximately the integral equation Eq. (5.14) for the surface flux $\sigma(x)$, for all x in $(-1, 1)$, when Pe is sufficiently small, Pe $< O(1)$. For this purpose, we define the dependent variable $\nu(x) = e^{-\mathrm{Pe}\,x}\sigma(x)$. Equation Eq. (5.14) thus becomes

$$\int_{-1}^{1} dx'\, K_0(\mathrm{Pe}|x - x'|)\,\nu(x') = \pi e^{-\mathrm{Pe}\,x}, \qquad -1 < x < 1. \tag{5.60}$$
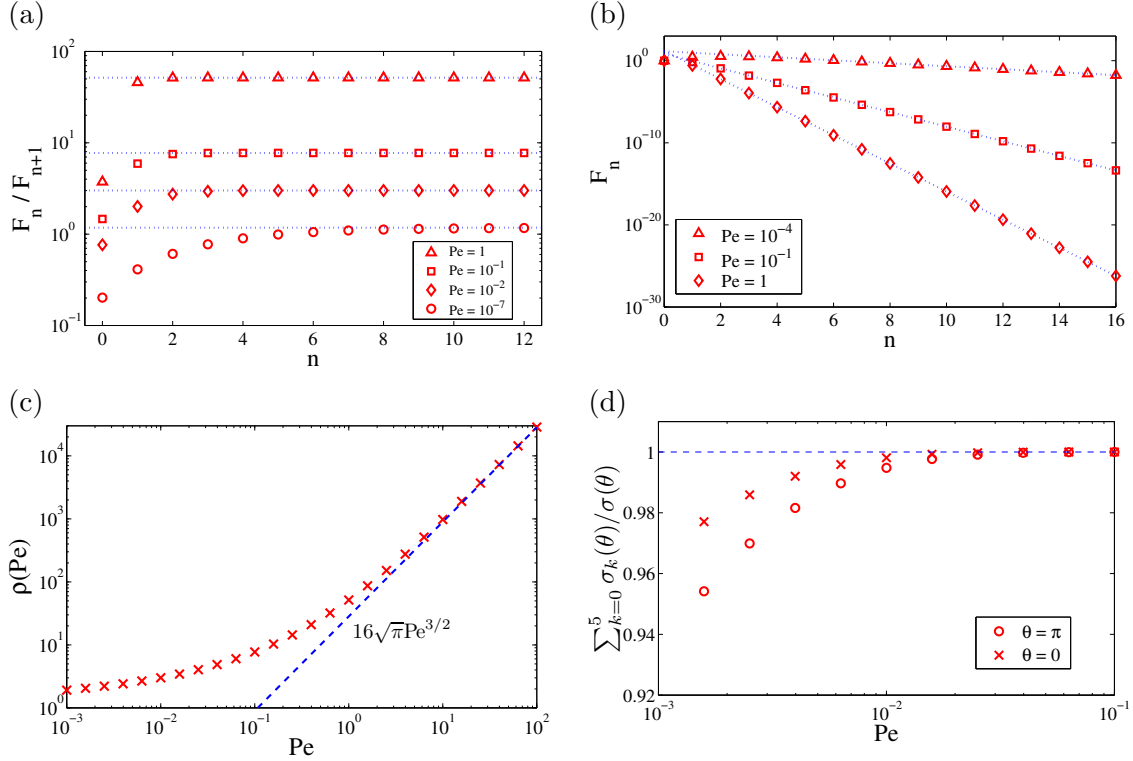
Figure 5-8: Numerical evidence for the convergence of the iteration series $\sum_n \sigma_n \sim \sigma$. (a) The ratio $||F_n||/||F_{n+1}||$ as a function of n for different values of Pe. The convergence of $\sum_n \sigma_n$ is guaranteed if $||F_n||/||F_{n+1}|| > 1$ by virtue of Eq. (5.56). (b) The term $||F_n||$ as a function of n for different values of Pe. (c) The decay rate $\rho(\text{Pe})$ of $||F_n||$ as a function of Pe, where $\rho = \lim_{n\to\infty}(||F_n||/||F_{n+1}||)$. The asymptotic behavior Eq. (5.59) is shown to be attained for Pe > 10. (d) The ratio of $\sum_{k=1}^{5} \sigma_k(\theta)$ to $\sigma(\theta)$ as a function of small values of Pe and $\theta = 0, \pi$, where $\sigma(\theta)$ is evaluated numerically by the method of Sec. 5.3.

Because the argument of the kernel is also sufficiently small, $\text{Pe}|x - x'| < O(1)$, we invoke the expansion

$$K_0(\text{Pe}|x - x'|) \sim -I_0(\text{Pe}|x - x'|) \ln\left(\frac{\text{Pe}}{2}|x - x'|\right) + \sum_{m=0}^{M} \frac{\psi(m+1)}{(m!)^2}\left(\frac{\text{Pe}|x - x'|}{2}\right)^{2m}, \quad (5.61)$$

where it is understood that

$$I_0(\text{Pe}|x - x'|) \sim \sum_{m=0}^{M} \frac{2^{-2m}\text{Pe}^{2m}|x - x'|^{2m}}{(m!)^2}, \quad (5.62)$$

and $\psi(z)$ is the logarithmic derivative of the Gamma function, $\psi(z) = \frac{d}{dz}\ln\Gamma(z)$. It was first pointed out by Pearson [88] that the resulting integral equation can be solved exactly for any finite number of terms, M, but the procedure becomes increasingly cumbersome with M.

To leading order we consider $M = 0$ in Eqs. (5.61) and (5.62). Eq. (5.60) thus reduces to a variant of Carleman's equation [99],

$$\int_{-1}^{1} dx' \ln(|x - x'|)\, \nu_0(x') = C_1 - \pi e^{-\text{Pe}\,x}, \quad (5.63)$$

where $\gamma = -\psi(1) = 0.577215\cdots$ is the Euler number, $\nu_0(x) \sim \nu(x)$ is the corresponding approximation for $\nu(x)$, and C_1 is the constant

$$C_1 = -[\gamma + \ln(\text{Pe}/2)] \int_{-1}^{1} dx'\, \nu_0(x'). \quad (5.64)$$

Following Carrier et al. [65], we introduce the complex function

$$\Pi(z) = \frac{\sqrt{z^2 - 1}}{2\pi i} \int_{-1}^{1} dx'\, \frac{\nu_0(x')}{x' - z} \quad (5.65)$$

and single out the limit values

$$\Pi^{\pm}(x) \equiv \lim_{\varepsilon \to 0} \Pi(x \pm i\varepsilon) = \pm\frac{\sqrt{1 - x^2}}{2\pi} \lim_{\varepsilon \to 0} \int_{-1\mp i\varepsilon}^{1\mp i\varepsilon} dz'\, \frac{\nu_0(z')}{z' - x}, \quad (5.66)$$

86

by which the integral equation Eq. (5.63) is equivalent to the equations:

$$\Pi^+(x) - \Pi^-(x) = -\frac{\sqrt{1-x^2}}{\pi} \frac{d}{dx} \int_{-1}^{1} dx' \, \ln(|x-x'|) \, \nu_0(x') = -\mathrm{Pe}\sqrt{1-x^2} \, e^{-\mathrm{Pe}\,x}, \quad (5.67)$$

$$\Pi^+(x) + \Pi^-(x) = i\sqrt{1-x^2} \, \mathrm{Res}\left\{\frac{\nu_0(z')}{z'-x}; z'=x\right\} = i\sqrt{1-x^2}\,\nu_0(x). \quad (5.68)$$

First, we find $\Pi(z)$ via applying directly the Mittag-Leffler expansion theorem to Eq. (5.67) [65]:

$$\Pi(z) = -\frac{1}{2\pi i}\left(\mathrm{Pe}\int_{-1}^{1} dx' \, \frac{\sqrt{1-x'^2}}{x'-z} \, e^{-\mathrm{Pe}\,x'} + A\right), \quad (5.69)$$

where $-(2\pi i)^{-1} A$ is the limit as $z \to \infty$ of the function $\Pi(z)$; by inspection of Eq. (5.65),

$$A = \int_{-1}^{1} dx' \, \nu_0(x'). \quad (5.70)$$

We recognize that the constant C_1 of Eq. (5.64) is $C_1 = -[\gamma + \ln(\mathrm{Pe}/2)]A$.

Next, we obtain the approximate solution $\nu_0(x)$ in terms of this A by Eq. (5.67):

$$\nu_0(x) = \frac{1}{\pi\sqrt{1-x^2}}\left[\mathrm{Pe}\,(P)\int_{-1}^{1} dx' \, \frac{\sqrt{1-x'^2}}{x'-x} \, e^{-\mathrm{Pe}\,x'} + A\right], \quad (5.71)$$

where $(P)\int_{-1}^{1}$ denotes the principal value of the integral. In order to determine the unknown constant A, we multiply both sides of Eq. (5.63) by $(1-x^2)^{-1/2}$ and integrate over $(-1, 1)$ by use of the elementary integral [65]

$$\int_{-1}^{1} dx \, \frac{\ln(|x-x'|)}{\sqrt{1-x^2}} = -\pi \ln 2. \quad (5.72)$$

A few comments on this result are in order. It can be obtained via differentiating the left-hand side with respect to x', and thus converting the integral to a Cauchy principal value which is found directly to vanish identically. Hence, the original integral is independent of x' and can be evaluated for $x' = 0$ by changing the variable to $x = (\xi - 1/\xi)/(2i)$, where ξ moves on the unit circle, and applying the residue theorem [65]. We thus find

$$A = -\frac{1}{\gamma + \ln(\mathrm{Pe}/4)} \int_{-1}^{1} dx \, \frac{e^{-\mathrm{Pe}\,x}}{\sqrt{1-x^2}}, \quad (5.73)$$

$$\nu_0(x) = \frac{1}{\pi\sqrt{1-x^2}} \left[\mathrm{Pe} \cdot (P) \int_{-1}^{1} dx' \, \frac{\sqrt{1-x'^2}}{x'-x} e^{-\mathrm{Pe}\,x'} - \frac{1}{\gamma + \ln(\mathrm{Pe}/4)} \int_{-1}^{1} dx' \, \frac{e^{-\mathrm{Pe}\,x'}}{\sqrt{1-x'^2}} \right].$$

$$(5.74)$$

It is straightforward to carry out the integrations in Eq. (5.74). The second integral on the right-hand side is simply a modified Bessel function of the first kind:

$$\int_{-1}^{1} dx \, \frac{e^{-\mathrm{Pe}\,x}}{\sqrt{1-x^2}} = \int_{0}^{\pi} dt \, e^{-\mathrm{Pe}\cos t} = \pi J_0(i\mathrm{Pe}) = \pi I_0(\mathrm{Pe}). \tag{5.75}$$

The remaining integral can be converted to one that is directly amenable to numerical computation for $\mathrm{Pe} \le O(1)$. By defining

$$\mathcal{I}(\mathrm{Pe}; x) = (P) \int_{-1}^{1} dx' \, \frac{\sqrt{1-x'^2}}{x'-x} e^{-\mathrm{Pe}(x'-x)}, \tag{5.76}$$

we evaluate the derivative

$$e^{-\mathrm{Pe}\,x} \frac{\partial \mathcal{I}}{\partial \mathrm{Pe}} = - \int_{-1}^{1} dx' \, \sqrt{1-x'^2} \, e^{-\mathrm{Pe}\,x'} = -\pi[I_0(\mathrm{Pe}) - I_0''(\mathrm{Pe})] = -\pi \frac{I_1(\mathrm{Pe})}{\mathrm{Pe}}, \tag{5.77}$$

where I_ν is the modified Bessel function of the first kind. An expression for the integral Eq. (5.76) then follows by direct integration in Pe of Eq. (5.77):

$$\mathcal{I}(\mathrm{Pe}; x) = \mathcal{I}(0; x) - \pi \int_{0}^{\mathrm{Pe}} dt \, e^{tx} \frac{I_1(t)}{t}, \tag{5.78}$$

where

$$\mathcal{I}(0; x) = -(1-x^2) \frac{d}{dx} \int_{-1}^{1} dx' \, \frac{\ln(|x-x'|)}{\sqrt{1-x'^2}} - \pi x = -\pi x. \tag{5.79}$$

Hence,

$$\mathcal{I}(\mathrm{Pe}; x) = -\pi x - \pi \int_{0}^{\mathrm{Pe}} dt \, e^{tx} \frac{I_1(t)}{t}. \tag{5.80}$$

The approximation

$$\gamma + \ln(\mathrm{Pe}/4) \sim -K_0(\mathrm{Pe}/2), \tag{5.81}$$

which becomes useful in Sec. 5.6 where we construct a uniform formula for all Pe and local coordinate of the boundary, and the use of Eqs. (5.75), (5.80) and $\sigma(x) = e^{\mathrm{Pe}\,x}\nu(x)$ yield a

low-Pe approximation for the flux on the boundary of the finite strip, $\sigma^{(\mathrm{lo})} = e^{\mathrm{Pe}\,x}\nu_0(x)$,

$$\sigma(x) \sim \sigma^{(\mathrm{lo})}(x) = \frac{1}{\sqrt{1-x^2}}\left\{\frac{I_0(\mathrm{Pe})}{K_0(\mathrm{Pe}/2)}\,e^{\mathrm{Pe}\,x} - \mathrm{Pe}\left[x + \int_0^{\mathrm{Pe}} dt\, e^{tx}\,\frac{I_1(t)}{t}\right]\right\}. \tag{5.82}$$

Hence, by virtue of Eq. (5.22), the flux on the unit circle is

$$\sigma(\theta) \sim \sigma^{(\mathrm{lo})}(\theta) = \frac{I_0(\mathrm{Pe})}{K_0(\mathrm{Pe}/2)}\,e^{\mathrm{Pe}\cos\theta} - \mathrm{Pe}\left[\cos\theta + \int_0^{\mathrm{Pe}} dt\, e^{t\cos\theta}\,\frac{I_1(t)}{t}\right]. \tag{5.83}$$

We note in passing that the integral in Eq. (5.82) can be expressed as a powers series in Pe. With the series expansions

$$e^{tx} = \sum_{n=0}^{\infty}\frac{t^n x^n}{n!}, \quad \frac{I_1(t)}{t} = \sum_{m=0}^{\infty}\frac{t^{2m}}{2^{2m+1}}\frac{1}{m!\,(m+1)!}, \tag{5.84}$$

it is straightforward to derive the expansion

$$
\begin{aligned}
\int_0^{\mathrm{Pe}} dt\, e^{xt}\,\frac{I_1(t)}{t} \;=\; & \sum_{l=0}^{\infty}\frac{\mathrm{Pe}^{2l+1}}{2l+1}\sum_{m=0}^{l}\frac{x^{2m}}{(2m)!\,(l-m)!\,(l-m+1)!} \\
& + \sum_{l=0}^{\infty}\frac{\mathrm{Pe}^{2(l+1)}}{2(l+1)}\sum_{m=0}^{l}\frac{x^{2m+1}}{(2m+1)!\,(l-m)!\,(l-m+1)!}.
\end{aligned} \tag{5.85}
$$

A few comments on formula Eq. (5.82) are in order. Aleksandrov and Belokon [100] expanded to high orders the kernels of the relevant class of singular integral equations and derived in generality a more accurate yet complicated formula for the solution. The procedure here, though being based on simply taking $M = 0$ in Eq. (5.61) and Eq. (5.62), leaves intact the right-hand side of Eq. (5.60) and applies Eq. (5.81); our approximate formula for $\sigma(x)$ turns out to be accurate for an extended range of low Pe. Fig. 5-9 shows a comparison of Eq. (5.83) with the numerical solution of Sec. 5.3 for a range of low Péclet numbers.
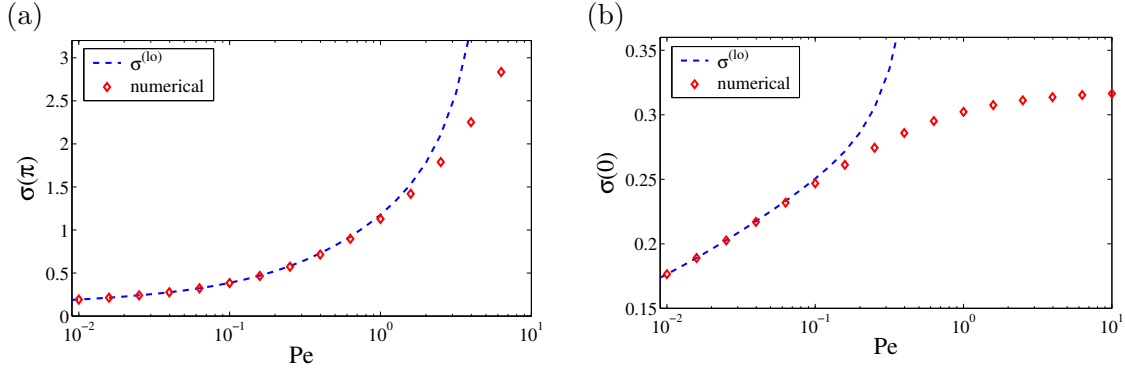
Figure 5-9: The asymptotic approximation $\sigma^{(\mathrm{lo})}(\theta;\mathrm{Pe})$ in Eq. (5.83) compared to the numerical solution of Sec. 5.3 for a range of low Pe. (a) Upstream flux, $\sigma^{(\mathrm{lo})}(\theta = \pi;\mathrm{Pe})$, and (b) downstream flux, $\sigma^{(\mathrm{lo})}(\theta = 0;\mathrm{Pe})$.

5.6 Uniformly Accurate Formula for All Positions and Péclet Numbers

5.6.1 Connecting the High and Low Pe Approximations for the flux

In Sec. 5.4 and 5.5 we derived asymptotic formulae for the surface flux σ on the boundary of the unit circular disk (or finite strip) that are valid for sufficiently high or sufficiently low Pe; these expressions, $\sigma^{(\mathrm{hi})}$ and $\sigma^{(\mathrm{lo})}$ in Eq. (5.49) and Eq. (5.83), respectively, hold for all values of the local coordinate of the absorber boundary, although we did not analyze to what extent the approximations are uniformly valid in a rigorous mathematical sense. Comparisons with the numerical results in Figs. 5-7 and 5-9 show that the approximations are comparably accurate for the rear stagnation point ($\theta = 0$) and forward stagnation point ($\theta = \pi$). We have also checked that, for fixed Pe, the errors are also comparable at intermediate values of the local coordinate ($0 < \theta < \pi$). In Fig. 5-10, we show that the two approximations, $\sigma^{(\mathrm{hi})}$ and $\sigma^{(\mathrm{lo})}$, nearly overlap for some range of values Pe near the value Pe = 0.1, while remaining remarkably close to the "exact" numerical solution from Sec. 5.3.

The existence of a regime of overlapping accuracy allows us to construct an analytical formula for σ, accurate for all values of Pe and the local coordinate of the absorbing boundary, θ, by smoothly connecting $\sigma^{(\mathrm{hi})}$ and $\sigma^{(\mathrm{lo})}$. A similar overlapping accuracy was found for a three-dimensional problem of heat or mass transfer in a steady shear flow by Phillips [71], who combined high- and low-Pe expansions only for the Nusselt number, Nu, using singular perturbation. The dependence of the flux σ on Pe can be described heuristically
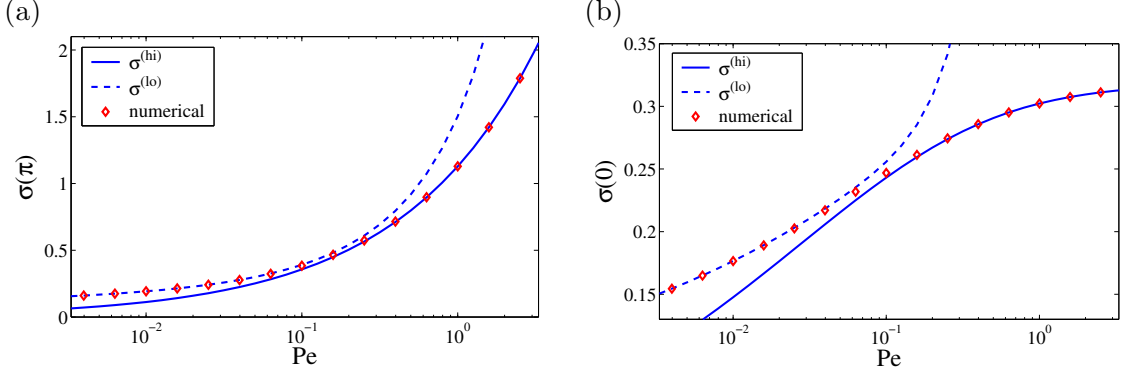
Figure 5-10: Plots of formulae Eq. (5.49) for $\sigma^{(\mathrm{hi})}$ and Eq. (5.83) for $\sigma^{(\mathrm{lo})}$ versus Pe in the same graph as the plot for the solution σ evaluated numerically by the method of Sec. 5.3. (a) Upstream flux, $\sigma(\theta = 0; \mathrm{Pe})$. (b) Downstream flux, $\sigma(\theta = \pi; \mathrm{Pe})$.

by a formula of the form

$$\sigma(\theta; \mathrm{Pe}) \sim \sigma^{(\mathrm{conn})} = \sigma^{(\mathrm{hi})}(\theta; \mathrm{Pe})\,\mathcal{U}(\mathrm{Pe}/\mathrm{P}_0) + \sigma^{(\mathrm{lo})}(\theta; \mathrm{Pe})\left[1 - \mathcal{U}(\mathrm{Pe}/\mathrm{P}_0)\right], \qquad (5.86)$$

for the entire range of Pe and θ; $\mathcal{U}(\chi)$ is a family of smooth functions defined for $\chi = \mathrm{Pe}/\mathrm{P}_0 > 0$ that at least satisfy the conditions

$$\lim_{\chi \to 0^+} \mathcal{U}(\chi) = 0, \qquad \lim_{\chi \to +\infty} \mathcal{U}(\chi) = 1. \qquad (5.87)$$

A simple choice for the step-like function, $\mathcal{U}$, which yields a rather accurate formula for σ, is

$$\mathcal{U}(\chi; \alpha) = e^{1/(1 - e^{\chi^\alpha})}, \qquad \alpha > 0. \qquad (5.88)$$

We note that there are two free parameters in Eq. (5.88) with $\chi = \mathrm{Pe}/\mathrm{P}_0$: α and P_0. The parameter P_0 corresponds to a value of Pe in the region of overlap of formulae Eqs. (5.49) and (5.83); in principle, P_0 may depend on the local coordinate, which is θ for the unit circle. The parameter α determines the steepness of the curve $\mathcal{U}(\chi)$ near $\chi = 1$.

We find that a good fit with the numerical solution is achieved for $\alpha = 2$ and $\mathrm{P}_0 = 1/6$, as shown in Fig. 5-11 where $\sigma^{(\mathrm{conn})}(\theta)$ is plotted versus Pe for $\theta = \pi$ (upstream flux) and $\theta = 0$ (downstream flux). The relative error is less than 1.75% for all values of Pe and θ. Because we have the exact Green's function Eq. (5.12), this uniform accuracy also carries over to the solution of the entire concentration field, $c(x, y; \mathrm{Pe})$, obtained from the integral Eq. (5.13).

91
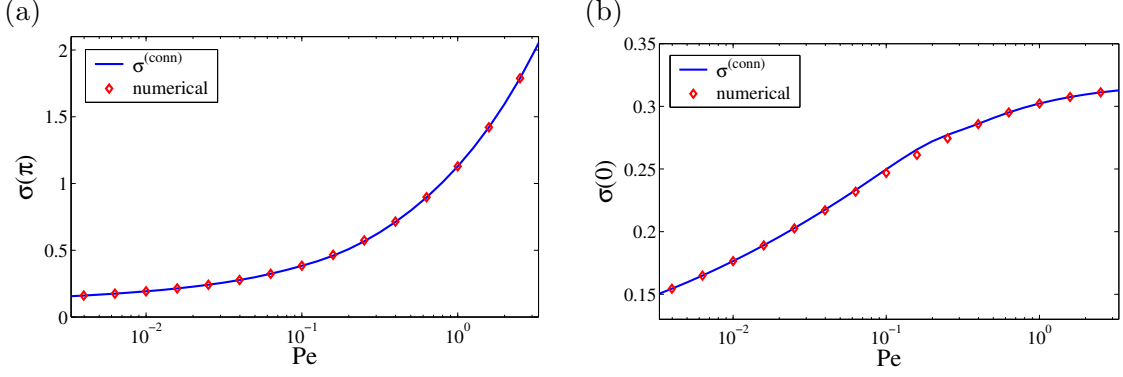
Figure 5-11: Plots of the connection formula, $\sigma^{(\text{conn})}$, from Eqs. (5.86) and (5.88), in comparison to the numerical solution of Sec. 5.3: (a) Upstream flux, $\sigma(\theta = \pi; \text{Pe})$, and (b) downstream flux, $\sigma(\theta = \pi; \text{Pe})$. The relative error of $\sigma^{(\text{conn})}$ compared to the numerical solution is less than 1.75% for all values of Pe and θ, and it becomes negligibly small at high and low Pe for all θ.

Our analytical approximation also describes an absorber of arbitrary shape obtained by conformal mapping, $z = g(w)$ ($w = e^{i\theta}$). The flux distribution on the unit circle, $\sigma^{(\text{conn})}(\theta)$, is transformed to the new surface using Eq. (5.21). Because the flux is proportional to a gradient, it is locally amplified by a factor of $|g'(w)|^{-1}$, which may cause relative errors larger than 1.75% in some locations, e.g. near a cusp, where conformality breaks down ($g' = 0$). For a well behaved univalent mapping, however, the approximation should remain very accurate for all positions, $g(e^{i\theta})$ and Pe, so the general BVP may be considered effectively solved.

5.6.2 The Total Flux to the Absorber

It is straightforward to obtain a uniformly accurate approximation of the Nusselt number by integrating the flux on the unit circle or the finite strip:

$$\text{Nu}(\text{Pe}) = \int_0^{2\pi} d\theta \, \sigma(\theta; \text{Pe}) = 2 \int_{-1}^1 dx \, \sigma(x; \text{Pe}). \qquad (5.89)$$

The leading-order expressions of Nu(Pe) in the high and low Pe limits are thus obtained by integrating Eqs. (5.48) and (5.82) using integration by parts and the identity $xI_0(x) =$

(a)   (b)
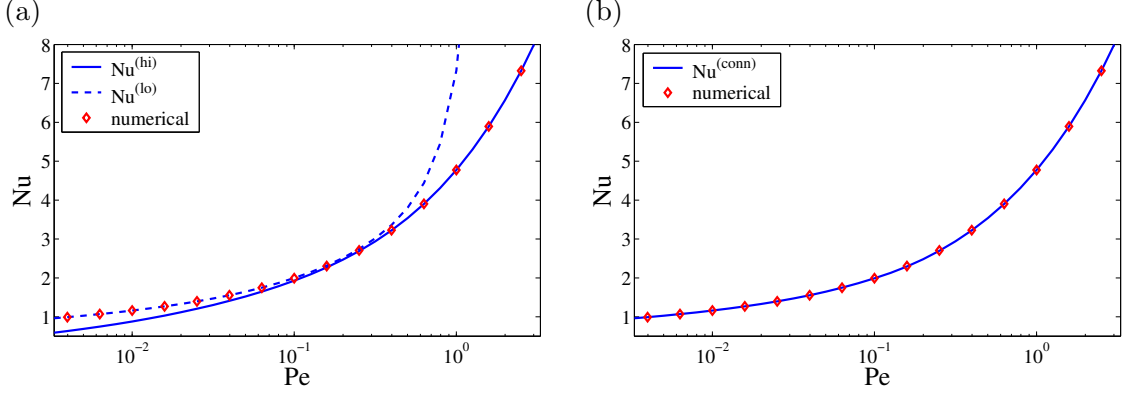
Figure 5-12: The Nusselt number, Nu, which gives the total flux to the absorber, versus the Péclet number, quantifying the importance of advection compared to diffusion. In (a) the asymptotic expressions Eq. (5.90) overlap for $0.1 < \text{Pe} < 0.4$. In (b) the analytical connection formula Eq. (5.91) compares very well with the "exact" numerical result from Sec. 5.3. The results hold for absorbers of arbitrary shape, as long as Pe is the renormalized Péclet number, $\text{Pe} = A_1 \text{Pe}_o$, where A_1 is the conformal radius and Pe_o is the bare Péclet number for the unit circle.

$[xI_1(x)]'$ [101],

$$\begin{aligned}
\text{Nu}^{(\text{hi})}(\text{Pe}) &= \frac{8}{\pi}\left\{\sqrt{\frac{\text{Pe}}{\pi}}e^{-2\text{Pe}}K_0(2\text{Pe}) + \text{Pe}e^{2\text{Pe}}\text{erf}(2\sqrt{\text{Pe}})[K_0(2\text{Pe}) + K_1(2\text{Pe})]\right\}, \\
\text{Nu}^{(\text{lo})}(\text{Pe}) &= 2\pi\left\{\frac{I_0(\text{Pe})^2}{K_0(\text{Pe}/2)} + (\text{Pe})^2[I_1(\text{Pe})^2 - I_0(\text{Pe})^2] + \text{Pe}I_0(\text{Pe})\,I_1(\text{Pe})\right\}.
\end{aligned} \tag{5.90}$$

The uniform analytical approximation for Nu(Pe) follows as

$$\text{Nu}^{(\text{conn})}(\text{Pe}) = \text{Nu}^{(\text{hi})}(\text{Pe})\,e^{1/(1-e^{36\text{Pe}^2})} + \text{Nu}^{(\text{lo})}(\text{Pe})\,[1 - e^{1/(1-e^{36\text{Pe}^2})}]. \tag{5.91}$$

As shown in Fig. 5-12, this analytical result is quite accurate over the entire range of Péclet numbers, and it becomes exact as $\text{Pe} \to 0$ and $\text{Pe} \to \infty$. The maximum relative error is found to be 0.53%. We are not aware of any such analytical formula for the complete Nusselt-Péclet relation of a finite absorber.

It may come as a surprise that the same result Eq. (5.90) also holds for an absorber of arbitrary shape, obtained by conformal mapping of the unit circle, $z = g(w)$, without any additional error. The reason is that the total flux through any contour is preserved *exactly* under every conformal mapping of a conformally invariant BVP [62]. When computing Nu from Eq. (5.89) for another shape, therefore, one must simply use the renormalized Péclet number, $\text{Pe} = A_1\text{Pe}_o$, equal to the conformal radius, A_1, times the bare Péclet number, Pe_o,

for the unit circle.

5.7 Conclusion

5.7.1 Summary of Results

We have performed a detailed study of the BVP Eqs. (5.3)∼(5.5) for a finite absorber of arbitrary cross section in a steady two-dimensional potential flow. Our focus has been the flux profile on the boundary, σ, from which the concentration can be obtain everywhere in the plane by convolution with the known Green's function. We have explicitly considered several simple cases, notably the canonical problem of uniform flow past a circular cylinder, which can be mapped to arbitrary geometries by conformal mapping, as described in Sec. 5.2.

In Sec. 5.3, we presented an efficient numerical method to solve the BVP. We began by mapping the BVP to the inside of the unit circle in order to work with a bounded domain. We then eliminated some "far-field" singularities (at the origin) using exact asymptotics and applied a spectral method in polar coordinates, with exponential convergence in the number of nodes. We also used an adaptive mesh to deal with boundary layers at very high Péclet numbers. The results, which are illustrated in Figs. 5-2 and 5-4, provided reliable tests of our analytical approximations.

In Sec. 5.4 and 5.5, we derived distinct asymptotic expansions for the flux on the boundary of the finite strip for high and low Pe, respectively, starting from a well known integral equation in streamline coordinates [78], which has been studied extensively in the theory of solidification and freezing in a flowing melt [80, 81, 64, 82, 83, 84, 60]. We used some original variations on classical techniques from the theory of singular integral equations, including the Wiener-Hopf method of factorization, to obtain improvements on previous approximations.

Noteworthy features of our expansions for high Pe are: (i) The summands admit closed-form expressions in terms of multiple integrals Eq. (5.55), which are straightforward to evaluate numerically; (ii) the expansions converge for all distances along the strip for a wide range of Pe, Pe $\geq O(10^{-2})$; and (iii) only the small number of terms in Eq. (5.49) can be retained for reasonable accuracy though the number increases as Pe decreases. On the other hand, our asymptotic formula Eq. (5.83) for low Pe is accurate for Pe $\leq 10^{-1}$, which

renders it possible to have a region where the two expansions overlap.

Therefore, we were able to construct an *ad hoc* analytical connection formula Eq. (5.86), which reproduces our numerical results for the flux to a circular absorber with less than 1.75% relative error for all angles and Péclet numbers, as shown in Fig. 5-11. We also predicted the Nu(Pe) relation Eq. (5.89) with comparable accuracy, as shown in Fig. 5-12. These results constitute a nearly exact, analytical solution to the BVP Eqs. (5.3)∼(5.5).

The main contribution of our work is a unified description of the crossover regime, interpolating between the well known asymptotic limits of high and low Pe. As such, we can draw some mathematical and physical conclusions about the transition in the following sections.

5.7.2 Mathematical Discussion

A posteriori, we may try to understand why perturbation methods, which ostensibly require extreme values of Pe, produce a very accurate analytical solution for *all* values of Pe. One technical reason is that our high-Pe approximation, $\sigma^{(\mathrm{hi})}$, is not the usual asymptotic series of singular perturbation, since we have essentially "summed" parts of a naive expansion exactly in the Bessel function terms of Eq. (5.49). This allows the approximation to be more accurate than a simple power-series type of expansion, presumably extending its validity to somewhat higher Pe. Still, the neglected higher-order terms involve powers of Pe, which become important as Pe becomes small.

As we have mentioned throughout this chapter, similarity solutions govern the asymptotic limits. For Pe $\to$ 0, we are perturbing around the trivial similarity solution with uniform diffusive flux from infinity, $\sigma =$constant and $c(r, \theta) \propto \ln r$. As shown in Fig. 5-4(a) for Pe $= 0.01$, a small amount of fluid flow changes this picture only slightly near the disk, by favoring flux to one side compared to the other. When Pe $= 1$, as in Fig. 5-4(b), the region of depleted concentration begins to be swept significantly downstream by the flow. This causes the low-Pe approximation to break down near the rear stagnation point, while remaining fairly accurate near the forward stagnation point, as shown in Fig. 5-9.

The high-Pe approximation is derived by perturbing around a different similarity solution Eq. (5.24) for an absorbing circular rim on an absorbing flat plate [62]. In this advection-dominated regime, there is a thin diffusion layer of width, $O(1/\sqrt{\mathrm{Pe}})$, around the disk, as shown in Fig. 5-4(c), which provides the first term in the approximation Eq. (5.83). The

asymptotic corrections in Sec. 5.4 are obtained by effectively removing the "false plate" from the similarity solution, downstream from the disk.

To understand the influence of downstream perturbations, consider the Green's function Eq. (5.12), which has the asymptotic form

$$G(x,y) \sim \frac{e^{\text{Pe}(x-r)}}{\sqrt{8\pi \text{Pe}\, r}} \quad \text{as} \quad r = \sqrt{x^2 + y^2} \to \infty. \tag{5.92}$$

The Green's function decays exponentially at the scale of Pe in all directions, except precisely downstream, where it is long-ranged: $G(x,0) \sim 1/\sqrt{8\pi \text{Pe}\, x}$ as $x \to \infty$ for $y = 0$. Therefore, all corrections to the leading-order similarity solution Eq. (5.24) decay exponentially upstream beyond an $O(\text{Pe})$ distance from the rear stagnation point. Our high-Pe approximation, $\sigma^{(\text{hi})}$, in Eq. (5.49) captures the first such correction, which is needed for uniform accuracy over the disk. Further corrections are $O(e^{-4\text{Pe}})$, as is clear from formulae Eq. (5.56).

The fact that the approximation breaks down when $e^{4\text{Pe}}$, rather than Pe, gets close to unity explains the fortuitous accuracy of $\sigma^{(\text{hi})}$ down to Pe $= 0.1$. Higher-order terms further extend the region of accuracy by orders of magnitude, e.g., to Pe $= O(10^{-3})$ for five terms, as shown in Fig. 5-7. Because the approximation is valid for a wide range of Pe that would not be considered "high", it overlaps with the low-Pe approximation.

We also mention some directions for further analysis. The analytical treatment on the basis of an integral equation essentially avoids the complications of boundary-layer theory applied directly to the BVP [102]. In that sense, it resembles renormalization-group (RG) methods for PDEs [103, 104], which provide a general means of deriving asymptotic expansions in place of traditional problem-specific singular-perturbation methods. An attractive feature of RG methods is that they promise to produce globally valid approximations *directly*, without the need to combine distinct overlapping expansions, as we have done. It would be interesting to see if this could possibly be accomplished for our BVP, and, if so, whether the resulting approximations are any simpler or more accurate than ours. We leave this as an open challenge to RG aficionados.

From the point of view of mathematical methods, another interesting observation is that the BVP Eqs. (5.3)~(5.5) can be formulated in analogous way to the problem of wave scattering by a finite strip [105] in acoustics or electromagnetics, which has some variants

with other geometries such as the scattering by a broken corner [106]. Such problems, where the requisite PDEs are or can be reduced to Helmholtz-type equations by simple transformations, can be described alternatively by finite sets of nonlinear ODEs in which the length of the strip, or the Péclet number Pe in the present case, is the independent variable. The underlying method is an improvement over Latta's method [107] for the solution of a class of singular integral equations via their exact conversion to ODEs.

Another technical question is how to place the method of high-Pe expansion pursued in Sec. 5.4 on a more firm mathematical ground. To address this issue, two of us have developed an equivalent approach based on a generalization of the Wiener-Hopf technique applied to the BVP Eqs. (5.3)$\sim$(5.5) in the Fourier domain, which yields the same results as the iteration scheme of Sec. 5.4 [94]. Since the Wiener-Hopf method is well known in this context for a semi-infinite strip [65], it would be interesting to ask how the method might be extended for the present case of a finite strip, or perhaps more general situations, such as multiple strips, or three-dimensional objects.

A more careful comparison should be made of our numerical solutions with the works by Kornev and Mukhamadullina [64]. Our method in Sec. 5.3 seems to require more computational resources to obtain the same level of accuracy because it solves a two-dimensional BVP, whereas the other method solves a one-dimensional integral equation. Aspects of the technique in Sec. 5.4.3 also need to be studied further, especially the number of the required terms versus Pe, the accuracy for Pe $\ll$ 1 and the propagation of error through the requisite multiple integrals.

5.7.3   Physical Discussion

Our analysis provides quantitative information about the crossover between diffusion-dominated and advection-dominated adsorption, which is important in applications. As described above, the former regime, at low Pe, is characterized by a broad diffusion layer extending in all directions like a "cloud", with the flow causing only a minor broken symmetry, as shown in Fig. 5-4(a). In contrast, at high Pe, concentration gradients are confined to a thin boundary layer around the object, which separates into a long thin "wake" near the rear stagnation point, as shown in Fig. 5-4(c).

What is the critical Pe for the cloud-to-wake transition? Of course, the answer depends on one's definition, but the shape of the object also plays a role. In streamline coordinates,
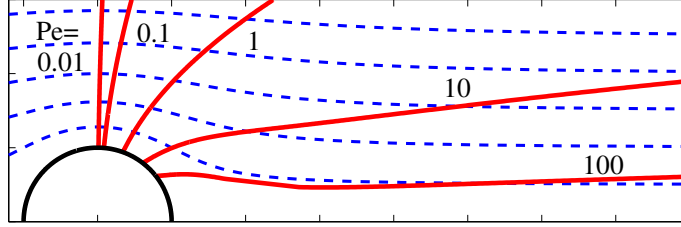
Figure 5-13: The locus of points, for various values of Pe, (solid lines) where the concentration c attains its maximum along the streamlines (dashed lines) around a circular disk for desorption into an unconcentrated fluid. (In the equivalent problem of absorption from a concentrated fluid, the solid curves give the minimum concentration along streamlines for different Pe.)

the transition is not so obvious since the object corresponds to an infinitely thin strip, which cannot "shield" a thinner, finite-sized wake. Objects of finite thickness, however, do show a clear transition. A uniformly valid formula for $c(x, y, \text{Pe})$ in any geometry may be obtained by inserting our expression for the flux to the strip Eq. (5.86) into the convolution integral Eq. (5.13) and conformally mapping from the desired shape to the strip, $w = f(z)$.

The cloud-to-wake transition is related to $f(z)$, as we illustrate for the case of the disk, $f(z) = z + 1/z$. The analytical approximation is nearly indistinguishable from the numerical solution in Fig. 5-4, so we consider the latter. In Fig. 5-13, we show curves where, for different values of Pe, the concentration change, relative to the background, is maximal along streamlines. Far from the disk, they approach parabolae, $\text{Pe}y^2 = 4x$, due to balance between diffusion in the y-direction scaling as $y \sim 2\sqrt{t}$ and advection in the x-direction scaling as $x \sim \text{Pe}t$. Near the object, the map causes a significant distortion of the curves, which allows us to define the critical value, $\text{Pe} = 60$, above which they become non-monotonic functions of x. At larger values of Pe, the curves get sucked back into a thinner wake region behind the disk, signifying the dominance of advection.

It is interesting to note the limiting wake structure as $\text{Pe} \to \infty$. As the concentration boundary layer wraps all the way around the disk, the downstream disturbance begins to look like that of a Green's function source located at the rear stagnation point. If one defines the "wake" as the region behind the disk enclosed by a given iso-concentration line, $c = c_0$, then it is easy to see that the wake tends to a finite length as $\text{Pe} \to \infty$, even though its thickness tends to zero, like $1/\sqrt{\text{Pe}}$. Physically, the (dimensionless) length $L = O(l_0^2 \text{Pe}) = O(1)$ is the distance traveled in the flow downstream in x during the time

for diffusion across the initial wake thickness, $l_0 = O(1/\sqrt{\mathrm{Pe}})$. For example, the $c = 0.5$ contour ends roughly 2.3 disk diameters downstream from the rear stagnation point, as $\mathrm{Pe} \to \infty$.

These results have relevance for more complicated, physical situations, such as the coating of fibers from a gas flow, where quasi-steady advection-diffusion in a two-dimensional potential flow is a reasonable model for the growth dynamics [108]. It is well known that the Péclet number, based on the fiber diameter, controls the total growth rate, as well as the uniformity of the coating's thickness, for a *single* fiber. For $\mathrm{Pe} \leq 0.1$, the flux to the disk (or fiber cross-section), $\sigma(\theta, \mathrm{Pe})$, is nearly uniform, apart from a minor asymmetry due to the flow, which is accurately described by Eq. (5.83). For $\mathrm{Pe} \geq 0.01$, the high-Pe expansion Eq. (5.49) shows how the flux profile becomes increasingly asymmetric and approaches the advection-dominated limit, $\sigma \sim 2\sqrt{\mathrm{Pe}/\pi} \sin \theta/2$ as $\mathrm{Pe} \to \infty$. Our work provides an analytical description of how this crossover occurs for the flux profile, Eq. (5.86), and the total flux, Eq. (5.89), which may be useful in future analytical or numerical studies of the coating process.

By quantifying the crossover in the concentration field, we also provide some insight into the possible effect of interactions between *multiple* nearby fibers during real coating process. In the "cloud" regime at low Pe, the concentration field approximately satisfies Laplace's equation, which means that other fibers in all directions can strongly influence the local flux, due to the long-range decay of the concentration. In the "wake" regime at high Pe, the concentration remains uniform (outside a thin boundary layer) in all directions except directly downstream, where a thin wake forms of $O(1/\sqrt{\mathrm{Pe}})$ thickness and $O(1)$ extent (at the scale of a few particle diameters). When the mean fiber spacing is larger than the typical wake length, there are negligible interactions, but, whenever a fiber ends up in the wake of another fiber, its coating becomes much thinner in a localized region, which can be undesirable. Our analysis shows that this important crossover occurs at a critical value of $\mathrm{Pe} \approx 60$.

Chapter 6

Conclusion to Part I

In the course of this thesis, we described a class of growth phenomena on two-dimensional surfaces limited by various transport processes by use of time-dependent conformal mapping. In Chap. 2 we identified non-Laplacian, yet conformally invariant, transport processes and formulated continuous and stochastic growth driven by them, generalizing viscous fingering and diffusion-limited aggregation (DLA) respectively. A waiting time was first introduced in stochastic growth, which is not clear in DLA.

In Chap. 3 we considered a representative case where advection and diffusion cause growth and simulated the stochastic version, advection-diffusion-limited aggregation (ADLA). While a universal crossover in morphology has been observed from diffusion-limited to advection-limited fractal patterns, controlled by a time-dependent Péclet number, the fractal dimension has not been affected by advection. In a theoretical approach to ADLA, we derived an equation relating both linear and non-linear averaging of conformal maps, whose mean-field theory approximation is the similarity solution of continuous growth. It agreed well with our numerical result and explained the slight disparity observed in the two asymptotic shapes.

The flux density around a finite absorber in advection-diffusion, which determines the growth probability for ADLA, is also essential in other applications such as solidification in a flowing melt. In Chap. 5 we effectively solved this nontrivial problem; an efficient numerical methods were developed, enabling ADLA simulation possible, and previously known asymptotic solutions were significantly improved by singular integral theories. In particular, we found the analytic forms of the complete high-Pe expansion and constructed

a connection formula for all Pe with a maximum relative error of 1.75%. The future work of this problem is separately discussed in Sec. 5.7.

In Chap. 4 we extended our model to non-planar manifolds. DLA has been simulated on constant curvature surfaces, i.e., elliptic and hyperbolic geometries, via stereographic projections. The fractal dimension turned out to be insensitive to curvature since the surface is locally flat at a small length scale. However, the manifolds structure altered the screening and tip-splitting of branches; as a result, the multifractal dimensions were shifted.

We believe that the research throughout this thesis made several important contributions to the study of interfacial growth phenomena and satisfied many of our initial motivations. At the same time, it opened up new questions to be pursued as future works.

Our model of transport-limited aggregation (TLA) is a significant generalization of DLA. We brought non-harmonic transport processes into the realm of the conformal mapping dynamics. By doing so, we simplified the simulation, yet utilizing the analytic tools of conformal mapping; as mentioned in Chap. 2, one can not think of any simpler ways of performing such growth simulations. Considering that the Hastings-Levitov algorithm is preferred over random walk simulation even at the cost of computational complexity, the efficiency of our generalization can not be underestimated. Moreover, the conformally invariant transport mechanisms in Eq. (2.1) are broad enough to model arbitrary phenomena with some simplifying assumptions as they can be incorporated in the combinations of various forms. As shown in the case of ADLA, the features manifested from the interplay among only two transport processes are already rich and complex. Our future work should be focused on developing other systems of TLA beyond our simplest example, ADLA.

The study of continuous transport-limited growth is a big open problem. The high-Pe asymptotic solution in advection-diffusion is an important discovery. But the exact solution at intermediate time is yet unknown. One can seek the extension of numerical methods [109] developed for Laplacian growth (with or without regularization) to our generalized models. The evolution of pole-like singularities under non-diffusive transport processes is a mathematically interesting question. A recent study on gravity currents in ambient flows in porous media [110] is a relevant case in which the continuous growth model and the corresponding numerical methods can be applied.

Our model also provided meaningful feedback to DLA. In simulating stochastic aggregates, we introduced two perturbations to DLA, i.e., advection and curvature, which caused

noticeable changes in the global morphology of aggregates such as anisotropy and instability respectively.

In both cases, the fractal dimension, $D_f \approx 1.71$, is surprisingly robust. We think it is because the effects of advection and curvature vanish in a small length-scale comparable to the particle size; thus, DLA dynamics is recovered in the scale. The ubiquity of DLA is important again. We further conjectured that D_f is universal if the the growth model have a steadystate growth probability measure $p_\infty(\theta)$. Albeit unphysical, it can be easily tested using arbitrary probability, $p_\infty(\theta)$. In regard to the controversy about multiscaling, one might check if the local fractal dimension of ADLA is angle-dependent.

The curvature, however, seems to affect the higher moments of the probability measure. The multifractal dimensions D_q on spheres seem to be transient, suffering from the finite space and the singularity at the north pole. Thus, more exact and larger simulations should follow. Nevertheless the correlation is consistent that D_q ($q \geq 2$) increases as the curvature increases from negative (hyperbolic) to zero (planar) and to positive (elliptic). The distribution of λ should be directly obtained and compared in the different geometries. It would be interesting to see how *a priori* predictions for D_q are adjusted on curved surfaces. In particular, the theory of branched growth [7, 51, 52, 53] looks to have some relevance in this regard. As Parisio et al. [67] suggested, the curvature could be used as a control parameter for the tip-splitting instability, probably useful for the theoretical approaches.

From our comparison of continuous and stochastic profiles in Secs. 3.3∼3.5, it is clear that the two dynamics are closely related in the mean-field approximation, but not identical. The fact that radial DLA (and viscous fingering) is the degenerate case of the approximation retrospectively tells us why the difference is subtle and has been controversial in the case. As mentioned in Sec. 3.5, Eqs. (3.40)∼(3.41) are necessary conditions relating $\langle G_\infty \rangle$ and $\langle G_\infty^{-2} \rangle$ but not a complete theory for $\langle G_\infty \rangle$. We notice an open possibility that our *ad hoc* argument Eq. (3.49) may close the relation; Eqs. (3.40), (3.47), and (3.49) may determine, at least qualitatively, the average cluster without going into the full statistics of the ensemble. The calculation will reduced to the systems of nonlinear equations for the Laurent coefficients. Thus, Eq. (3.49) should be verified thoroughly. A choice of artificial $p_\infty(\theta)$ will be used for this purpose as well. Above all, an immediate test is required for the case of DLA on a channel geometry.

Part II

Dense Granular Flow

Chapter 7

Introduction to Part II

Granular materials display a surprisingly complex range of properties which make them appear solid or liquid like depending on the applied conditions [111, 112]. Because the interaction between the grains is dissipative and the thermal energy scale is small compared with the energy required to move grains, such materials quickly come to rest unless external energy is supplied constantly. Although vibro-fluidization and tumbling [113] is frequently used to excite granular materials, flows driven purely by gravity can occur in nature as well. Typical granular flows are dense and a fundamental statistical theory is not available to describe their properties. One reason for this situation is the lack of quantitative data which can be used to test and develop models of dense granular flow. In this paper, we focus on flows inside silos and hoppers in order to elucidate the nature of the flow and to test existing models. Such systems are ubiquitous due to the need to store and process granular materials in devices ranging from simple hour glasses to sophisticated nuclear pebble reactors [114, 115].

Several aspects of granular drainage have been studied over the years. Beverloo et al. [116] thoroughly investigated the relation between the orifice size and the mass flow rate in cylindrical silos and proposed a formula describing the observed dependence. Using radiography, Baxter et al. [117] observed density waves in the hopper flow and showed various patterns of the wave depending on the particle roughness and the hopper angle.

The velocity field of the flow inside a silo has been described by two different approaches. One is based on the critical-state theory of soil mechanics which relates stress and density to predict velocity field or mass flow rate [118, 119]. Although this approach has the appeal

of starting from mechanical considerations, some questionable assumptions are made to resolve indeterminacy in the stress tensor, and the resulting equations are mathematically ill-posed and can lead to violent singularities [120, 121]. The solutions available for hoppers possess shock-like velocity discontinuities ("rupture zones") [119], which are not seen in our experiments (see below).

The second approach ignores the stress field and attempts a purely kinematic description of the velocity profile, starting from an empirical constitutive law. A theory of this type was first discussed by Litwiniszyn, who introduced a stochastic model in which particles perform random walks through available "cages" [122, 123, 124]. Later, Mullins independently proposed an equivalent stochastic model of the flow in terms of "voids" and extensively developed the continuum limit, where a diffusion equation arises [125, 126]. Decades later, Caram and Hong revisited the Void Model and implemented it explicitly in computer simulations on a triangular lattice (where the voids are simply crystal vacancies) [127].

As an alternative to the microscopic void picture, Nedderman and Tüzün derived the same continuum equation starting from a constitutive law relating horizontal velocity and downward velocity gradient [128, 129]. Regardless of its derivation, the Kinematic Model predicts velocity fields with only one free parameter. In light of its simplicity, early experiments on silo drainage were viewed as successes of the model [129, 130, 131], even though it has since fallen from favor in engineering [119]. Although the free parameter has been observed to be proportional to grain diameter in all experiments, the constants of proportionality do not agree [129, 130, 132]. Furthermore, Medina et al. [133] have reported that the kinematic parameter varies within a silo when the flow is analyzed in detail by particle image velocimetry.

In addition to the studies of the flow pattern, the diffusion of particles has been investigated as well. Hsiau and Hunt [134], Natarajan et al. [135] imaged tracer particles in a dense flow inside a vertical channel with various boundary wall condition to investigate the concept of "granular temperature". From an analysis of velocity fluctuations, they found that particles show normal diffusion and that the diffusivity in the stream wise direction is higher than in the transverse direction. Later, [136] used diffusing-wave spectroscopy to measure the dynamics of 100μm glass beads inside a three-dimensional flow with improved temporal resolution, albeit at rather small length scales. They reported that the particles show ballistic flight between collisions over a short time scale, and normal diffusion over

longer time scale, although the collision distance of 28 nm (1/10,000 of a grain diameter) could perhaps be associated with sliding or rotating asperities in frictional contacts. In any case, the randomizing gas-like collisions assumed in kinetic theories [137, 138, 139] have not been confirmed in any experiments on dense flows.

With rapid advances in high-speed digital imaging technology, it is now possible to simultaneously record thousands of individual particle positions. It seems to be opportune to use the advanced imaging technology to examine the theories for dense granular flow. In particular, with the improved resolution in both time and space, we are able to directly test the validity of the microscopic assumptions these theories are based on. Thus, we devote the rest of the thesis to this purpose. We also remark that this experimental research have been conducted in parallel with an effort to make a new consistent model for dense granular flow, which we will briefly introduce. The *Spot* model is discussed in detail elsewhere [140, 141, 142].

We first outline the experimental set-up and particle tracking algorithm in Chap. 8. In Chap. 9 the existing models for velocity profile are introduced and compared with experimental results. In Chap. 10 we investigate the diffusion and mixing properties of particles. Finally we summarize our result in Chap. 11.

Chapter 8

Experimental Procedure

8.1   Experimental Setup

Our experimental apparatus involves black glass beads ($d = 3.0 \pm 0.1$ mm) in a quasi-two dimensional silo with length $L = 20.0$ cm ($67d$) height $H = 90.0$ cm ($300d$), and thickness $D = 2.5$ cm ($8.3d$): See Fig. 8-1. The particles are observed near the front wall made of transparent glass. The slight polydispersity reduces the tendency for hexagonal packing to occur near the front wall. (As seen in Fig. 8-2, there is no long-range order, although the wall induces some short-range order that may affect our results.) The thickness of the silo D is large enough that finite-size effects are not significant. We obtained similar results for both mean velocity and diffusion when we increase D. Therefore, we report our data for a single thickness. A distributed filling procedure [143] was used to fill the silo with the grains. The orifice is opened and steady state flow is allowed to develop before acquiring the images used for determining particle positions.

For the measurement of mean velocity in Chap. 9, we view a rectangular region of 20.0×50.0 cm above the orifice with a resolution of 512×1280 pixels. Therefore, each particle diameter corresponds to $d = 7.7$ pixels. The images are acquired at a rate of 125 frames per second. The camera memory allows 2048 consecutive images to be stored at this resolution, and therefore the maximum interval over which we can track a particle is about 16.4 s.

For the funnels in the hopper, plexi-glass wedges are placed on top of the bottom plate. The surface property of wedge boundaries is identical to the side walls. We use wedges with three different angles, $\theta = 30°, 45°$ and $60°$. The orifice size $W = 18$ mm is fixed for the
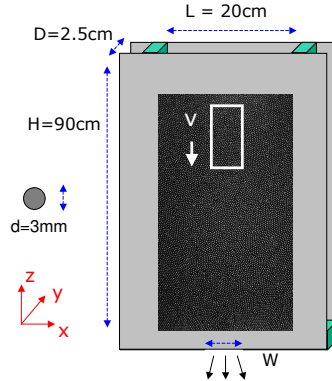
Figure 8-1: The quasi-two dimensional silo and the dimensions

hopper experiments while, it is varied with $W = 12, 16$ and $20\,$mm for the silo. To gain good statistics, three experiments are conducted for each funnel angle and orifice size.

For the measurement of diffusion in Chap. 10 (and flow rate dependence in Sec. 9.3), we focus on a narrow 5×25 cm $(17 \times 87\,d)$ region far above the orifice, the white box in Fig. 10-1(c). The purpose is to investigate particle dynamics in a region where the flow is almost uniform and to acquire a higher resolution. We imaged the area with 256×1280 pixels $(d = 15$ pixels$)$ at a rate of 1000 frames per second. At this combination, 4096 consecutive images (4.1 s) can be stored. The mean velocity v, which is nearly constant in this window, is controled by the orifice width W. We vary W in the range of 8 mm $\leq W \leq$ 32 mm, in increments of 4 mm. We compile statistics from all tracked particles in six experiments per flow speed (except two for $W = 32$mm) and only use flat-bottomed silo.

8.2 Particle Tracking

To identify the locations of particles from images, we employ the algorithm proposed by Crocker and Grier [144]. In this algorithm, the raw images are preprocessed to reduce
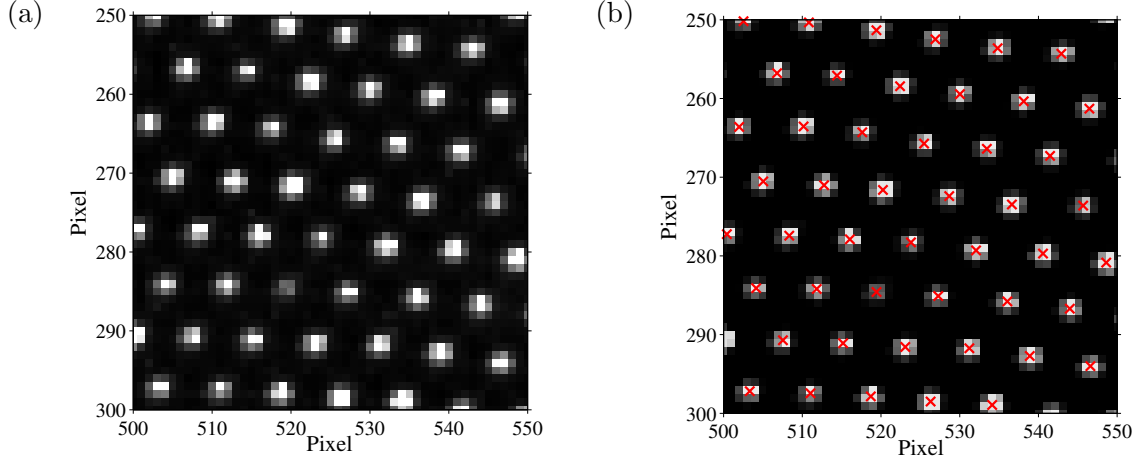
Figure 8-2: (a) A raw image of the glass beads acquired with the high-speed camera, and (b) the preprocessed image along with the position of the centroid of the identified particle (×).

the noise and the background. This involves convolving the image with a Gaussian filter and then an average filter of roughly d pixels respectively. The particle location is then identified with the centroid around the local maximum brightness pixel in the modified image. To optimize the particle tracking for our experiment, the algorithm was also further customized. Because the glass beads are circular, we use circular shaped filter. We also set an intensity cutoff to discard the blur images of particles located deep away from the front wall. A sample of an image before and after the processing is shown in Fig. 8-2. The position of the located particles is also superposed. When the algorithm is tested on the stationary particles in the silo drianage experiment, the fluctuation of particle positions about $0.003\,d$.

After particles are located frame by frame, their trajectories should be retrieved by "connecting" their positions in time. We associate a particle in a frame with another in the next frame which is within a radius of $0.66\,d$ pixels around the original position. This simple method works well avoiding more complicated multiple associations except very near the orifice where the particles move more than $0.66\,d$ pixels per frame. The particles can be tracked there by using a faster frame rate, but we do not do so here since bulk flow, and not orifice dynamics, is the focus of our study.

Chapter 9

Velocity Profile Inside Silos and Hoppers

9.1 Models for the Mean Velocity Profiles

A simple kinematic description of the mean velocity profile in silos and hoppers has been developed since the 1950s, from a variety of theoretical perspectives [119]. The continuum Kinematic Model starts from an empirical constitutive law relating velocity components [128], which can be derived as a continuum limit of the (earlier) Void Model [122, 125]. The latter is a more complete theory, because it provides a microscopic mechanism for flow, which can be checked by experiments on diffusion and mixing. Recent experiments, however, have firmly rejected the void hypothesis. On the other hand, an alternative stochastic description, the Spot Model [140, 141], which starts from a cooperative mechanism for random-packing rearrangements, roughly preserves the mean flow profile of the Kinematic Model, with much less diffusion and slow cage breaking, consistent with experiments in Chap. 10.

9.1.1 The Kinematic Model

Nedderman and Tüzün [128], Tüzün and Nedderman [129] proposed a model based on the following constitutive law relating velocity components:

$$u = b\frac{\partial v}{\partial x}, \tag{9.1}$$

which states that the horizontal velocity u, is proportional to the horizontal gradient (i.e. the shear rate) of the downward velocity v. This assumption is based on the fact that particles tend to drift horizontally towards a region of faster downward flow as they are likely to find more space to move in that direction. Assuming that the density fluctuation is small in dense granular regimes, they combined Eq. (9.1) with the incompressibility condition,

$$\frac{\partial u}{\partial x} - \frac{\partial v}{\partial z} = 0, \tag{9.2}$$

and obtained an equation for the downward velocity,

$$\frac{\partial v}{\partial z} = b \frac{\partial^2 v}{\partial x^2}. \tag{9.3}$$

Eq. (9.3) has a form of the diffusion equation, where time is replaced by the vertical coordinate z. When an "initial condition" is given for v at the bottom of the silo at $z = 0$, the velocity diffuses upward. The boundary condition assumed at the side walls of the silo is that the velocity is parallel to the wall. Although the authors did not discuss this situation, the condition can be naturally generalized to the case where the side walls are not vertical. It is written as

$$u\,n_x - v\,n_z = 0 \quad \text{at} \quad (x, z) \quad \text{on the side wall}, \tag{9.4}$$

where (n_x, n_z) is the normal vector at the boundary.

For a semi-infinite quasi-two dimensional system $(-\infty < x < \infty)$ with a point-like orifice at $z = 0$ which acts as a source of velocity, a similarity solution exists:

$$v(x, z) = \frac{Q}{\sqrt{4\pi bz}} \, e^{-x^2/4bz}, \tag{9.5}$$

where, Q is the flow rate per unit thickness of the silo. We refer to the constant of proportionality b in Eq. (9.1), as the "diffusion length," as it is has units of length. We provide microscopic understanding of b in Sec. 9.1.2.

The Kinematic Model has been tested experimentally, and the parameter, b has been measured by various groups. Tüzün and Nedderman [129] observed $b \approx 2.24d$ for various particle size. Experiments by Mullins [130] with monodisperse iron ore particles imply $b \approx 2d$. Medina et al. [133] used the particle image velocimetry (PIV) technique to obtain the velocity field and found that the diffusion length increases from $b \approx 1.5d$ to $b \approx 4d$ as the

height increases to fit the field. Samadani et al. [132] reported $b \approx 3.5d$ for monodisperse glass beads using difference imaging to find velocity contours. All the groups claimed that the prediction of the Kinematic Model qualitatively agree with their experiment. The fact that a single fitting parameter b suffices to reproduce the entire flow field should be viewed as a major success of the Kinematic Model.

In order to test the Kinematic Model more thoroughly, we use numerical methods to solve the Kinematic Model subject to the same dimensions used in our experiments. For this purpose, we define the stream function, $\psi(x, z) = \int_0^x v(s, z)ds$ and solve for $\psi(x, v)$ rather than $v(x, z)$. Formulated in terms of ψ, the boundary condition turns into a Dirichlet one from a rather complicated one given by Eq. (9.4). Furthermore, it is more convenient for the hopper geometry with inclined boundaries. If the width of the system is given by $L(z)$ and the silo is symmetric about its center [e.g. $-L(z)/2 \leq x \leq L(z)/2$], the equation and the boundary condition for ψ is given by

$$\frac{\partial \psi}{\partial z} = b\frac{\partial^2 \psi}{\partial x^2} \quad \text{and} \quad \psi(0, z) = 0, \quad \psi\left(\pm\frac{L(z)}{2}, z\right) = \pm\frac{Q}{2}. \tag{9.6}$$

We numerically integrate Eq. (9.6) from $z = 0$ using the Crank-Nicholson method to obtain the prediction of the Kinematic Model.

Due to its continuum formulation, the Kinematic Model cannot predict grain-level diffusion and mixing, so we now turn to statistical kinematic models for the velocity profile, which postulate mechanisms for random-packing dynamics.

9.1.2 The Void Model

Since Eq. (9.3) has the form of a diffusion equation, where the vertical distance z plays the role of "time," it is clear that any microscopic justification for the Kinematic Model should be based on independent random walks. In fact, this is how the model was first derived decades earlier, based on statistical considerations. Although the continuum approach is more general, in the sense that it is not tied to any specific microscopic mechanism, it lacks a clear physical basis, so it is important to consider what kind of microscopic mechanisms might support it.

Litwiniszyn first suggested the idea that particles are confined to a fixed array of hypothetical "cages" as they perform random walk from one available cage to another during

117

drainage [122, 123, 124]. Then, Mullins [125, 126] independently proposed an equivalent model in terms of "voids" rather than particles, which is analogous to vacancy diffusion in crystals. In his model, particles move passively downward in response to the passage of voids, and the voids take directed random walks upward after emerging from the orifice.

Assuming that voids diffuse by non-interacting random walks, it is straightforward to show that in continuum limit, at scales larger than the grain diameter, the concentration (or probability density) of voids, ρ_v, satisfies the diffusion equation,

$$\frac{\partial \rho_v}{\partial z} = b \frac{\partial^2 \rho_v}{\partial x^2}. \tag{9.7}$$

Since the downward velocity v is proportional to the frequency of the void passage, this implies Eq. (9.3) of the Kinematic Model. However, the equivalence of the two model assumes that voids can be superimposed without interaction.

The void model also gives us an interpretation for the kinematic parameter, b. If a void undergoes a random horizontal displacement, Δx_v, while it climbs up by Δz_v, the parameter b is given by

$$b = \frac{\mathrm{Var}(\Delta x_v)}{2 \Delta z_v}, \tag{9.8}$$

which is the characteristic length of the void diffusion. However it is very difficult to determine b directly from Eq. (9.8). Δx_v and Δz_v cannot be measured from an experiment, nor does any *a priori* choice produce the measured value of b. Mullins also deduced $b \approx 2d$ from the velocity profile for round particles ($b \approx d/4$ for irregular particles) without specifying the value of Δx_v and Δz_v. By contrast, Caram and Hong [127] assume a void makes an one-to-one exchange with particles on a regular lattice when they later revisited the void model. It is noteworthy that any regular lattice of hard sphere packing under predicts b ($b \ll d$) [140].

The void model faces more serious problems when it is used to predict diffusion and mixing, which was not done by its proponents. If a tracer particle is placed in a uniform flow driven by voids, the particle does a directed random walk downward with precisely the same diffusion length as the voids moving up. Thus particles are easily mixed before they drop by a few particle diameters, which goes against our everyday experience and our experiments in Chap. 10.

9.1.3 The Spot Model

To address these contradictions, Bazant et al. [140], Bazant [141] proposed the Spot Model, which starts from a mechanism for cooperative diffusion in a dense random packing. It has roughly the same mean flow as in the kinematic model, because it also assumes that particles move in response to upward diffusing free volume, but this excess volume is carried in extended "spots" of slightly enhanced interstitial volume, not in voids.

The kinematic parameter, b, is now set by the diffusion length for spots,

$$b = \frac{\text{Var}(\Delta x_s)}{2\Delta z_s},$$ (9.9)

where, Δx_s and Δz_s are spot displacements in x and z directions, respectively. Unlike a void which is a vacancy capable of being filled by an entire particle, however, a spot carries small fraction of interstitial space spread across an extended region and causes all affected particle to move (on average) as a block with the same displacement in the opposite direction to the spot.

Of course, there are more complicated internal rearrangements, which can be taken into account to achieve accurate spot-based simulations [142], but the simplest mathematical model already captures many essential features of dense drainage [140, 141]. For example, it is easy to see that the spot mechanism greatly reduces the diffusion length of particles, compared to the diffusion length of free volume. Suppose that a spot carries a total free volume V_s, and causes equal displacements (Δx_p, Δz_p), among N_p particles of volume V_p. The particle displacement can be related to the spot displacement (Δx_s, Δz_s) by an approximate expression of total volume conservation,

$$N_s V_p(\Delta x_p, \ \Delta z_p) = -V_s(\Delta x_s, \ \Delta z_s),$$ (9.10)

which ignores boundary effects at the edge of the spot. From this relation, we can compute the particle diffusion length,

$$b_p = \frac{\text{Var}(\Delta x_p)}{2\Delta z_p} = \frac{w^2 \text{Var}(\Delta x_s)}{2w\Delta z_s} = wb$$ (9.11)

which is smaller than the spot diffusion length b by a factor, $w = V_s/N_p V_p$. This can in turn be related to the change, $\Delta\phi$, in local volume fraction, ϕ, caused by the presence of

119
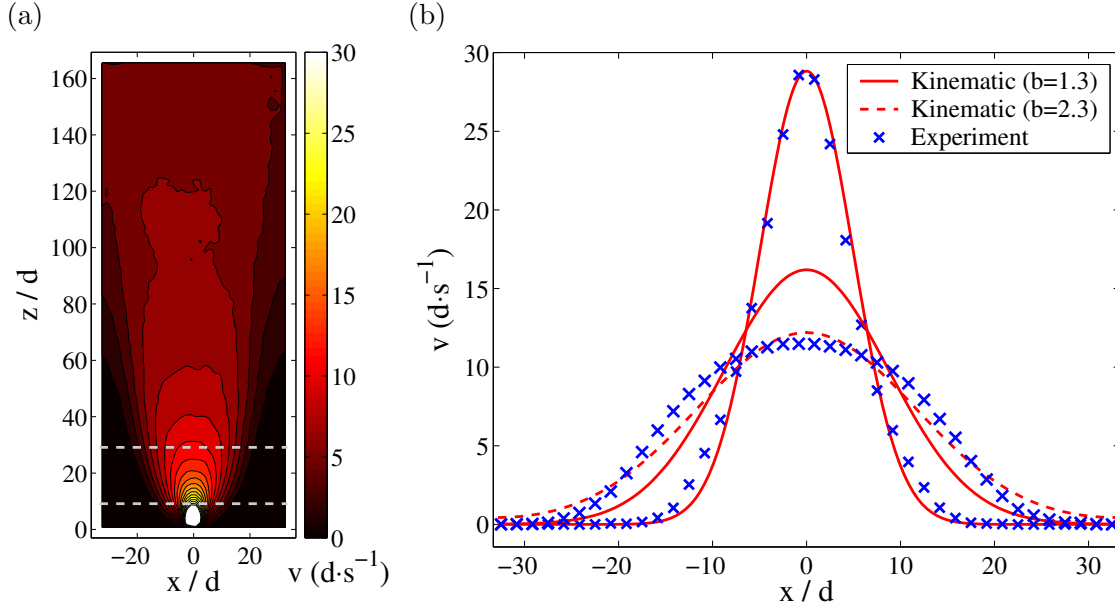
Figure 9-1: (a) Contour plot of the average downward velocity field, v in a flat-bottomed silo with an orifice width, $W = 16\,\text{mm}$. (b) v as a function of x at the two heights, $z_1 = 9.1d$ and $z_2 = 29.1d$ indicated with gray dotted lines in (a). The result from the Kinematic Model in the same geometry fits best with $b = 1.3d$ for the z_1 profile, and $b = 2.3d$ for the z_2 profile. The result from the model for the z_2 profile with b fitted at z_1 (narrow solid curve) is also shown.

the spot,

$$w = \frac{b_p}{b} = \frac{V_s}{N_p V_p} \approx \frac{\Delta\phi^2}{\phi} \tag{9.12}$$

It is well known from simulations and experiments that the volume fraction fluctuates on the order of 1% in a dense flow, so the Spot Model thus predicts $w = b_p/b = O(10^{-2})$. (In our experiments, the local area fraction of glass beads near the viewing wall varies by less than three percent.) The estimate of w is further reduced by noting that spots occur in large numbers and overlap, so that each spot contributes only a small part of the change in local volume fraction. We will test this prediction in our experiments in Chap. 10.

9.2 Comparison of Experiment Results with the Kinematic Model

We first compare the data from the flat-bottom silo with the model. Fig. 9-1(a) shows the contour plot of the average downward velocity v. The mean velocity is obtained by dividing the observation window into square cells of size $1.6d \times 1.6d$. Then in each cell, the average

120
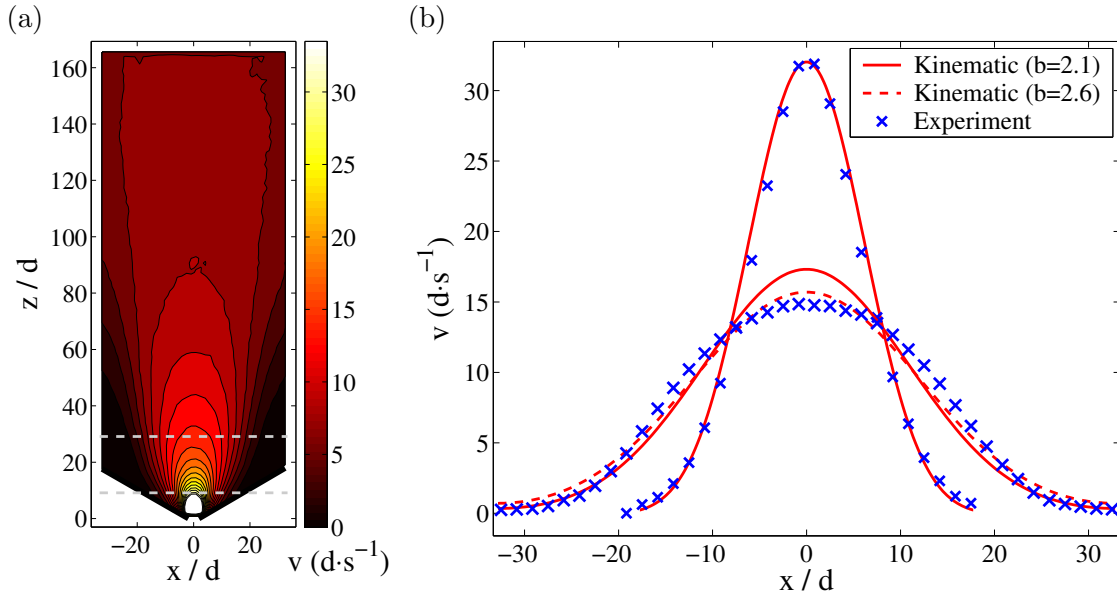
Figure 9-2: (a) Contour plot of the average downward velocity field, v in a hopper with angle, $\theta = 30°$, and $W = 18\,\text{mm}$. (b) v as a function of x at the two heights, $z_1 = 9.1d$ and $z_2 = 29.1d$ indicated with gray dotted lines in (a). The result from the Kinematic Model fits best with $b = 2.1d$ for the z_1 profile and $b = 2.6d$ for the z_2 profile. The result from the model for the z_2 profile with b fitted at z_1 (narrow solid curve) is also shown.
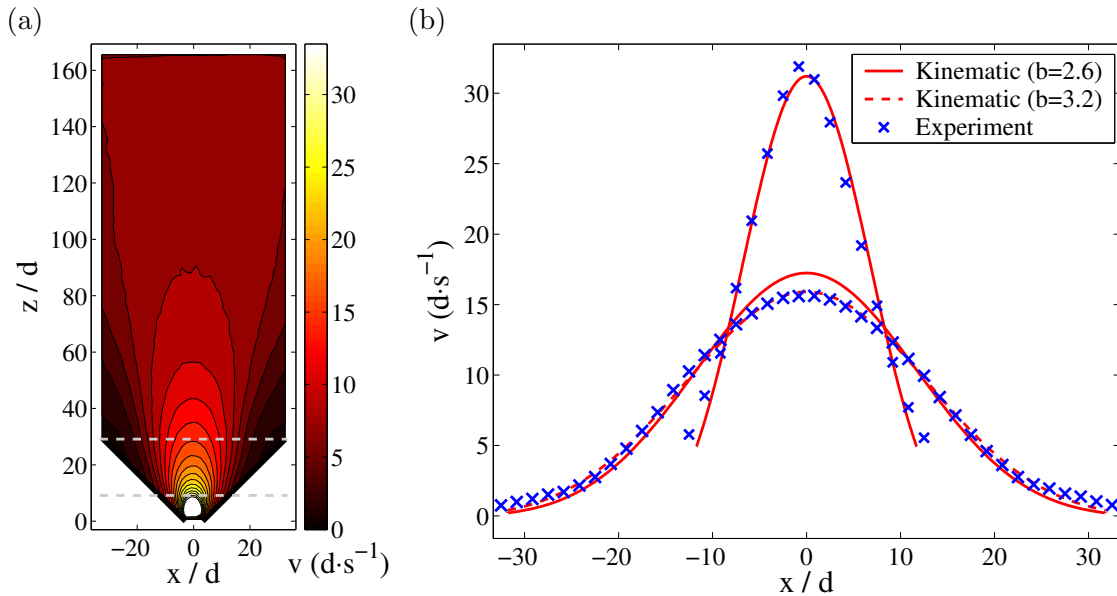
Figure 9-3: (a) Contour plot of the average downward velocity field, v in a hopper with angle, $\theta = 45°$, and $W = 18\,\text{mm}$. (b) v as a function of x at the two heights, $z_1 = 9.1d$ and $z_2 = 29.1d$ indicated with gray dotted lines in (a). The result from the Kinematic Model fits best with $b = 2.1d$ for the z_1 profile and $b = 2.6d$ for the z_2 profile. The result from the model for the z_2 profile with b fitted at z_1 (narrow solid curve) is also shown.

121
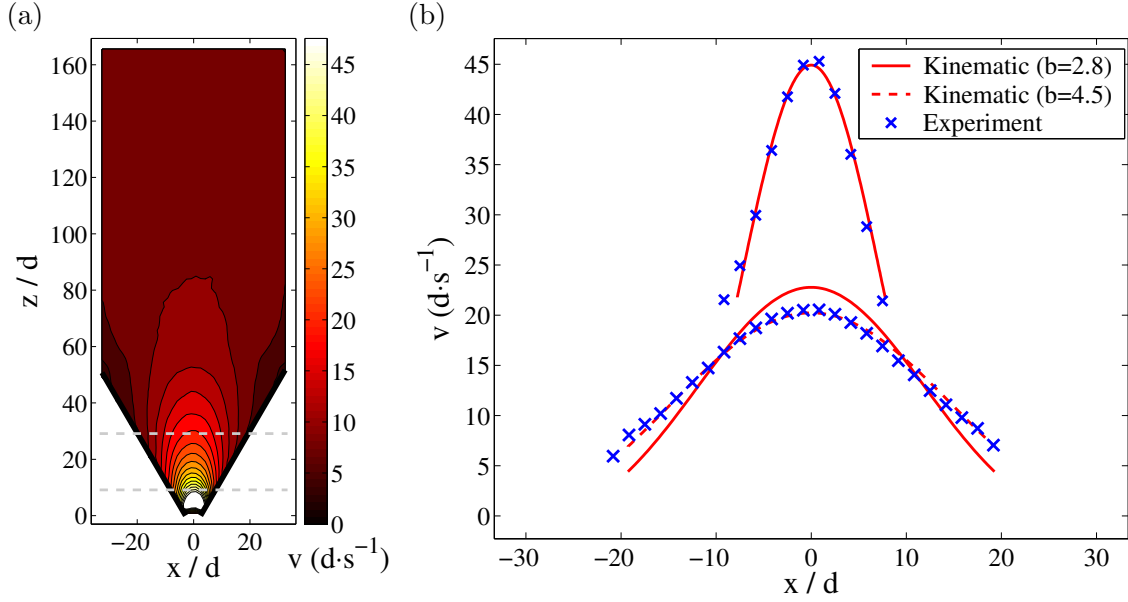
Figure 9-4: (a) Contour plot of the average downward velocity field, v in a hopper with angle, $\theta = 60°$, and $W = 18\,\text{mm}$. (b) v as a function of x at the two heights, $z_1 = 9.1d$ and $z_2 = 29.1d$ indicated as gray dotted lines in (a). The result from the Kinematic Model fits best with $b = 2.6d$ for the z_1 profile and $b = 3.2d$ for the z_2 profile. The result from the model for the z_2 profile with b fitted at z_1 (narrow solid curve) is also shown.

is performed over the displacements of all the particles passing through the cell. We again take the average of the field from three experiments. The data across experiments shows little variation, which confirms that the velocity field is well-defined and stationary. Thus we do not show the error bar in the plots of this paper unless the concerned quantity has visible fluctuations.

The contour plot shows that v is maximum right at the orifice and appears to "diffuse" upward, in qualitative agreement with the models discussed above. The regions in the left and right corner made by the side walls and the bottom plate remain stagnant, and the boundary of mobile region has a parabolic shape. In Fig. 9-1(b), we show the profiles $v(x)$ at two cross sections $z_1 = 9.1d$ and $z_2 = 29.1d$ [dotted lines in Fig. 9-1(a)] with the fit to the Kinematic Model. The diffusion length, $b = 1.3d$ was the best fit for the profile at z_1. However, b becomes larger when z increases as some previous reports have also reported [119, 133]. The profile at z_2 is best fit with $b = 2.3d$, but it has a flattened shape at center with thinner tail indicating further obvious deviations from the model.

The velocity profiles from the experiments with different orifice width turn out to co-incide when they are normalized by the flowrate as is commonly observed in other dense

granular flows [145]. Thus the best fitting value of b is independent of the flowrate. The dependence of the flowrate on the orifice width willl be discussed in the next subsection.

We performed similar analysis of the experiments with the hoppers. The contour plots along with the profiles at $z = z_1$, z_2 for the angles, $30°, 45°$ and $60°$ are presented in Figs. 9-2, 9-3, and 9-4 respectively. As angle is increased, the stagnant region is diminished as the particles slip on the wedge. At z_1, the critical angle over which slip occurs is between $30°$ and $45°$ and at z_2, it is between $45°$ and $60°$. However the shape of equi-velocity contours well above the funnel is not affected significantly by the funnel's detailed shape.

The value of b to obtain the best fit depends on the angle of the hopper as well. It increases from $2.1d$ to $2.8d$ for z_1, and from $2.6d$ to $4.5d$ for z_2 as the angle is increased.

Although we observe some quantitative discrepancies with the simple Kinematic Model with a constant coefficient, b, the flow is at least qualitatively consistent. This appears not to be the case with continuum models from critical-state soil mechanics [119], which generally predict sharp, shock-like discontinuities in velocity (and stress, which we do not measure) within the silo, especially near corners. We see no such abrupt jumps in velocity in the silo, only rather smooth velocity profiles.

9.3 Flow Rate Dependence on the Orifice Size and the Funnel Angle

The mass flow rate in a silo during discharge was an important subject of early research. Using drainage experiments in cylindrical silos with a circular orifice, Beverloo et al. [116] reported a relation known as the Beverloo correlation

$$Q \propto \rho\sqrt{g}\,(W - kd)^{2.5}, \quad k = 1.4 \tag{9.13}$$

where Q is the mass flow rate, ρ is the bulk density of packing, g is the gravitational constant and W is the diameter of orifice. It is usually argued that $Q \propto \rho\sqrt{g}\,(W - d)^{2.5}$ is the only form which can be deduced from the dimensional analysis as $(W - d)$ is the effective diameter (or width) where particle centers can be placed within the orifice, but arching and other effects could also introduce the particle diameter d and thus another dimensionless parameter, d/W. Instead, the Beverloo correlation includes a somewhat controversial factor
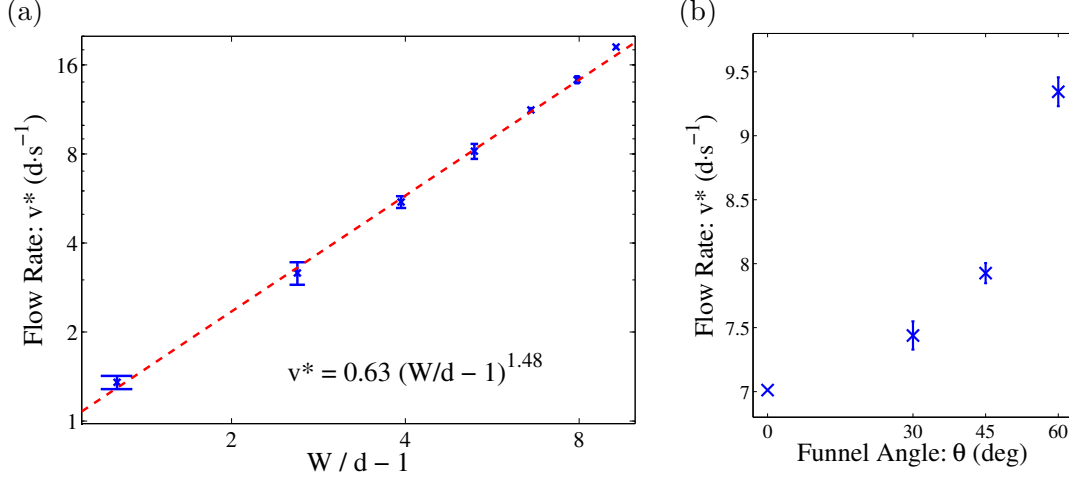
Figure 9-5: The dependence of the flow rate on (a) the effective orifice width, $W/d-1$ in a flat-bottomed silo (log-log scale), and (b) the funnel angle θ in a hopper with a fixed orifice width. The flow rate is measured averaging the downward velocity in the plug-flow region. The fitting of (a) validates the result of a dimensional analysis, $Q \propto (W-d)^{1.5}$.

$W-kd$, where the empirical factor k is claimed to derive from the region near the orifice rim which obstructs the passage of particles. This picture could be consistent with the concept of an "empty annulus" proposed by Brown and Richards [146].

For a *slit* orifice with a quasi-two-dimensional silo as in our experiment, the dependence can be obtained to be

$$Q \propto \rho\sqrt{g}\,(D-d)\,(W-kd)^{1.5}, \tag{9.14}$$

because the flow rate is linear with system depth $D-d$ [1]. We investigated the flow rate dependence on orifice width using our data. Although the discharged mass flux is not directly measured, we use the overall average velocity, $v^* = Q/L$ to obtain the flow rate.

Fig. 9-5(a) shows the relation between the flow rate and orifice size in log-log scale. When $k=1$, the data fits to a power law scaling with an exponent of 1.48. Although $k=0.94$ gives the exact exponent of 1.5, we do not attach much importance to the deviation as our flow rate measure is indirect. However, it is sufficient to check that the Beverloo correlation (dimensional analysis) holds in a 2-D silo.

We also investigated how the funnel angle affects the flow rate. In order to compare the rate at a fixed orifice width, we interpolate the rate with $W = 18\,\text{mm}$ from data with

---

[1] It should be noted that the orifice in our system is entirely open from front to back surface. Thus the "empty annulus" argument is difficult to apply in the direction of silo depth. We cannot find the exact dependence on D because we fix $D = 2.5\,\text{cm}$.
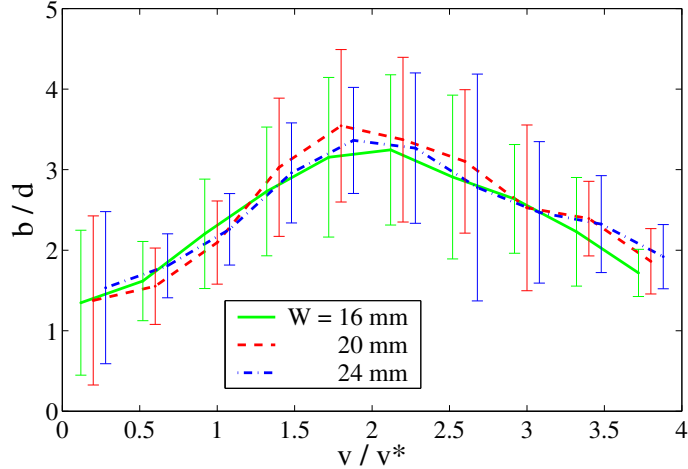
Figure 9-6: The locally measured diffusion length, b as a function of the normalized velocity, v/v^*.

$W = 16$, 20 and 24 mm for the silo experiment. Fig. 9-5(b) shows a consistent increase in the flow rate as the angle increases. The flow rate in the 60° funnel turns out to be about 33% more than that in the flat-bottom silo. This dependence is consistent with the data from Tüzün and Nedderman [147], although the reported increase of the flow rate is smaller than our data. We believe the increased flow rate largely comes from the fact that the smooth rigid boundary facilitates the passage of particles. As seen clearly from Figs. 9-1(b)∼9-4(b), the stagnant zone present in the corners of flat-bottom silo gets replaced by wedges. Thus the slip velocity at the boundary increases as the angles increases, which make the out-going flow at the orifice ($z = 0$) more uniform and shear-free. This effect appears to allow the particles to exit the orifice more easily.

9.4   Validity of the Kinematic Model

In Sec. 9.2, we observed that the Kinematic Model with a constant parameter b is not consistent with the experiments. It was found that b depends on the height and the funnel angle. In this section, we investigate the validity of two important assumptions of the Kinematic Model, namely the constitutive law Eq. (9.1), and the generalized boundary condition Eq. (9.4) for the funnel geometry.

First, we directly check the constitutive law Eq. (9.1) using the results from our experiments. In each cell that was used for averaging the velocity, we measure the horizontal

velocity u, the downward velocity gradient $\partial v/\partial x$, and therefore the diffusion length b. Fig. 9-6 shows the distribution of the locally measured values of b. As expected, it shows a wide fluctuation scattered from $b = d$ to $b = 3d$. When b is associated with v, we find b increases upto $3.4d$ and decrease as v increases. In other words, we observe higher b moving away from the stagnant zone and towards the fast flow regions at the center. However, for the fastest-flow regions close to the orifice, b decreases. A reasonable implication of the increase in b is that the slightly lower density in the fast-flow region due to dilation makes horizontal movements easier. The decrease in b at higher v is perhaps related to the fact that particles undergo collisional flow in the fast flowing regions near the orifice. Since the particles are less locked to neighbors than in the dense bulk away from the orifice, the shear in the downward velocity result in less horizontal movement, therefore, smaller b.

A few further comments about Fig. 9-6 are in order. To collect meaningful statistics for b, we ignore shear-free zones (e.g. stagnant zone and plug-flow regions where the gradient of v is negligible), where b is likely to have large errors. We accomplish this by only considering cells where gradient is larger than 5% of the characteristic magnitude, v^*/d, where v^* is overall average velocity in the plug region. Although we only discuss b for the silo experiments in Fig. 9-6, a similar trend is also found for the hoppers as well.

The correlation between v and b gives some clues to explain the discrepancies in Sec. 9.2. The Kinematic Model with constant b fails to capture the development of a more plug-like plateau in the velocity profile even with larger values of b. However, if higher b is applied to the region around the center (where v is high), and lower b is applied to the region close to walls (where v is low), the model would come into closer agreement with experiment.

In an effort to understand the universality of this pattern, we use the overall average velocity, v^*, to normalize the downward velocity, v, from different flow rates (or orifice size). As shown in Fig. 9-6, pairs of $(v/v^*, b)$ for three different flow rates fall into nearly the same pattern. This is a consistent with the trends we observe in Chap. 10 that increasing the flow rate merely *fast-forwards* the entire dynamics, without changing the geometrical sequence of events.

Our way to describe our experimental results *a posteriori* is via a modified constitutive law with a variable diffusion length, b, which depends on the (scaled) local velocity:

$$u = b\frac{\partial v}{\partial x} \quad \text{and} \quad b = b^* \Phi\left(\frac{v}{v^*}\right), \tag{9.15}$$

where b^* is an effective diffusion length and Φ is a dimensionless scaling function. Note that the velocity field satisfying Eq. (9.15) is still linear with respect to rescaling the total magnitude of the velocity (by changing the total flow rate) since v/v^* is invariant when v is rescaled. However, the velocity profile in space is governed by a nonlinear diffusion equation,

$$\frac{\partial v}{\partial z} = b^* \frac{\partial}{\partial x} \left[\Phi \left(\frac{v}{v^*} \right) \frac{\partial v}{\partial x} \right] \tag{9.16}$$

It is well known that spreading solutions to this equation (analogous to a concentration-dependent diffusivity) are flatter in the central region (compared to a Gaussian) when Φ is an increasing function of its argument [148].

We should consider what might be the microscopic reason for a nonlinear diffusion length in the Kinematic Model. In general, it would arise from interactions between different spots, which are neglected as a first approximation. It makes sense that spots of free volume should diffuse less when they find themselves in a more slowly flowing, less dense, region, with fewer other nearby spots. This could explain why b appears to grow with velocity (or spot concentration). On the other hand, the flow in the upper part of the silo becomes more plug-like should exhibit less diffusion than the lower region of greater shear near the orifice, so it remains unclear whether the nonlinear model Eq. (9.15) can be given a firm microscopic justification. Further comparison with theory and experiment is needed to settle this question.

The next issue to test is the boundary condition at the side walls. Specifically, it is important to test if the model can be simply extended from open silos to hoppers by using Eq. (9.4). It is interesting to note that the curvature of the profile at $z = z_1$ around $x = 0$ remains the same for the different funnel angles [see Figs. 9-1(b)~9-4(b)]. In fact, it is b that should increase from $b = 1.3d$ to $b = 2.8d$ in order to reproduce the same curvature as the hopper angle is increased. For a more quantitative argument, we show in Fig. 9-7 the variance of the downward velocity profile (a measure of its squared width),

$$\langle x^2 \rangle_v = \frac{\int x^2 \, v(x) dx}{\int v(x) dx} \tag{9.17}$$

as a function of height, z. From Eq. (9.9), the slope of the linear regime near the orifice is equal to $2b$, and the value of the implied b does not significantly vary from $b = 1.9d$ for the silo, as can be seen in the inset to Fig. 9-7.
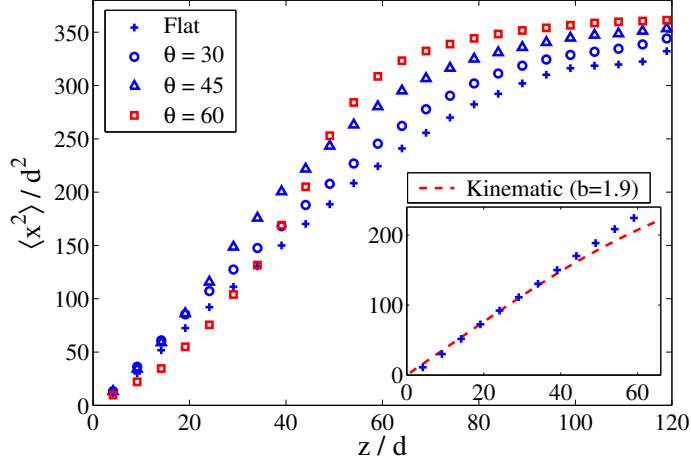
Figure 9-7: The variance (squared effective width) of the downward velocity profile, $\langle x^2 \rangle_v$, as a function of the vertical coordinate, z for different funnel angles.

We conclude, therefore, that extending the Kinematic Model to a hopper with non-vertical walls does not seem to be successful with the naive idea of Eq. (9.4), which assumes the same bulk constitutive law holds all the way to the boundary.

It may be that a nonlinear constitutive law as in Eq. (9.15) can improve the situation because particles slip more on a funnel wall and b thus tends to be higher than in the silo. However, there may still be problems higher in the tank where the flowing region meets the vertical side walls. The boundary condition Eq. (9.4) requires that the strain rate (horizontal gradient of vertical velocity) vanishes at a vertical wall, and yet small velocity gradients are observed near the walls in the upper region in Figs. 9-1~9-4. We plan to compare the nonlinear Kinematic Model, as well as other continuum models from critical-state mechanics and hourglass theory, more closely with the experimental flow profiles in future work.

Chapter 10

Diffusion and Mixing

Granular flow is an attractively simple and yet surprisingly complex subject [112]. Fast, dilute flows are known to obey classical hydrodynamics (with inelastic collisions), but slow, dense flows pose a considerable challenge to theorists, due to many-body interactions and non-thermal fluctuations. Beyond their fundamental scientific interest, such flows have important engineering applications [113], e.g. to new pebble-bed nuclear reactors [114], whose efficiency and safety depend on the degree of mixing in very slow granular drainage (< 1 pebble/min).

Although dense granular drainage is very familiar (e.g. sand in an hourglass), it is far from fully understood. Over the past forty years, a number of theoretical approaches have been proposed for steady state flow [124, 125, 128, 118, 119]. Continuum approaches are based on the critical-state theory of soil mechanics and yield only mean velocity fields [118, 119]. On the other hand, the diffusing void model [124, 125] takes a particle approach, in which "voids" injected at the orifice cause drainage by diffusing upward and exchanging position with particles along the way. Averaging over the void trajectories yields the same continuum velocity field for particles as the "kinematic model" [128, 119], which provides a reasonable fit to experimental data with only one fitting parameter (the diffusion length, b) [125, 130, 128, 132], although the void model on a regular lattice (as in Caram and Hong [127]) underpredicts its value [140]. Remarkably, these models depend only on *geometry* and not on momentum, energy, etc.

In spite of the success of the kinematic model, however, its only microscopic basis, the void model, greatly overpredicts diffusion. To see this, consider the Péclet number,
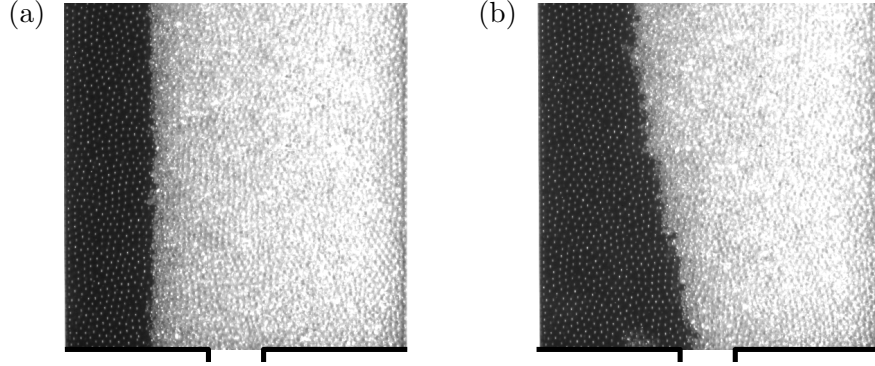
Figure 10-1: An initially flat, off-center interface between two regions of differently colored beads (a) stretches and roughens after draining half of the silo (b), but little mixing is observed.

$Pe_x = vd/D_x$, the dimensionless ratio of advection in uniform downward flow of speed, v, to diffusion with a horizontal diffusivity, D_x, at the scale of a particle diameter, d. In the void model, when a particle falls a distance $-\Delta z$,

$$Pe_x = \frac{(-\Delta z/\Delta t)\, d}{\langle \Delta x^2 \rangle / 2\Delta t} = \frac{-\Delta z\, 2d}{\langle \Delta x^2 \rangle},$$ (10.1)

is of order one for any conceivable packing since $-\Delta z \approx \Delta x \approx d$, and therefore it diffuses horizontally by roughly $\sqrt{-\Delta z}$. This prediction is contradicted by everyday experience and our experiments below, which exhibit far less mixing. An attempt to resolve this paradox with a new model appears in a companion paper [140].

In this Letter, we describe particle-tracking experiments on silo drainage using similar techniques as in a recent (lower-resolution) study of the velocity field [133]. We focus on the statistical evolution of particle displacements and topological "cages," which should aid in developing new microscopic models. Our data may also have implications for recent attempts to apply thermodynamic approaches from glassy dynamics to granular flows [149, 150, 151]. Although we do not define a "granular temperature," we observe the presumably related effect of varying the flow rate in all of our measurements.

10.1   Diffusion in an Uniform Flow

We first provides a visual demonstration that particles mix much less than predicted by the void model. We load the silo with black and white (but otherwise identical) glass beads, forming two separate columns, as shown Fig. 10-1(a). From Fig. 10-1(b), where half of the

particles have drained (in 30 sec), it is clear that the black-white interface has not smeared significantly, although it has roughened. The small degree of mixing is consistent with the segregation of bi-disperse beads in a similar apparatus [132].

For a quantitative analysis, we use high-speed imaging and particle tracking. In order to investigate particle dynamics in an uniform flow, we focus on a small $17 \times 87\ d$ region 50cm above the orifice, the white box in Fig. 8-1. The average flow speed v, the only control parameter in this study, is varied by changing the width of the orifice, W. The flow is fairly smooth for $W \geq 8$ mm (about $3d$) and nearly continuous for $W \geq 16$ mm. For simplicity, we vary W in the range 8 mm $\leq W \leq 32$ mm, in increments of 4 mm, to avoid the complicated regime of intermittent flow [152]. This corresponds to 1.38 $d/\sec \leq v \leq 18.39\ d/\sec$.

From the positions of the particles sampled at 1 ms intervals, we calculate the horizontal and vertical displacements, Δx and Δz, relative to a frame moving with the mean speed of the flow,

$$\Delta x = \Delta x(t + \Delta t) - x(t) - u\Delta t \qquad \text{and} \qquad \Delta z = \Delta z(t + \Delta t) - z(t) + v\Delta t, \qquad (10.2)$$

where Δt is the time gap between two consecutive frames (or integer multiples of it), and $x(t)$ and $z(t)$ are the coordinates of the particle in x and z axis respectively A typical trajectory computed in this way in Fig. 10-2(a) shows periods of small fluctuations with occasional, much larger steps. This suggests that the probability density functions (PDFs) for Δx and Δz (for $\Delta t = 1$ ms) should have fat tails compared to a Gaussian, which is confirmed in Fig. 10-2(b)$\sim$(c).

Fat-tailed PDFs have also been observed in colloidal glasses and attributed to cage-breaking [153], but a special feature here is the asymmetry of the PDF for Δz in Fig. 10-2(c). Downward fluctuations ($\Delta z < 0$) are larger than upward ($\Delta z > 0$) and horizontal (Δx) fluctuations. We attribute this to the fact that particles are accelerated downward by gravity while being scattered in other directions by dissipative interactions with neighbors.

Looking again at Fig. 10-2(a), it seems that the large fluctuations in particle displacements would be reduced by coarse-graining in time, perhaps enough to recover standard Gaussian statistics. Indeed, as shown in Fig. 10-2(d), the normalized kurtosis, $\kappa_x = \langle \Delta x^4 \rangle / 3 \langle \Delta x^2 \rangle^2 - 1$, which measures how much the shape of the distribution of Δx differs from a Gaussian, decreases toward zero as $v\Delta t$ increases. (The data fluctuates somewhat
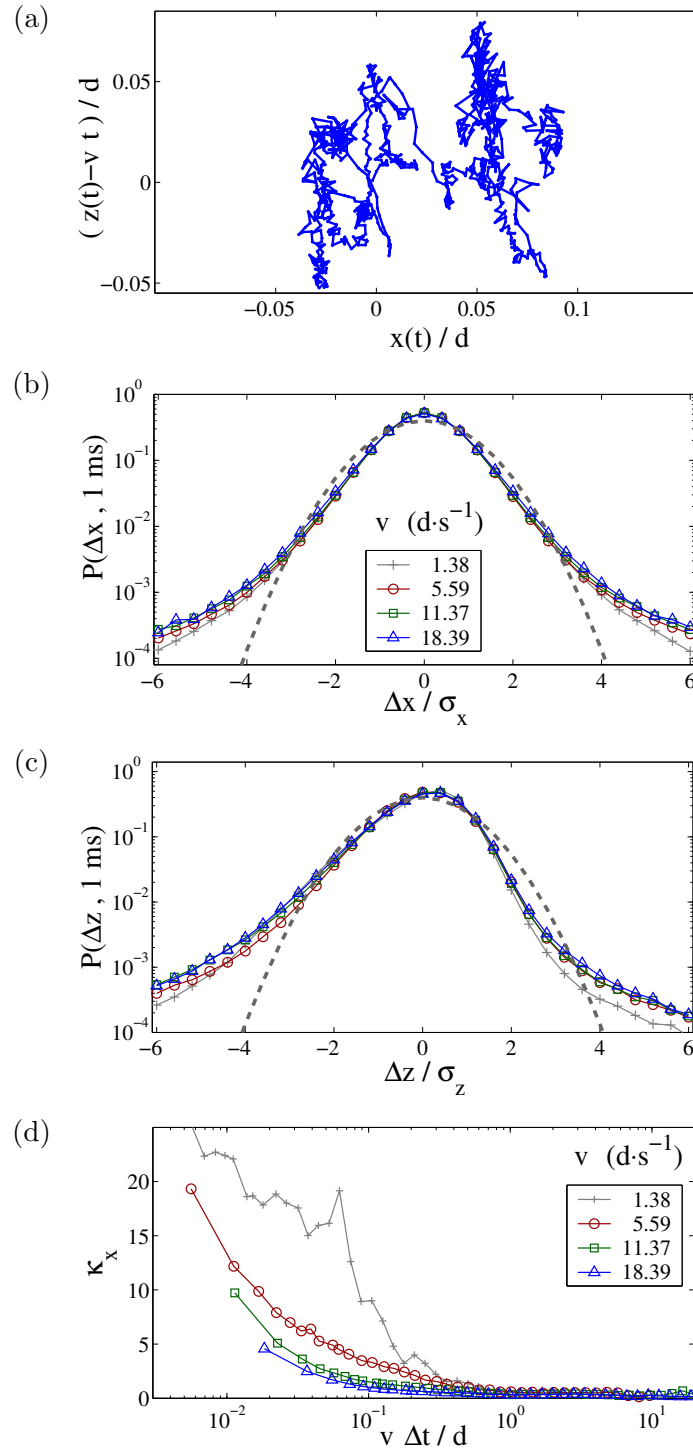
Figure 10-2: (a) A typical particle trajectory sampled at 1 ms intervals in a frame moving with the average flow speed, v. (b)~(c) Normalized PDFs for the 1 ms particle displacements, Δx and Δz, for various flow speeds, v, compared to a standard Gaussian distribution (dotted line); standard deviations, σ_x and σ_z, are of order $10^{-3}d$. (d) The kurtosis of Δx versus the mean distance fallen, $v\Delta t$.
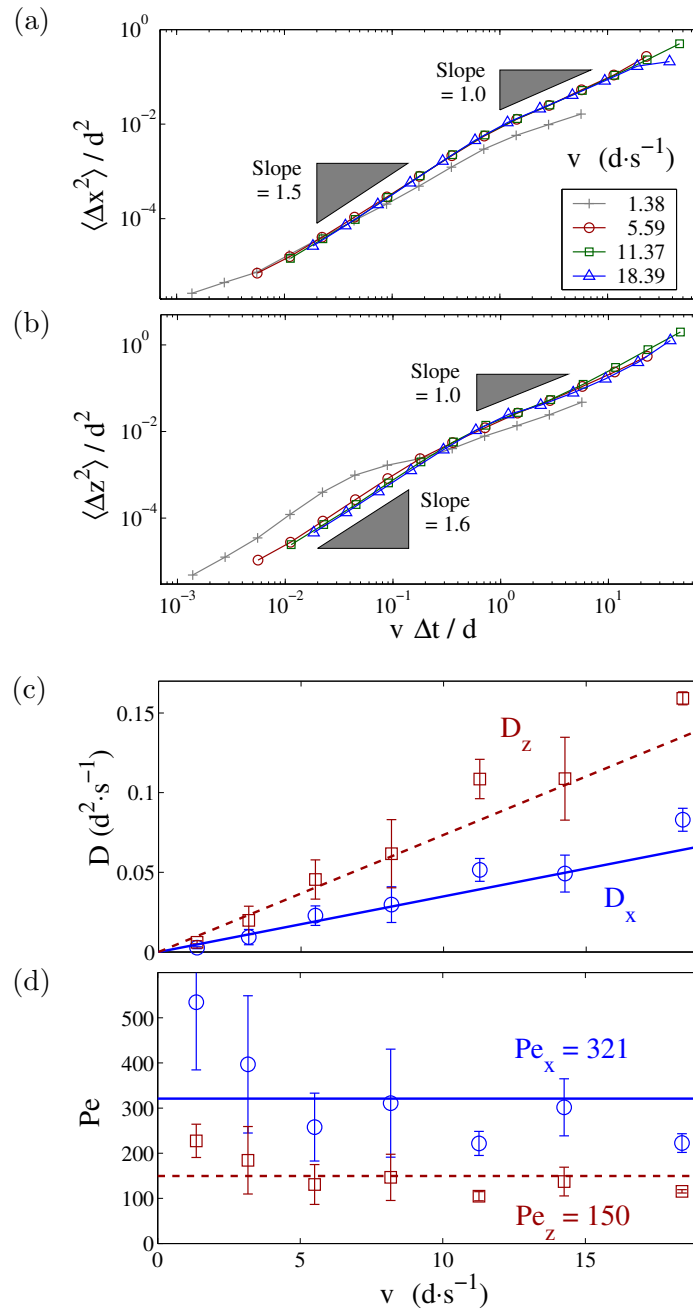
Figure 10-3: (a)~(b) Mean squared horizontal ($\langle \Delta x^2 \rangle$) and vertical ($\langle \Delta z^2 \rangle$) displacements versus mean distance dropped, which collapse onto a single curve for different flow speeds, v, except for the smallest where the flow is intermittent. (c)~(d) Diffusion coefficients (D) and Péclet numbers (Pe) in the horizontal (x) and vertical (z) directions versus v.

for $v = 1.38d/\text{sec}$, presumably due to intermittency.) This suggests a transition from super to normal diffusion.

As shown in Fig. 10-3(a)~(b), the scaling of the mean-square displacements does, in fact, change from super-diffusive,

$$\langle \Delta x^2 \rangle \propto \Delta t^{1.5} \qquad \text{and} \qquad \langle \Delta z^2 \rangle \propto \Delta t^{1.6}, \tag{10.3}$$

to diffusive

$$\langle \Delta x^2 \rangle \propto \langle \Delta z^2 \rangle \propto \Delta t. \tag{10.4}$$

The normal diffusion in long time scales is consistent with previous studies of dense drainage where particles were tracked with lower time resolution [134, 135]. Curiously, the super-diffusion is slower than ballistic transport in fluids, $\langle \Delta x^2 \rangle \propto \langle \Delta z^2 \rangle \propto \Delta t^2$, which has been found in a recent indirect measurement of granular flow [136], albeit at the scale of surface roughness ($< 25\,\text{nm} \approx d/10,000$).

Sub-ballistic scaling and non-Gaussian statistics at short times suggest that dense granular flows differ from classical fluids, as becomes more clear upon changing the flow rate. In a fluid, this causes a linear increase in Pe because the mean flow has no affect on molecular diffusion due to thermal fluctuations. Here, as shown in Fig. 10-3(c)~(d), the measured diffusion coefficients,

$$D_x = \lim_{\Delta t \to \infty} \frac{\langle \Delta x^2 \rangle}{2\Delta t}, \tag{10.5}$$

are actually proportional to the flow speed (with $D_z \approx 2.1 D_x$, consistent with the discussion above). So the Péclet numbers,

$$\text{Pe}_x = \frac{v\,d}{D_x} \approx 321 \qquad \text{and} \qquad \text{Pe}_z = \frac{v\,d}{D_z} \approx 150, \tag{10.6}$$

interpreted as the distances (in unit of d) for a particle to fall before it diffuses by a diameter in x or z direction, respectively, are roughly constant. This suggests that diffusion and advection are caused by the same physical mechanism, such as a passing void. The measured Péclet numbers, however, are two orders of magnitude larger than predicted by the void model.

Since $D_x, D_z \propto v$, we plot the mean square displacements versus the mean distance dropped in the laboratory frame, $v\Delta t$. Remarkably, as shown in Fig. 10-3(a)~(b), this
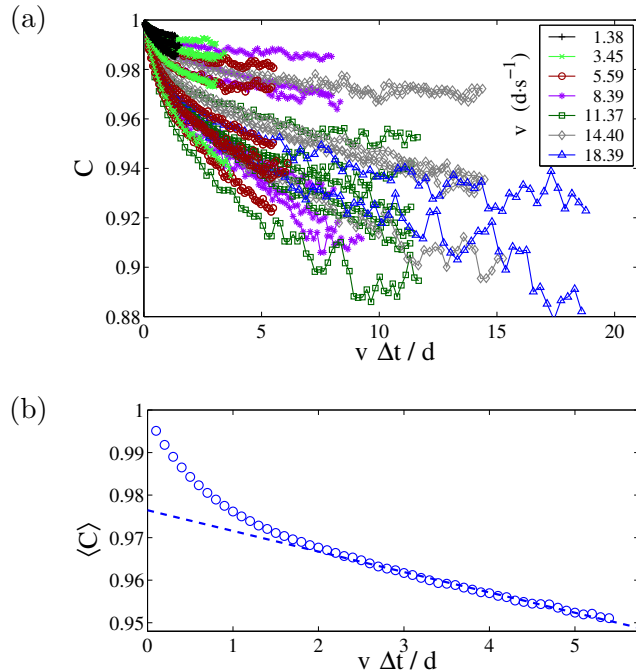
Figure 10-4: (a) The topological cage correlation function, $C(\Delta t)$, versus the mean distance fallen, $v\Delta t$, and (b) the average over all experiments in the continuous-flow regime ($W \geq 16$ mm), compared with an exponential fit in the diffusive regime (dotted line).

collapses all of our data for different flow speeds onto a single curve, not only in the diffusive regime, but also in the super-diffusive regime. (The data for the smallest flow speed again differs somewhat.) A smooth crossover from super to normal diffusion occurs after particles have fallen roughly one particle diameter.

10.2 Rearrangement of Nearest Neighbors

Although advection dominates particle dynamics (Pe $\gg 1$), diffusion causes a gradual rearrangement of the "cage" of nearest neighbors. To investigate this mixing directly, we measure the topological correlation function, $C(\Delta t)$, defined as the fraction of nearest neighbor pairs preserved from times t to $t + \Delta t$, averaged over all t. We chose the cutoff for a nearest neighbor, $1.5d$, as the first minimum of the radial distribution function. (which yields coordinations near 0.59). As shown in Fig. 10-4(a), the data for $C(\Delta t)$ collapses when plotted versus $v\Delta t$, in the sense that no systematic dependence on v is observed (except perhaps for the smallest orifice widths), so in Fig. 10-4(b) we plot the average over all experiments in the continuous flow regime ($W \geq 16$ mm or $v \geq 5.59$ d/sec).

135

The cage correlation function in Fig. 10-4(b) exhibits a clear crossover, which closely parallels the ones for mean displacements in Fig. 10-3(a)∼(b). In the superdiffusive regime, $C(\Delta t)$ decreases fairly quickly (with a decay length of roughly $20d$), but after falling more than one particle diameter the rate of decrease (neighbor loss) slows considerably. Since the topology remains more than 90% intact within the observation window, the precise form of the long-distance decay is uncertain, but a least-squares exponential fit,

$$\langle C \rangle \sim 0.976 \exp(-v\Delta t/200d), \tag{10.7}$$

yields a "cage breaking length" of $200d$.

10.3 Validity of the Microscopic Theories

As explained in Sec. 9.1, particle diffusion is a key property to distinguish between different possible microscopic mechanisms for dense granular flow. From our measurement in Secs. 10.1 and 10.2, we found the mechanisms of the void model is not correct. In particular, the cage breaking length of order $100d$ firmly rejects the model because any void-particle exchange removes roughly half of the neighbors of a particle as it falls by only one diameter.

Our results also suggest that structural rearrangements with long-lasting contacts dominate diffusion in dense granular flows, as opposed to ballistic collisions, which are central to the kinetic theory of gases. To counter the argument that a collisional regime may exist below the experimental resolution ($\Delta t \ll 1$ ms), we show that this is inconsistent with the fact that diffusion and mixing depend only on geometry (Figs. 10-3∼10-4). In the standard model of a collisional gas, a particle dropping a distance, L, experiences an average of N collisions which must dissipate its gravitational potential energy: $m\,g\,L = (1/2)\,N\,(1-e^2)\,m\,v_r^2$, where m is the mass, g the gravitational acceleration, e the restitution coefficient, and v_r the mean relative velocity. To be consistent with our data, N should depend on L, but not the flow speed, v. Although v_r is unknown, we can make two estimates — both of which lead to a contradiction. The first starts from the natural formula, $v_r^2 \approx (\langle \Delta x^2 \rangle + \langle \Delta z^2 \rangle)/\Delta t^2$ with fixed $\Delta t = 1$ ms, which suggests $v_r \propto v^{0.8}$ by looking at the initial slope of $\langle \Delta z^2 \rangle$ in Fig. 10-3(b). The second follows from direct measurements [136] of v_r yielding $v_r \propto v^{2/3}$. In either case, N would not be constant. (Note that $(1-e^2)$ would typically correlate with v_r^2, so velocity-dependent restitution cannot compensate for the changes in v_r.)

More generally, in slow granular flows it seems that the concept of "granular temperature" based on thermodynamic, randomizing collisions is may not be useful. Figs. 10-3∼10-4 clearly show that fluctuations depend only on the distance fallen, and yet any notion of temperature should increase with the flow speed. The fact that the nearest-neighbor topology persists for distances comparable to the system size also seems to cast doubt on the assumption of ergodicity. Instead, our experimental data suggests that cage rearrangements are caused by the relaxation of contact networks, as are believed to occur in Couette cells [154]. Such networks could absorb potential energy via rolling and sliding neighbors. The breaking of a contact could cause non-Gaussian fluctuations and small-scale superdiffusion among the particles in a network, while the gradual destruction of a network (and reformation of a new one) as a particle falls farther than its own diameter could cause the observed transition to normal diffusion. All of these effects are dominated by the geometry of random close packings, which is not fully understood, even without any dynamics [155].

The fact that the dynamics only depends on geometry strongly suggests that advection and diffusion have the same physical source. Although it overpredicts particle diffusion, the assumption of passing void, at least, captures this feature. The spot model, similarly based on the diffusion of the free volume, correctly predict the geometry dominated diffusion, The relation of Péclet number and the particle diffusion length,

$$\text{Pe}_x = \frac{d}{b_{p,x}} \qquad \text{and} \qquad \text{Pe}_z = \frac{d}{b_{p,z}}. \tag{10.8}$$

with the measured values from Eq. (10.6) indicates that $w_x = b_{p,x}/b \approx 1/600$ and $b_{p,z}/b \approx 1/300$ since $b/d \approx 2$. These are consistent with the prediction of Spot Model, $w \approx 10^{-3} \sim 10^{-2}$.

Chapter 11

Conclusion to Part II

To summarize, we have experimentally investigated particle dynamics in dense granular flows as they occur in the drainage in silos and hoppers. High speed imaging and direct particle tracking techniques enables to test the microscopic bases of the existing theories. The particles inside the silo are imaged and tracked with unprecedented resolution in both space and time to obtain their velocity and diffusion properties. The data obtained by varying the orifice width and the hopper angle allows us to thoroughly test models of gravity driven flows inside these geometries.

All of our measured velocity profiles are smooth and free of the shock-like discontinuities ("rupture zones") predicted by critical state soil mechanics. On the other hand, we find that the simple Kinematic Model is in qualitative agreement with experiments. This model is appealing due to their mathematical simplicity and completeness, which allows direct application to various geometries. While it accurately captures the mean velocity profile near the orifice, it fails to describe the rapid transition to plug flow far away from the orifice. The measured diffusion length b, the only free parameter in the model, is not constant as usually assumed, but increases with both the height above the orifice and the angle of the hopper. It turns out that b nonlinearly depends on the velocity gradient. Clearly further work is needed to improve the Kinematic Model in the constitutive law and boundary conditions for both discrete and continuous models of slow, dense granular flows. We also discussed the flow rate as a function of the orifice width and hopper angles. We find that the flow rate scales with the orifice size to the power of 1.5, consistent with dimensional analysis and the similar investigations in three-dimensional cylindrical silo. Interestingly,

the flow rate increases when the funnel angle is increased.

From our data, we also directly measure the diffusion of the particles and the rearrangement of nearest neighbors. The particle displacements show a universal transition from super-diffusion to normal diffusion, as a function of the distance fallen, independent of the flow speed. In the super-diffusive (but sub-ballistic) regime, which occurs before a particle falls through its diameter, the displacements have fat-tailed and anisotropic distributions. In the diffusive regime, we observe slow diffusion and cage breaking significantly less than predicted by the void model, which provides the classical microscopic derivation of the Kinematic Model in terms of diffusing voids in the packing. The constant Péclet number supports that that diffusion and mixing are dominated by geometry, consistent with long-lasting contacts but not thermal collisions, and the kinetic theories with the notion of "granular temperature" may not be useful in dense granular flow.

The experimental data is consistent with the recently proposed Spot Model based on a simple mechanism for cooperative diffusion.

Bibliography

[1] M. Z. Bazant, J. Choi, and B. Davidovitch. Dynamics of conformal maps for a class of non-laplacian growth phenomena. *Phys. Rev. Lett.*, 91:045503, 2003.

[2] M. Z. Bazant, J. Choi, B. Davidovitch, and D. Crowdy. Transport-limited aggregation. *Chaos*, 14:S6, 2004.

[3] M. Z. Bazant, J. Choi, and B. Davidovitch. Advection-diffusion-limited aggregation. *Chaos*, 14:S7, 2004.

[4] J. Choi, D. Margetis, T. M. Squires, and M. Z. Bazant. Steady advection-diffusion around finite absorbers in two-dimensional potential flows. *to appear in J. Fluid Mech.*, 2005.

[5] J. Choi, A. Kudrolli, and M. Z. Bazant. Velocity profile of granular flows inside silos and hoppers. *J. Phys.: Condens. Matter*, 17:1, 2005.

[6] J. Choi, A. Kudrolli, R. R. Rosales, and M. Z. Bazant. Diffusion and mixing in gravity-driven dense granular flows. *Phys. Rev. Lett.*, 92:174301, 2004.

[7] T. C. Halsey. Diffusion-limited aggregation: A model for pattern formation. *Physics Today*, page 36, Nov 2000.

[8] T. A. Witten and L. M. Sander. Diffusion-limited aggregation, a kinetic critical phenomenon. *Phys. Rev. Lett.*, 47:1400, 1981.

[9] H. E. Stanley. Fractals and multifractals: the interplay of physics and geometry. In A. Bunde and S. Havlin, editors, *Fractal and disordered systems*, page 1. Springer, Berlin, 2nd edition, 1996.

[10] P. G. Saffman ang G. I. Taylor. The penetration of a fluid into a porous medium or hele-shaw cell containing a more viscous liquid. *Prc. R. Soc. London, Ser. A*, 245: 312, 1958.

[11] L. Niemeyer, L. Pietronero, and H. J. Wiesmann. Fractal dimension of dielectric breakdown. *Phys. Rev. Lett.*, 52:1033, 1984.

[12] R. M. Brady and R. C. Ball. Fractal growth of copper electrodeposits. *Nature*, 309: 225, 1984.

[13] D. A. Kessler, J. Koplik, and H. Levine. Pattern selection in fingered growth phenomena. *Adv. Phys.*, 37:255, 1988.

[14] B. Shraiman and D. Bensimon. Singularities in nonlocal interface dynamics. *Phys. Rev. A*, 30:2840, 1984.

[15] E. Sharon, M. G. Moore, W. D. McCormick, and H. L. Swinney. Coarsening of fractal viscous fingering patterns. *Phys. Rev. Lett.*, 91:205504, 2003.

[16] A. Arnéodo, Y. Couder, G. Grasseau, V. Hakim, and M. Rabaud. Uncovering the analytical saffman-taylor finger in unstable viscous fingering and diffusion-limited aggregation. *Phys. Rev. Lett.*, 63:984, 1989.

[17] L. Paterson. Diffusion-limited aggregation and two-fluid displacements in porous media. *Phys. Rev. Lett.*, 52:1621, 1984.

[18] R. C. Ball and E. Somfai. Theory of diffusion controlled growth. *Phys. Rev. Lett.*, 89: 135503, 2002.

[19] R. C. Ball and E. Somfai. Diffusion-controlled growth: Theory and closure approximations. *Phys. Rev. E*, 67:021401, 2003.

[20] F. Barra, B. Davidovitch, A. Levermann, and I. Procaccia. Laplacian growth and diffusion-limited aggregation: different universality classes. *Phys. Rev. Lett.*, 87: 134501, 2001.

[21] F. Barra, B. Davidovitch, and I. Procaccia. Iterated conformal dynamics and laplacian growth. *Phys. Rev. E*, 65:046144, 2002.

[22] E. Somfai, R. C. Ball, J. P. DeVita, and L. M. Sander. Diffusion-limited aggregation in channel geometry. *Phys. Rev. E*, 68:020401, 2003.

[23] P. Ya. Polubarinova-Kochina. On a problem of the motion of the contour of a petroleum shell. *Dokl. Akad. Nauk S. S. S. R.*, 47:254, 1945. In Russian.

[24] L. A. Galin. Unsteady filtration with a free surface. *Dokl. Akad. Nauk S. S. S. R.*, 47:246, 1945. In Russian.

[25] M. B. Hastings and L. Levitov. Laplacian growth as one-dimensional turbulence. *Physica D*, 116:244, 1998.

[26] E. Somfai, L. M. Sander, and R. C. Ball. Scaling and crossovers in diffusion limited aggregation. *Phys. Rev. Lett.*, 83:5523, 1999.

[27] M. Z. Bazant and D. Crowdy. Conformal mapping methods for interfacial dynamics. In S. Yip, editor, *The Handbook of Materials Modeling*, volume I, page 4.10. Springer, 2005.

[28] B. Davidovitch, A. Levermann, and I. Procaccia. Convergent calculation of the asymptotic dimension of diffusion-limited aggregates: scaling and renormalization of small clusters. *Phys. Rev. E*, 62:5919, 2000.

[29] P. Meakin, R. C. Ball, P. Ramanlal, and L. M. Sander. Structure of large two-dimensional square-lattice diffusion-limited aggregates: Approach to asymptotic behavior. *Phys. Rev. A*, 35:5233, 1987.

[30] M. G. Stepanov and L. S. Levitov. Laplacian growth with separately controlled noise and anisotropy. *Phys. Rev. E*, 63:061102, 2001.

[31] B. B. Mandelbrot, A. Vespignani, and H. Kaufman. *Europhys. Lett.*, 32:199, 1995.

[32] B. Davidovitch, M. J. Feigenbaum, H. G. E. Hentschel, and I. Procaccia. Conformal dynamics of fractal growth patterns without randomness. *Phys. Rev. E*, 62:1706, 2000.

[33] M. B. Hastings. Fractal to nonfractal phase transition in the dielectric breakdown model. *Phys. Rev. Lett.*, 87:175502, 2001.

[34] M. Plischke and Z. Rácz. Active zone of growing clusters: Diffusion-limited aggregation and the eden model. *Phys. Rev. Lett.*, 53:415, 1984.

[35] C. Amitrano, A. Coniglio, P. Meakin, and M. Zannetti. Multiscaling in diffusion-limited aggregation. *Phys. Rev. B*, 44:4974, 1991.

[36] B. B. Mandelbrot, B. Kol, and A. Aharony. Angular gaps in radial diffusion-limited aggregation: Two fractal dimensions and nontransient deviations from linear self-similarity. *Phys. Rev. Lett.*, 88:055501, 2002.

[37] E. Somfai, R. C. Ball, N. E. Bowler, and L. M. Sander. Correction to scaling analysis of diffusion-limited aggregation. *Physica A*, 325:19, 2003.

[38] R. C. Ball, N. E. Bowler, L. M. Sander, and E. Somfai. Off-lattice noise reduction and the ultimate scaling of diffusion-limited aggregation in two dimensions. *Phys. Rev. E*, 66:026109, 2002.

[39] H. G. E. Hentschel and I. Procaccia. The infinite number of generalized dimensions of fractals and strange attractors. *Physica D*, 8:435, 1983.

[40] T. C. Halsey, M. H. Jensen, L. P. Kadanoff, I. Procaccia, and S. Shraiman. Scaling structure of the surface layer of diffusion-limited aggregates. *Phys. Rev. Lett.*, 33:1141, 1986.

[41] N. G. Makarov. On the distortion of boundary sets under conformal mappings. *Proc. London Math. Soc.*, 59:2067, 1985.

[42] T. C. Halsey. Some consequences of an equation of motion for diffusive growth. *Phys. Rev. Lett.*, 59:2067, 1987.

[43] B. Davidovitch, H. G. Hentschel, Z. Olami, I. Procaccia, L. M. Sander, and E. Somfai. Dla and iterated conformal maps. *Phys. Rev. E*, 59:1368, 1999.

[44] L. A. Turkevich and H. Scher. Occupancy-probability scaling in diffusion-limited aggregation. *Phys. Rev. Lett.*, 55:1026, 1985.

[45] M. H. Jensen, A. Levermann, J. Mathiesen, and I. Procaccia. Multifractal structure of the harmonic measure of diffusion-limited aggregates. *Phys. Rev. E*, 65:046109, 2002.

[46] B. Davidovitch, M. H. Jensen, A. Levermann, J. Mathiesen, and I. Procaccia. Thermonynamic formalism of the harmonic measure of diffusion limited aggregates: phase transition. *Phys. Rev. Lett.*, 87:164101, 2001.

[47] T. A. Witten and L. M. Sander. Diffusion-limited aggregation. *Phys. Rev. B*, 27:5686, 1983.

[48] R. Ball, M. Nauenberg, and T. A. Witten. Diffusion-controlled aggregation in the continuum approximation. *Phys. Rev. A*, 29:2017, 1984.

[49] E. Erzan, L. Pietronero, and A. Vespignani. The fixed-scale transformation approach to fractal growth. *Rev. Mod. Phys.*, 67:545, 1995.

[50] M. B. Hastings. Renormalization theory of stochastic growth. *Phys. Rev. E*, 55:135, 1997.

[51] T. C. Halsey and M. Leibig. Theory of branched growth. *Phys. Rev. A*, 46:7793, 1992.

[52] T. C. Halsey. Diffusion-limited aggregation as branched growth. *Phys. Rev. Lett.*, 72: 1228, 1994.

[53] T. C. Halsey, B. Duplantier, and K. Honda3. Multifractal dimensions and their fluctuations in diffusion-limited aggregation. *Phys. Rev. Lett.*, 78:1719, 1997.

[54] D. Bensimon, L. Kadanoff, B. I. Shraiman, and C. Tang. Viscous flows in two dimensions. *Rev. Mod. Phys.*, 58:977, 1986.

[55] M. J. Feigenbaum, I. Procaccia, and B. Davidovitch. Pattern selection: Determined by symmetry and modifiable by long-range effects. *J. Stat. Phys.*, 103:973, 2001.

[56] P. Bouissou, B. Perrin, and P. Tabeling. Influence of an external flow on dendritic crystal growth. *Phys. rev. A*, 40:509, 1989.

[57] Y.-W. Lee, R. Ananth, and W. N. Gill. Selection of a length scale in unconstrained denditic growth with convection in the melt. *J. Crystal Growth*, 132:226, 1993.

[58] F. Argoul and A. Kuhn. The influence of transport and reaction processes on the morphology of a metal electrodeposit in thin gap geometry. *Physica A*, 213:209, 1995.

[59] J. M. Huth, H. L. Swinney, W. D. McCormick, A. Kuhn, and F. Argoul. Role of convection in thin-layer electrodeposition. *Phys. Rev. E*, 51:3444, 1995.

[60] L. M. Cummings, Y. E. Hohlov, S. D. Howison, and K. Kornev. Two-dimensional solidification and melting in potential flows. *J. Fluid Mech.*, 378:1, 1999.

[61] F. Barra, H. G. E. Hentschel, A. Levermann, and I. Procaccia. Quasistatic fractures in brittle media and iterated conformal maps. *Phys. Rev. E*, 65:045101, 2002.

[62] M. Z. Bazant. Conformal mapping of some non-harmonic functions in transport theory. *Proc. Roy. Soc. A.*, 460:1433, 2004.

[63] T. Needham. *Visual Complex Analysis*. Oxford University Presss, Oxford, UK, 1997.

[64] K. G. Kornev and G. L. Mukhamadullina. Mathematical theory of freezing for flow in porous media. *Proc. Roy. Soc. A*, 447:281, 1994.

[65] G. F. Carrier, M. Krook, and C. E. Pearson. *Functions of a complex variable*, chapter 2 and 5 and 8. Hod Books, Ithaca, NY, 1983.

[66] V. M. Entov and P. I. Etingof. Viscous flows with time-dependent free boundaries in a non-planar hele-shaw cell. *Euro. J. of Appl. Math.*, 8:23, 1997.

[67] F. Parisio, F. Moraes, J. A. Miranda, and M. Widom. Saffman-taylor problem on a sphere. *Phys. Rev. E*, 63:036307, 2001.

[68] G. Leal. *Laminar flow and convective transport processes*. Butterworth-Heineman, New York, 1992.

[69] A. Acrivos and T. D. Taylor. Heat mass transfer from single spheres in stokes flow. *Phys. Fluids*, 5:387, 1962.

[70] H. Brenner. Forced convection heat and mass transfer at small péclet numbers from a particle of arbitrary shape. *Chem. Eng. Sci.*, 18:109, 1963.

[71] C. G. Phillips. Heat and mass transfer from a film into steady shear flow. *Quart. J. Mech. Appl. Math.*, 43:135, 1990.

[72] V. Magar, T. Goto, and T. J. Pedley. Nutrient uptake by a self-propelled steady squirmer. *Quart. J. Mech. Appl. Math.*, 56:65, 2003.

[73] M. J. Boussinesq. Sur le pouvoir refroidissant d'un courant liquide ou gazeux. *J. de Math.*, 1:285, 1905.

[74] J. Koplik, S. Redner, and E. J. Hinch. Tracer dispersion in planar multipole flows. *Phys. Rev. E*, 50:4650, 1994.

[75] M. Morega and A. Bejan. Heatline visualization of forced convection in porous media. *Int. J. Heat Fluid Flow*, 36:42, 1994.

[76] I. Eames and J. W. M. Bush. Long dispersion by bodies fixed in a potential flow. *Proc. Roy. Soc. A*, 455:3665, 1999.

[77] J. C. R. Hunt and I. Eames. The disappearance of laminar and turbulent wakes in complex flows. *J. Fluid Mech.*, 457:111, 2002.

[78] L. van Wijngaarden. Asymptotic solution of a diffusion problem with mixed boundary conditions. *Proc. Koninkl. Nederl. Akad. Wet.*, 69:263, 1966.

[79] V. A. Maksimov. On the determination of the shape of bodies formed by solidification of the fluid phase of the stream. *Appl. Math. Mech. (Prikl. Mat. Mekh.)*, 40:264, 1976.

[80] V. A. Chugunov and K. G. Kornev. Dynamics of ice-rock barriers under conditions of freezing of filtering rocks. *J. Eng. Phys. (Inzh.-Fiz. Zh.)*, 51:981, 1986.

[81] K. G. Kornev and V. A. Chugunov. Determination of the equilibrium shape of the bodies formed during the solidification of filteration flow. *J. Appl. Math. Mech. (Prikl. Mat. Mekh.)*, 52:773, 1988.

[82] M. M. Alimov, K. G. Kornev, and G. L. Mukhamadullina. The equilibrium shape of an ice-soil body formed by liquid flow past a pair of freezing columns. *J. Appl. Math. Mech. (Prikl. Mat. Mekh.)*, 58:873, 1994.

[83] M. M. Alimov, K. G. Kornev, and G. L. Mukhamadullina. Hysteretic effects in the problems of artificial freezing. *SIAM J. Appl. Math.*, 59:387, 1998.

[84] L. J. Cummings and K. G. Kornev. Evolution of flat crystallisation front in forced hydrodynamic flow-some explicit solutions. *Physica D*, 127:33, 1999.

[85] S. D. Howison. Complex variable methods in hele-shaw moving boundary problems. *Euro. J. Appl. Math.*, 3:209, 1992.

[86] G. K. Batchelor. *An introduction to fluid dynamics.* Cambridge University Press, Cambridge, UK, 1967.

[87] I. Stakgold. *Green's functions and boundary value problems.* Wiley, New York, 2nd edition edition, 1998.

[88] C. E. Pearson. On the finite strip problem. *Quart. Appl. Math.*, XV:203, 1957.

[89] E. C. Titchmarsh. *Introduction to the theory of Fourier integrals.* Clarendon Press, Oxford, UK, 3rd edition edition, 1948.

[90] N. I. Muskhelishvili. *Singular Integral Equations.* Dover, New York, 1992. Based on the second Russian edition of 1946.

[91] V. L. Rvachev. The pressure on an elastic half-space of a stamp in the form of a strip in a plane. *Prikl. Mat. Mekh.*, 20:163, 1956. (In Russian).

[92] V. S. Protsenko and V. L. Rvachev. Plate in the form of an infinite strip on an elastic half-space. *J. Appl. Math. Mech. (Prikl. Mat. Mekh.)*, 40:273, 1976.

[93] M. G. Krein. Integral equations on a half line with kernel depending upon the difference of the arguments. *Am. Math. Transl.*, 22:163, 1962.

[94] D. Margetis and J. Choi. Convergent iteration scheme by the wiener-hopf method for advection-diffusion problems. *in preparation*, 2005.

[95] L. N. Trefethen. *Spectral methods in matlab.* SIAM, Philadelphia, PA, 2000.

[96] B. Noble. *Methods based on the Wiener-Hopf technique for the solution of partial differential equations.* Chelsea, New York, 1988. 2nd edition.

[97] V. M. Aleksandrov and A. V. Belokon. Asymptotic solutions of a class of integral equations encountered in the investigation of mixed problems of the mathematical physics for regions with cylindrical boundaries. *J. Appl. Math. Mech. (Prikl. Mat. Mekh.)*, 32:402, 1968.

[98] V. M. Aleksandrov and D. A. Pozharskii. An asymptotic method in contact problems. *J. Appl. Math. Mech. (Prikl. Mat. Mekh.)*, 63:283, 1999.

[99] T. Carleman. über die abelsche integralgleichung mit konstanten integrationsgrenzen. *Math. Zeitschrift*, 15:111, 1922.

[100] V. M. Aleksandrov and A. V. Belokon. Asymptotic solutions of a class of integral equations and its application to contact problems for cylindrical elastic bodies. *J. Appl. Math. Mech. (Prikl. Mat. Mekh.)*, 31:718, 1967.

[101] I. S. Gradshteyn and I. M. Ryzhik. *Tables of integrals, series, and products*. Academic Press, New York, 1980.

[102] E. J. Hinch. *Perturbation Methods*. Cambridge University Press, Cambridge, UK, 1991.

[103] N. Goldenfeld. *Lectures on Phase Transitions and the Renormalization Group*. Perseus Books, Reading, MA, 1992.

[104] L. Y. Chen, N. D. Goldenfeld, and Y. Oono. The renormalization group and singular perturbations: multiple scales, boundary layers and reductive perturbation theory. *Phys. Rev. E*, 54:376, 1996.

[105] J. M. Myers. Wave scattering and the geometry of a strip. *J. Math. Phys.*, 6:1839, 1965.

[106] J. M. Myers. Derivation of a matrix painlevé equation germane to wave scattering by a broken corner. *Physica D*, 11:51, 1984.

[107] G. E. Latta. The solution of a class of integral equations. *Rat. Mech. Anal.*, 5:821, 1956.

[108] K. G. Kornev. private communication. 2004.

[109] W-S. Dai, L. P. Kadanoff, and S.-M. Zhou. Interface dynamics and the motion of complex singularities. *Phys. Rev. A*, 43:6672, 1991.

[110] I. Eames, M. A. Gilbertson, and M. Landeryou. The effect of an ambient flow on the spreading of a viscous gravity current. *J. Fluid Mech.*, 523:261, 2005.

[111] J. Duran. *Sands, powders and grains.* Springer, New York, 2000.

[112] H. M. Jaeger, S. R. Naegel, and R. P. Behringer. Granular solids, liquids, and gases. *Rev. Mod. Phys.*, 68:1259, 1996.

[113] J. M. Ottino and D. V. Khakhar. Mixing and segregation of granular materials. *Annu. Rev. Fluid Mech.*, 32:55, 2000.

[114] D. Talbot. The next nuclear plant. *MIT Technology Review*, 105:54, 2002.

[115] A. C. Kadak and M. Z. Bazant. Pebble flow experiments for pebble-bed reactors. In *Proceedings of the Second International Topical Meeting on High Temperature Reactor Technology*, Beijing, China, 2004.

[116] W. A. Beverloo, H. A. Leniger, and J. V. de Velde. The flow of granular solids through orifices. *Chem. Eng. Sci.*, 15:260, 1961.

[117] G. W. Baxter, R. P. Behringer, T. Fagert, and G. A. Johnson. Pattern formation in flowing sand. *Phys. Rev. Lett.*, 62:2825, 1989.

[118] J. R. Prakash and K. K. Rao. Steady compressible flow of cohesionless granular materials through a wedge-shaped bunker. *J. Fluid Mech.*, 225:21, 1991.

[119] R. M. Nedderman. *Statics and Kinematics of Granular Materials.* Cambridge University Press, Cambridge, 1992.

[120] D. G. Schaeffer. Instability in the evolution equations describing incompressible granular flow. *J. Diff. Eq.*, 66:19, 1987.

[121] E. B. Pitman and D. G. Schaeffer. *Commun. Pure Appl. Math.*, 40:421, 1987.

[122] J. Litwiniszyn. Statistical methods in the mechanics of granular bodies. *Rheol. Acta*, 213:146, 1958.

[123] J. Litwiniszyn. *Bull. Acad. Pol. Sci.*, 9:61, 1963.

[124] J. Litwiniszyn. The model of a random walk of particles adapted to researches on problems of mechanics of loose media. *Bull. Acad. Pol. Sci.*, 11:593, 1963.

[125] J. Mullins. Stochastic theory of particle flow under gravity. *J. Appl. Phys.*, 43:665, 1972.

[126] J. Mullins. Critique and comparison of two stochastic theories of gravity-induced particle flow. *Powder Tech.*, 23:115, 1979.

[127] H. Caram and D. C. Hong. Random-walk approach to granular flows. *Phys. Rev. Lett.*, 67:828, 1991.

[128] R. M. Nedderman and U. Tüzün. A kinematic model for the flow of granular materials. *Powder Tech.*, 22:243, 1979.

[129] U. Tüzün and R. M. Nedderman. Experimental evidence supporting kinematic modelling of the flow of granular media in the absence of air drag. *Powder Tech.*, 24:257, 1979.

[130] J. Mullins. Experimental evidence for the stochastic theory of particle flow under gravity. *Powder Tech.*, 9:29, 1974.

[131] U. Tüzün, G. T. Houlsby, R. M. Nedderman, and S. B. Savage. The flow of granular magerials ii: velocity distributions in slow flow. *Chem. Engng. Sci.*, 37:1691, 1982.

[132] A. Samadani, A. Pradhan, and A. Kudrolli. Size segregation of granular matter in silo discharges. *Phys. Rev. E*, 60:7203, 1999.

[133] A. Medina, J. A. Córdova, E. Luna, and C. Trevi no. Velocity field measurements in granular gravity flow in a near 2d silo. *Phys. Lett. A*, 250:111, 1998.

[134] S. S. Hsiau and M. L. Hunt. Shear-induced particle diffusion and longitudinal velocity fluctuations in a granular-flow mixing layer. *J. Fluid Mech.*, 251:299, 1993.

[135] V. V. R. Natarajan, M. L. Hunt, and E. D. Taylor. Local measurements of velocity fluctuations and diffusion coefficients for a granular material flow. *J. Fluid Mech.*, 304:1, 1995.

[136] N. Menon and D. J. Durian. Diffusing-wave spectroscopy of dynamics in a three-dimensional granular flow. *Science*, 275:1920, 1997.

[137] S. B. Savage. *J. Fluid Mech.*, 92:53, 1979.

[138] J. T. Jenkins and S. B. Savage. A theory for the rapid flow of identical, smooth, nearly elastic, spherical particles. *J. Fluid Mech.*, 130:187, 1983.

[139] S. S. Hsiau and M. L. Hunt. Kinetic theory analysis of flow-induced particle diffusion and thermal conduction an granular material flows. *J. Heat Transfer*, 115:541, 1993.

[140] M. Z. Bazant, J. Choi, C. H. Rycroft, R. R. Rosales, and A. Kudrolli. A theory of cooperative diffusion in dense granular flows. *Preprint: cond-mat/0307379*, 2004.

[141] M. Z. Bazant. The spot model for granular drainage. *to appear in Mechanics of Materials*, 2005.

[142] C. H. Rycroft, M. Z. Bazant, J. Landry, and G. S. Grest. Dynamics of random packings in granular flow. *in preparation*, 2004.

[143] Z. Zhong, J. Y. Ooi, and J. M. Rotter. The sensitivity of silo flow and wall stress to filling method. *Engineering Structure*, 23:756, 2001.

[144] J. C. Crocker and D. G. Grier. Methods of digital video microscopy for colloidal studies. *J. Colloid Interface Sci.*, 179:298, 1996.

[145] GDR MiDi. On dense granular flows. *Eur. Phys. J. E*, 14:341, 2004.

[146] R. C. Brown and J. C. Richards. *Principles of Powder Mechanics*. Pergamon, New York, 1970.

[147] U. Tüzün and R. M. Nedderman. An investigation of the flow boundary during stady-state discharge from a funnel-flow bunker. *Powder Tech.*, 31:27, 1982.

[148] J. Crank. *Mathematics of Diffusion*. Clarendon Press, Oxford, 1975.

[149] S. F. Edwards. In A. Mehta, editor, *Granular Matter: An Interdisciplinary Approach*, page 121. Springer, New York, 1994.

[150] A. Barrat, J. Kurchan, V. Loreto, and M. Sellitto. Edwards' measures for powders and glasses. *Phys. Rev. Lett.*, 85:5034, 2000.

[151] H. A. Makse and J. Kurchan. Nature. *Testing the thermodynamic approach to granular matter with a numerical model of a decisive experiment*, 415:614, 2002.

[152] A. J. Liu and S. R. Nagel. Jamming is not just cool any more. *Nature*, 396:21, 1998.

[153] E. R. Weeks and D. A. Weitz. Properties of cage rearrangements observed near the colloidal glass transition. *Phys. Rev. Lett.*, 89:095704, 2002.

[154] D. Howell, R. P. Behringer, and C. Veje. Stress fluctuations in a 2d granular couette experiment: A continuous transition. *Phys. Rev. Lett.*, 82:5241, 1999.

[155] S. Torquato, T. M. Truskett, and P. G. Debenedetti. Is random close packing of spheres well defined? *Phys. Rev. Lett.*, 84:2064, 2000.